Western University

Scholarship@Western

Electronic Thesis and Dissertation Repository

10-26-2020 2:00 PM

Characterization for Spray Droplet Behaviour in Afterburner-like Flow Conditions

Matthew D. Mahaffy, *The University of Western Ontario*

Follow this and additional works at: https://ir.lib.uwo.ca/etd

Part of the Aerodynamics and Fluid Mechanics Commons, and the Heat Transfer, Combustion Commons

Recommended Citation

Abstract

Fuel injection processes can contribute to combustion instability in highly energetic combustion systems. In gas turbine engine afterburners, jet-in-crossflow (JIX) injection is used. Part one of the thesis study investigates the interaction between spray droplets and turbulent flow properties of a JIX. Jet-in-counterflow (JIC) configuration was also investigated. Part two of the investigation examined the behaviour of JIX droplets around a bluff body. Droplet size and flow turbulence was characterized simultaneously using particle image velocimetry and image processing techniques. Turbulence and droplet size were correlated, particularly at momentum flux ratios ≥ 60. High speed imaging was used to identify droplet breakup mechanisms and size distribution around the bluff body. Overall, the current techniques allow for a reasonable simultaneous investigation of the coupled behaviour between JIX droplets and turbulence, and further development of the technique may have a significant impact on improved understanding of the mechanisms of JIX.

Keywords

Summary for Lay Audience

In highly energetic combustion systems, such as the afterburner of a fighter jet engine, many fluid dynamic processes interact in complex ways. Proper fuel injection control is particularly important in regulating the heat in the engine and fuel flow rates may need to be adjusted depending on many flight conditions such as altitude or aircraft speed. The fuel injectors in an afterburner are very simple device which are similar to an oscillating sprinkler, except the injectors do not oscillate and the wind blows on the liquid jets at 900km/h and 1000°C, producing a spray of droplets. This spray injection process determines how well the afterburner is functioning. The chaotic nature of the gas and fuel mixture created by these injections is not well understood on a detailed level. Most measures of injection spray identify only the overall shape of the spray and the sizes of the droplets. To better understand this fuel injection process, this thesis investigates the movement of fluid between the spray droplets and attempts to correlate the flow behaviour with the droplet sizes in order to gain a better understanding of how the spray is mixed and distributed in an afterburner. This injection process is termed jet-in-crossflow (JIX), and it is found in many other applications such as irrigation, agricultural sprays, and numerous different combustion systems not limited to aircraft afterburners. Ultimately, a more detailed understanding of how JIX creates and distributes droplets may lead to improved control over fuel injection, therefore reducing fuel consumption. In addition, as the fight against climate change continues systems that rely on fossil fuel for combustion will need to switch to alternative fuels which need to be certified for use. Different fuels have different behaviours so understanding the fuel injection process is crucial in predicting and testing how a new fuel will behave in an existing combustion system.

Acknowledgments

I would like to thank my lab mates and colleagues for the interesting discussions and for helping me troubleshoot issues. It was a pleasure getting to know everyone of the course of my 2 years in the lab.

I would like to acknowledge the support provided by my family and friends provided in my pursuit of a 2nd graduate degree. Their endless encouragement kept me going when things got difficult.

I am sincerely grateful to my other half Dorothy. We both made it through grad school together, and I wouldn't have it any other way. Your patience and understanding kept me going when I was at my worst.

Finally, I would like to greatly extend my thanks to my supervisor Kamran Siddiqui for his unwavering support, and endless patience, and to Joanna without whom I may not have finished this thesis. I have no words to express my gratitude for the encouragement, support, and guidance they provided.

Table of Contents

List of Tables

List of Figures

Preface

The present thesis study was completed at an unprecedented time. With the COVID-19 pandemic forcing a large majority of the world into social distancing, experimental research was disrupted, creating many challenges. In addition, upon approval of an early return to research in order to complete this thesis on time, equipment malfunctions occurred requiring that a new methodology be developed to complete the bluff body study in Chapter 4, with as little as 3 months remaining in the program. Please keep these constraints in consideration when scrutinizing the accomplished scope of work, as well as the quality of methodology and results in Chapter 4.

Chapter 1

1 Introduction

Gas turbine engines, first designed for aviation purposes by Frank Whittle back in the 1930s, were the foundation of modern aviation. In principle, the gas turbine operates on the open Brayton (thermodynamic) cycle, which uses gas as the working fluid. The cycle consists of compressing the gas, adding heat at constant pressure, and then allowing the heated gas to expand through a turbine (more often multiple turbines) to extract useful work. Heat is then removed from the system and the gas is recirculated to the compressor. In the open Brayton cycle, the heat addition phase often occurs through combustion and therefore the inlet gas (reactants) needs to be expelled (products). These exhaust gases may consist entirely of combustion products, or they may be a mixture of reactants and products, such as in turbofan engines. Although the open Brayton cycle is most commonly used, closed Brayton cycles do find use in power generation, primarily in Europe [1].

1.1 The Afterburner

The basic components of a GTE, as well as a modification called an afterburner are illustrated in Figure 1. The book *Aerothermodynamics of Aircraft Engine Components* contains a chapter on afterburners written by E. Zukoski [2] which provides great insight into the history of research and development of the afterburner and was the primary resource for this section.
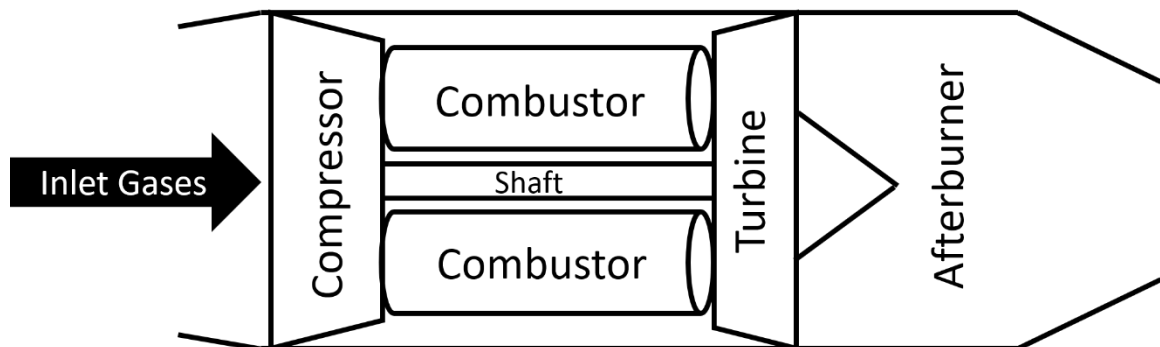
Figure 1: Illustration of the components of a turbojet engine fitted with afterburner

Gas turbine engines are often fitted with modifications such as afterburner (turbojets), fans (turbofans), or propellers (turboprops) depending on the required efficiency or functionality of the engine. While turbofan and turboprop engines modify the gas intake system to provide large mass flow rates at lower flow velocity, afterburners increase thrust of a GTE by greatly accelerating the exhaust gases relative to the same non-afterburning engine. Gas turbine afterburners are used primarily in military aviation to increase the thrust-to-weight ratio of an aircraft. The additional thrust provided by an afterburner is beneficial in situations requiring supersonic flight or short take-off, however this performance comes at the cost of poor thermodynamic and fuel efficiency.

An afterburner modifies the thermodynamic Brayton cycle by providing a re-heat stage as the gas exits the turbine (hence why afterburners are also described as reheat engines). An afterburner may operate under a wide range of conditions due to its primary use in military aviation, with chamber temperatures of 600°C to >1000°C, pressures of 0.5atm to 6atm, and gas velocities of 150m/s to 250m/s [3]. With inlet temperatures greater than 1000°C [3], the increased gas temperature (relative to the ~500°C primary combustor inlet temperatures) provides an ideal thermodynamic state for a secondary round of combustion to occur within the afterburner. Since the afterburner is the last stage of the engine and its components can be better designed to withstand high temperatures (relative to turbine blades), an afterburner can achieve a higher maximum temperature, increasing the thermodynamic work available to produce thrust. However, this secondary combustion is less efficient than the primary combustion due to the reduced pressure at the turbine exit. Increased thrust can also be achieved by increasing the mass flow rate during secondary combustion via increased fuel consumption. The inefficiency of the afterburner is evident in the operating specifications of any military combat jets. For example, the EJ200 engine used on the Eurojet fighter triples its fuel consumption when operating under reheat (afterburning flight) but only achieves 1.5 times increased thrust [4].

Afterburners were created as a design solution to increase thrust-to-weight performance of a GTE. The afterburner achieves increased thrust through the relatively inefficient but effective solution described above, and it achieves this increase in thrust at relatively low weight penalty by minimizing part count and complexity.

Afterburners are constructed with few primary components (see Figure 2a) and these components are notably less complex than elsewhere in an engine. At the afterburner inlet, fuel injector manifolds are supported through struts connecting them to the diffuser cone. As shown in Figure 2b and 2c, the injectors found in the afterburner are often no more complex than radially oriented spray bars or annular injection manifolds which contain many small sub-millimeter injection orifices. This type of injection is called jet-in-crossflow (JIX) injection or spray as a liquid jet is injected into a crossflowing gas. Following the injectors are flameholders which are used to anchor the flames. The flameholders are necessary as afterburner flames are highly susceptible to blowout due to the high velocity of the gas. Lining the walls of the afterburner are typically some form of perforated sheets which aid in acoustic dampening as well as outer wall cooling. Finally, the combustion products accelerate through a nozzle in order to produce thrust.

1.1.1 Combustion Instability

Combustion instability occurs in dynamic combustion systems when unsteady processes participate in closed-loop feedback resulting in the amplification and/or sustenance of those unsteady processes. It is not uncommon to find such instabilities in systems which contain large amounts of energy (such as afterburners), because a very small fraction of the available energy can result in disturbances large enough to be harmful to nominal operation of the combustion system.
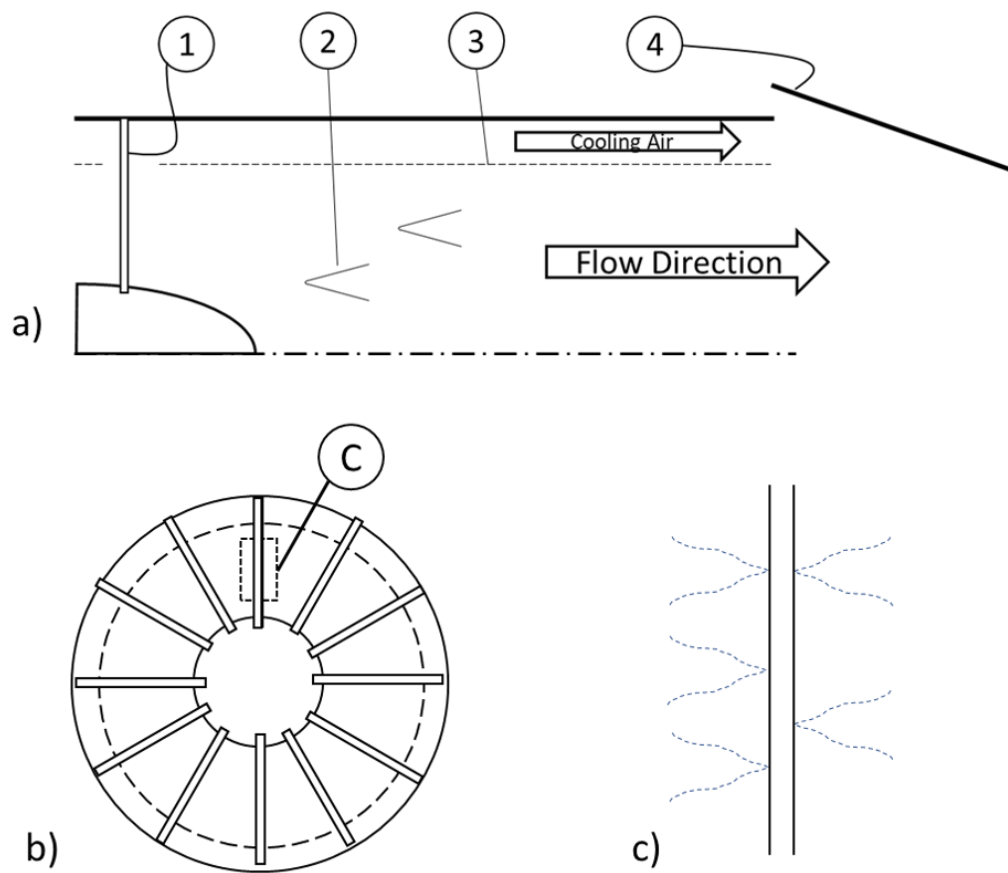
Figure 2: a) Symmetric, cross-section sketch of a typical afterburner duct. Hot air exiting the turbine first encounters the injection manifold (1), which here consists of radial spray bars. The air and injected fuel then reaches the annular flameholders (2) where combustion occurs. The acoustic liner (3) attenuates acoustic modes within the duct, and combustion products exit via a nozzle (4). Figure b) shows an axial view of the afterburner showing the radial spray bar configuration (flameholders omitted for clarity), and figure c) is a close up of a spray bar showing the directon of spray is tangential.

Thermo-acoustic instability is a form of combustion instability and refers to the interaction between sound (pressure) waves and heat. It has been described as early as 1878 by Lord Rayleigh [5], where he discussed the production of sound due to a coupling between heat release and fluid density. Rayleigh's criterion (Equation (1) [6]) was developed to show that when the perturbations in heat release are appropriately in phase with fluctuations in pressure, the initial perturbations gain more energy than is dissipated, leading to growing and self-sustaining instability. In Equation (1), p' is the zero-mean fluctuating pressure, q' is the zero-mean fluctuating heat release and the integration is occurring over the fluid domain Ω. In fact, Equation (1) is a contributes to the overall energy balance of a system by describing the growth or dissipation of energy created through the coupling of heat and pressure. If p' and q' are both positive (increasing mean quantities) or negative (decreasing mean quantities) at the same instant, they contribute to an increase in energy.

$$\iiint_{\Omega} p'(t)q'(t)d\Omega > 0 \tag{1}$$

Rayleigh's criterion was further developed by Chu [7], and Nicoud and Poinsot [8], who proposed an inequality which accounts for acoustic loses and entropy fluctuations in the system since isentropic assumptions inherent in Rayleigh's criterion are invalid for reacting flows [7], [8].

In a GTE, both the primary combustors and the afterburner are susceptible to combustion instabilities, however the manifestation of this instability will vary due to the differing geometry and mechanisms of combustion for the two combustor types. Both are susceptible to transverse (radial) instability, as are many combustion systems, which can also be linked to azimuthal instabilities [9]. Longitudinal (axial) instabilities, on the other hand, are of greater concern in afterburners due to reduced acoustic impedances upstream and downstream of the combustion zone.

In afterburners, thermoacoustic instabilities lead to two well-known behaviours: *rumble* and *screech*. Screech is often described as a high frequency transverse pressure wave typically damped by adding a screech/acoustic liner near the wall of the afterburner duct. Rumble on the other hand, is a low frequency thermoacoustic instability consisting of

longitudinal pressure waves which propagate axially in the afterburner duct. Both types of thermoacoustic instability are known to be detrimental to the structural integrity of the afterburner duct, with the potential to cause catastrophic damage within seconds if not addressed. For example, rumble, also termed reheat buzz, has been shown to cause vibrations coincident with the torsional frequency of the engine's low-pressure shaft, putting unwanted stress on the shaft [10].

Afterburner rumble affects numerous processes in the afterburner duct, such as atomization of fuel and behaviour of flameholders, because of its ability to propagate in the streamwise direction. Because of these longitudinal waves, the heat release fluctuations from the afterburning flame can become in phase with the pressure waves in the afterburner such that the thermoacoustic instability gains more energy than it dissipates as described by Rayleigh's criteria. Hence, rumble can become self-sustaining under certain conditions.

A number of factors can contribute to the closed-loop feedback system resulting from longitudinal pressure wave. These factors and their interactions have been summarized by Candel [11]. The factors which may participate in the feedback system can be broadly categorized into gas dynamics and fuel dynamics [3], [11], [12].

1.1.2   Afterburner Gas Dynamics

The gas dynamics within a combustion chamber are one aspect of the system which needs to be understood to fully understand combustion instability, and the gas dynamics are highly dependent on the design of the chamber. There are some commonalities between chamber designs, such as cooling flow through the combustion chamber walls and the use of acoustic liners and flameholders in afterburners, but the majority of combustor designs will differ enough to affect the gas flow through the combustor. Some examples of the effect of combustor design on the manifestation of instability can be seen in primary GTE combustors, where swirl injectors and cannular chamber designs can create unique azimuthal flow behaviours [9]. However, these are not used in afterburners.

In afterburners, the design of the bluff body flameholder contributes most to the behaviour of combustion. The flow around a bluff body is composed of three primary regions: the

boundary layers, the recirculation zone (RZ), and the wake region, as illustrated in Figure 3a. The end of the RZ is defined by a stagnation point and the flow adjacent to the stagnation point has been termed the close-out region (COR). The COR identifies a location that is particularly susceptible to flame blow off in reacting bluff body flow [13], [14] in part due to the high gradients present near the stagnation point.
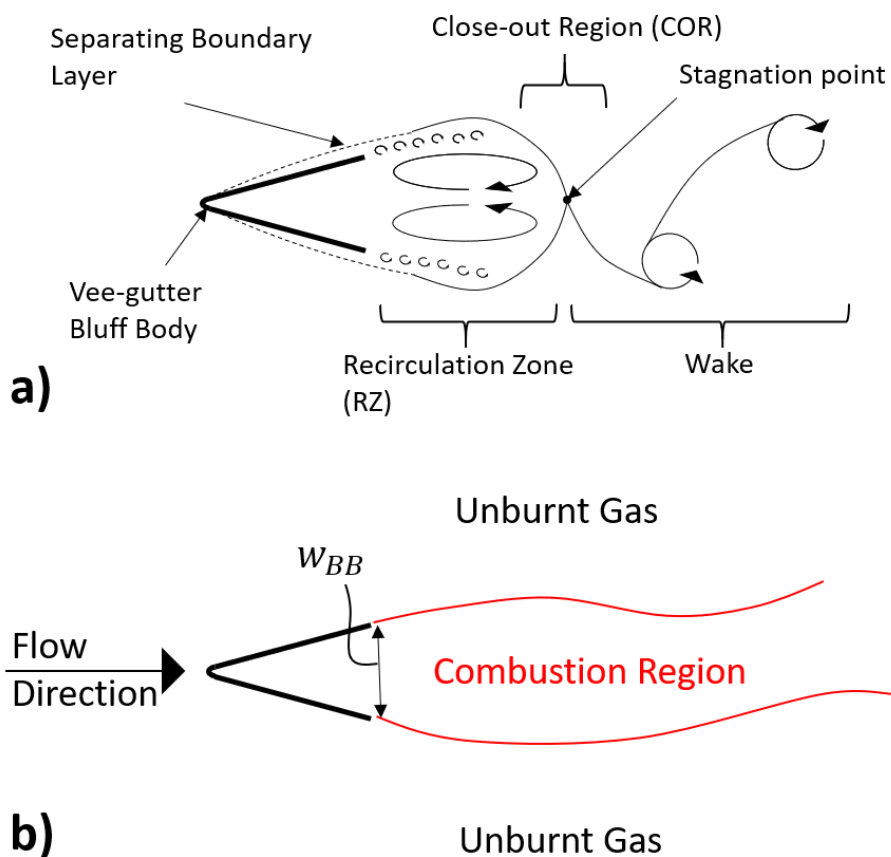
Figure 3: a) Features of bluff body flow. The boundary layer separates from the bluff body to from a free shear layer and a recirculation zone. Downstream the periodic shedding of vortices occurs. b) The combustion region is surrounded by unburnt gas which contributes to flow instability via temperature gradients.

Bluff bodies are used in reacting flow in order to anchor the flames and therefore are called flame holders. The stability of the flame is determined by the conditions under which the flame does not experience blowoff (i.e. the flame separates from the bluff body) and this is dependent on operating conditions like gas velocity and fuel-to-air ratio (FAR) [15]. In

order for a flame to be stabilized on a bluff body, the time required to mix the combustion reactants must be less than the residence time of the reactants to ensure a homogenously distributed mixture of fuel and oxidizer is used for combustion [16]. Although mixing begins at the time of injection, the flameholder is ultimately responsible for achieving stability by increasing mixing and residence time of the reactants.

While bluff bodies perform well as flameholders, they also generate flow instabilities such as Kelvin-Helmholtz (KH) shear layer instabilities formed by the separating boundary layer and Benard – von Karman (BVK) vortices which leave periodic vortical structures in the wake of the bluff body and therefore in the combustion zone [17]. The behaviour of these flow instabilities can be directly related to fluctuations in heat release [18], and can become amplified by external excitations [19] such as from thermo-acoustic instability. The KH and BVK instabilities that interact with thermo-acoustic instability can be affected by the large differences in temperature that exist between the combustion gas (temperature of burned products, T_b) and the surrounding non-reacting flow (temperature of unburned gas, T_u) (see Figure 3b). In particular, for a temperature ratio $T_b/T_u \approx 2$ the BVK instability is dominant in the wake and present in the flame behaviour, while $T_b/T_u \approx 4$ results in KH instabilities dominating the behaviour of the flame [20], [21].

A combination of temperature gradient between the freestream and bluff body wake and of fuel distribution to the bluff body results in widely ranging behaviour of thermo acoustic instability. In order to completely understand the problem, it is equally important to understand the fuel behaviour upstream of the bluff body in order to understand the onset of combustion instability. For example, it is known that close-coupled fuel injection (fuel injection released from the bluff body) contributes to greater magnitudes of heat release fluctuations as compared to upstream fuel injection [18] due to the resulting fuel distribution at the bluff body.

1.1.2.1   Fuel Behaviour

Distribution of fuel to either to RZ or to the COR in the bluff body wake can produce stable combustion. However, delivery of fuel primarily to the COR has been shown to increase the risk of flame blowoff [14], and that this is typically achieved by increasing the penetration of liquid jet injection (which results from larger liquid flow rates and therefore an increased FAR). Blowoff mechanisms were found to be both a result of fuel lean conditions (lower than stoichiometric FAR) in the RZ and unsteady combustion in the COR.

Typically, the effect of fuel distribution on combustion dynamics is classified using a bulk liquid injection rate to estimate the FAR in the system, or chemiluminessence is used to examine the flame composition during combustion [17], [18], [22]. The bulk liquid injection rate is determined by the mass flow of fuel injected, $\dot{m}_{fuel}$, to the mass flow of air coming into the combustion chamber, $\dot{m}_{air}$. On the other hand, chemiluminessence is a more advanced, optical-based measurement technique which can be used to obtain an estimate of the spatial FAR distribution in the combustion region. These measures capture the FAR at a fairly large spatial discretization and have so far succeeded in a better understanding of thermo-acoustic instability in combustors. It has been shown that varying the FAR ratio of the system can affect the amplitudes of acoustic pressure oscillation [23], [24], and that these amplitudes peaked as the FAR approached the stoichiometric ratio (which is the ideal FAR for complete combustion). However, detailed local fluid dynamics are not often quantified in the context of jet-in-crossflow injection used for combustion. This present a knowledge gap in the area of detailed droplet advection between the injector orifices and the bluff body (or combustion site) Some work has been found which characterizes fuel droplet sizes and spatial distribution in the combustion region [25], however this work did not involve bluff body flow, nor did it discuss the dynamic droplet behaviour or its interaction with the gas crossflow.

Since the fuel is not only present in the combustion region, but the behaviour of fuel also needs to be considered starting from the injection site. In this regard, thermo-acoustic behaviour on liquid injection has two effects. First, the fluctuating pressure field results in fluctuating fuel injection rate; second, the velocity field gradients affect the advection and

distribution of liquid fuel to the combustion region. Numerical methods have shown that it is the velocity field gradients that primarily influence the advection of liquid by reducing the droplet size [26], [27], but this has yet to be discussed in the afterburner combustion context.

1.2   Jet-in-Crossflow Spray Mechanics

To understand the importance of droplet size in the combustion process, the behaviour of the jet-in-crossflow fuel injection process needs to be understood (JIX). In the last decade, Ebrahimi [28] and Lovett et al. [3] both outlined areas of research required to advance afterburner technology, and one of these areas was improved knowledge of fuel spray behaviour under afterburner conditions. These conditions include high temperature (600°C to 1000°C) and high velocity gas flow (150m/s to 250m/s). In addition to these extreme conditions, spray injection is a complex two-phase flow and is a challenge to quantify in detail using numerical studies or experimental work. Currently, research on liquid fuel injection is largely based on experimental data. As the aviation industry pushes towards biofuels and creates new technologies, experimental testing is needed to certify and approve advancements in technologies. Therefore, it is important to have a detailed understanding of the behaviour of liquid fuel injection in a gas turbine engine combustors and afterburners.

1.2.1   Primary and Secondary Jet Breakup

To understand fuel jet behaviour in combustors and afterburners, it is necessary to first comprehend the mechanisms of liquid jet and droplet breakup. Jet-in-crossflow (JIX) is particularly relevant to the simple orifice injectors used in afterburners. Broumand and Birouk [29] published an extensive review on the behaviour of liquid jet-in-crossflow. The review was limited to subsonic, non-reacting flow, but it presents the relevant factors affecting liquid jet breakup and droplet breakup regimes as well as the conditions under which most experiments have been performed.

The primary variables in describing jet breakup are the momentum flux ratio, q (Equation (2)), and the Weber number which are defined as,

$$q = \frac{\rho_j v_j^2}{\rho_g v_g^2} \tag{2}$$

$$We = \frac{\rho_g v_g^2 d}{\sigma} \tag{3}$$

where the ρ is the fluid density, v is the characteristic fluid velocity (freestream gas velocity or the injection velocity for JIX), d is the characteristic length scale (the jet injection orifice diameter for JIX), and σ is the surface tension coefficient between the two fluids. The subscripts j and g represent values for the liquid jet, and the crossflow gas, respectively. The Weber number is representative of the ratio of inertial forces on the liquid jet to the surface tension of the liquid. The form presented in Equation (3) is more accurately described as the gas Weber number, We_g, and is most often used in regime mapping of JIX breakup processes. The Reynolds number (Equation (4)) is also a parameter of interest as it represents the ratio of inertial forces to viscous forces and is useful in characterising the turbulence of a fluid. The Reynolds number is defined as,

$$Re = \frac{\rho v l}{\mu} \tag{4}$$

where l is a characteristic length (such as the jet diameter d_o or the bluff body width w_{BB}), v is the bulk fluid velocity, ρ is the fluid density, and μ is the fluid dynamic viscosity.

Primary breakup of a liquid JIX is typically characterized by four regimes (see Figure 4) which can be related to the We_g. Wu et al. [30] were the first to characterize these regimes and the general ranges of We_g in which they occur. The enhanced capillary regime, which occurs for low $We_g < 11$, is dominated by capillary forces. In other words, the driving force causing the column (which is the continuous, unbroken fluid jet exiting the injection orifice) to break is the surface tension within the liquid. For We_g from 11 to 30, bag breakup occurs during which, the strain induced on the liquid column creates a thin fluid film (which forms the shape of a bag) which proceeds to burst into droplets. For $We_g > 90$, shear

breakup occurs; a process by which the crossflow causes stripping of droplets directly from the column surface. In between bag and shear breakup is multimode breakup, which is a combination of shear and bag breakup. The range of We_g under which these regimes fall has been found to vary slightly (e.g., [31], [32]), and they are only valid for a non-turbulent liquid jet.

Each of these regimes can be summarized as occurring through column breakup and surface stripping (also called shear breakup) to varying extents, where column breakup is dominant when the momentum of the crossflow is low relative to the momentum or surface tension of the jet, and *vice versa* for shear breakup. Shear breakup occurring on the JIX column, which results in the formation of ligaments and droplets, is the primary contributor to jet breakup. Secondary breakup occurs where these ligaments and droplets break into smaller droplets. Primary breakup typically occurs in the near-field region, that is, near the liquid column (see Figure 5) while secondary breakup occurs downstream, in the far-field.
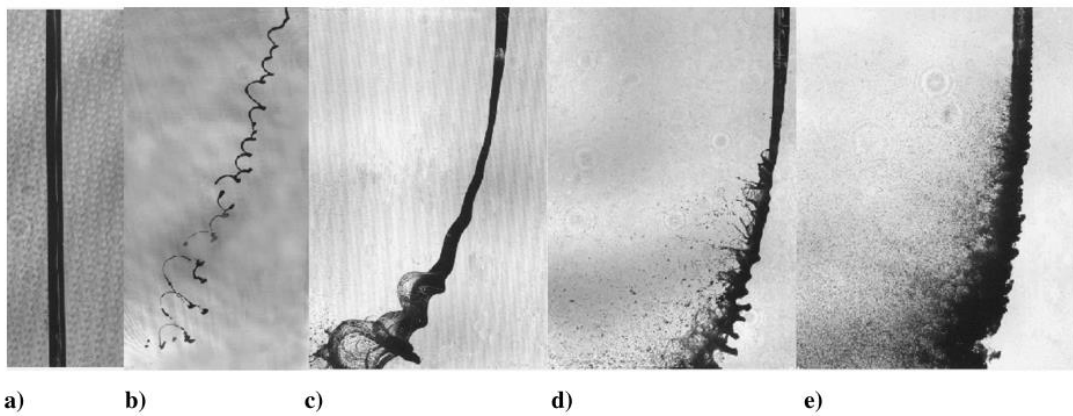
Figure 4: Primary jet-in-crossflow breakup regimes: a) undisturbed jet, b) enhanced capillary breakup, c) column bag breakup, d) multimode breakup, and e) shear (Reprinted from Ref. [33] **with permission from AIAA)**
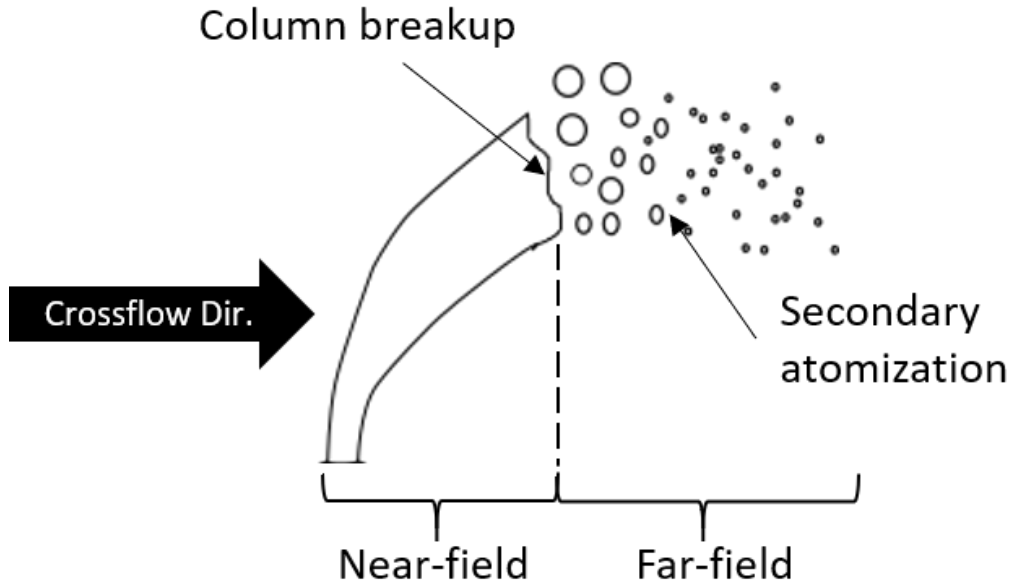
Figure 5: Schematic drawing of pertinent jet-in-crossflow regions including the rough definition of near-field and far-field sprays

Proposed surface breakup mechanisms of the JIX include boundary layer stripping and hydrodynamic instability on the jet surface. In past studies, these mechanisms are often observed breakup behaviour occurring on individual droplets but are extrapolated and applied to our understanding of secondary breakup behaviour occurring on liquid columns [30]. Boundary layer stripping is a process by which the gas flow introduces a velocity boundary layer at the surface of the liquid jet as a result of viscous interaction between the fluids [34]. Alternatively, hydrodynamic instability assumes inviscid deformation of the jet which results in the creation of waves at the jet-gas interface. If the amplitude of these waves is sufficiently large droplets begin to shed from the liquid column [35]. Ultimately, both mechanisms describe the mass shedding of droplets from the surface of the liquid jet and studies have linked this shedding to the gas momentum properties ρ_g and v_g [34], [36] which is why the momentum flux ratio q is of importance. Neither group discussed the momentum transport behaviour created by interaction between the gas and liquid phases.

Primary JIX breakup has been found to have an effect on secondary breakup due to the primary breakup contributions to jet geometry (penetration and column breakup length)

[33]. The characteristics of droplets resulting from primary breakup, such as velocity upon breakup, seem to be unaffected by crossflow velocity [37] but can be dependent on the jet Reynolds number Re_j which uses the liquid properties and jet diameter d_o as parameters. The jet Reynolds number has been used to quantify whether the momentum of the crossflowing fluid causes column breakup (aerodynamic breakup) or if the inertia or turbulence of the jet itself causes breakup to occur (non-aerodynamic). Aerodynamic breakup occurs up to around Re_j of 6,000 while turbulent breakup begins to occur around Re_j of 60,000 [38], [39]. A typical afterburner Re_j is estimated to be 30,000 and greater meaning that primary breakup exists in a transition region between aerodynamic and turbulent jet breakup.

Primary breakup and secondary breakup depend on interactions between the streamwise crossflow and the liquid jet [33], [34], [40], [41], and numerous works have shown that distribution of droplet sizes within the spray changes with crossflow velocity and momentum flux ratio. There was agreement among the literature that, at low q, the maximum droplet sizes are found in the core of the spray, and at high q, the maximum droplet sizes are found in the periphery of the spray [30], [32], [42]. Overall droplet diameter was also found to be reduced with increasing crossflow velocity [32] or with increasing We_g [43]. In addition, We_g dependence was found for secondary droplet breakup, where secondary breakup processes were independent of droplet size given that We_g remains constant [40]. Ultimately, the end of the secondary breakup process is a result of reduced relative velocity between the droplet and the crossflow (which is often described as the droplet relaxation) [41]. Again, while air and liquid flow velocities and spatial appearance have been examined, the impact of turbulence on breakup processes was not investigated.

Occasionally, inlet turbulence will be reported, but it is not typically investigated. For example, Lubarsky et al. [44] characterised the JIX spray behaviour with and without the presence of combustion and while they showed that inlet turbulence was affected by the combustion, and that the combustion process affected the upstream spray breakup process, no independent conclusion could be made on the impact of inlet turbulence on spray breakup. Only recently has work been reported on the detailed interaction between

crossflow turbulence and spray breakup. Broumand, Birouk, and Mahmoodi [45] found that increased inlet crossflow turbulence for low We_g flow (We_g less than 10) results in fluctuations of the liquid jet and delayed transition from primary to secondary breakup. Turbulence also changed the jet geometry, causing it to bend earlier than in studies with a more uniform inlet flow. This initial work provides reason to avoid generalizing liquid JIX behaviours for a variety of turbulent gas flow conditions; but it still does not address how turbulence interacts with the spray. This work also only covers a small range of low We_g and does not consider the impact of combustion or bluff bodies.

1.2.2   Jet-in-Crossflow Under Afterburner Conditions

Afterburners typically operate at extremely high crossflow gas temperatures and velocities. Broumand and Birouk [29] identified the scarcity of studies of liquid jets in high temperature and/or pressure (HTP) crossflow. Generally, for jet-in-crossflow studies, HTP is considered for temperatures around 500K to 600K and pressures up to 2atm, meaning that, at temperatures >900K and pressures up to 6bar, afterburner operating conditions well exceed the expected environment for JIX applications. Regardless, a few research studies have been reported in the literature that investigated the jets in crossflow under afterburner conditions [44], [46], [47].

These studies were performed at a large range of temperatures (from 23°C to 900°C), pressures (1atm to 5atm), and velocities (40m/s to 270m/s) in order to simulate a range of conditions covering the flight envelope (the range of expected operating conditions) of an afterburner as well as used jet-A fuel and the liquid. Droplet sizes were lower at higher crossflow pressure and velocity, and in general were approximately 30μm to 60μm in diameter. The largest droplets, up to 250μm, were found near the injection site at low density and velocity crossflow conditions, while the smallest droplets, as low as 12μm, were found downstream in high density and velocity crossflow. The droplet diameter did not change under different injector geometries (i.e., turbulent vs. non-turbulent liquid jet). The behaviour of droplets in the vicinity of a bluff body was also examined for a close-coupled injection configuration, which is a configuration in which the spray originates from the bluff body walls and showed that there was no notable difference in droplet size under reacting and non-reacting conditions. But although droplet sizes did not vary, close-

coupled injection has been linked to bluff body thermoacoustic instability due to lack of fuel pre-mixing [18]. These works are limited in that they are surprisingly focused on jets which originate from wall orifices, rather than from spray bars or manifolds like those used in industry application.

1.3   Knowledge Gaps

Liquid JIX spray studies have identified that the behaviour of the liquid spray and its resulting droplets are dependent upon the primary and secondary jet breakup processes. These processes are seen to vary depending on the We_g and q. The momentum flux ratio q affects the jet penetration and column breakup point of the jet while the We_g and crossflow velocity affect droplet size after secondary atomization. In afterburners, crossflow velocities of 50m/s to 200m/s have resulted in droplet formation with diameters as low as 30μm and up to 250μm. While there seems to be consensus that crossflow velocity plays a large role on droplet formation and size, the role of the crossflow turbulence has only recently been investigated [45]. Even still, the role of turbulence in determining droplet size was not concluded, nor was the effect of turbulence on droplet advection examined.

In addition to JIX breakup, the fuel and gas dynamics of the afterburner, which are intimately linked, were discussed with respect to the behaviour of the bluff body anchored flame in combustion instability. Investigation of bluff body dynamics has shown that KH and BVK flow instabilities can manifest itself in the flame dynamics resulting in heat release fluctuations. These flow instabilities can be influenced by fuel distribution to the bluff body wake, but currently, detailed droplet distribution in the combustion region is unknown as it is measured on a more global scale using the overall FAR of the system or using chemiluminessence techniques.

1.4   Thesis Objectives

The primary objective of this thesis research is to investigate the local gas and liquid behaviours and their interactions under afterburner-like flow configurations. The specific focus is on the characterization and fundamental understanding of how the liquid spray

influences the local mean and turbulent velocity fields and the relationships between droplet size and various flow characteristics.

In order to achieve this objective, improvements and additions were made to the existing experimental wind tunnel facility at the University of Western Ontario. Jet-in-crossflow was performed within the wind tunnel and spray and crossflow behaviour was captured using particle image velocimetry (PIV) and image processing techniques. The experimental setup was created with a modular design to allow for numerous geometric configurations. A bluff body was also inserted into the wind tunnel to examine how the spray interacted with the flow instabilities created by the bluff body. The relative position of the spray bar, injection orifice, and bluff body could be varied.

The first part of this study includes the characterization of the jet-in-crossflow (JIX). This serves two purposes: the characterization of the specific simple orifice spray bar injector, and the development of a methodology to non-intrusively and simultaneously investigate the individual behaviour of the liquid and gas phases as well as their interactions. A jet-in-counterflow (JIC) configuration was also examined using the same techniques at the request of the project sponsor.

The second part of this study serves to further the experimental research relating to jet-in-crossflow applications in GTE afterburners. Experimental facilities were modified in order to create afterburner-like conditions, particularly relating to the design. A bluff body was introduced downstream of the spray bar and the gas-droplet flow around the bluff body was investigated. Ideally, the investigation of turbulence and droplet distribution was to be similar to part one of this study. However, due to equipment malfunction and constraints imposed by the COVID-19 pandemic, the development of a different, yet novel method was undertaken. High-speed imaging was used to examine the droplet motion and the droplet size distribution around the bluff body.

1.5   Thesis Layout

This thesis is in monograph format and has been organized as such to describe all experimental methods and analytical techniques prior to reporting and analyzing the results of the experimental studies.

Chapter 1 provides the background information related to afterburners, current state of knowledge and challenges, and the knowledge gaps. The thesis objectives are defined next along with the organizational structure of the thesis.

Chapter 2 describes in detail the experimental setup, instrumentation and measurement techniques used in both parts of the research. The Chapter also explains the data analysis approaches used.

Chapter 3 provides detailed results related to the first part of the study focused on the detailed characterization of flow and droplet behaviours in the two configurations, jets in crossflow and jets in counterflow, as well as discussion of the results.

Chapter 4 presents the detailed results related to the second part of the study focused on the droplet characterization in the presence of the vee-shaped bluff body.

Chapter 5 summarizes the results from both parts of the study. The potential future works necessary to continue this study are also elaborated in this Chapter.

Chapter 2

2 Experimental Setup and Methods

In order to perform an investigation on the flow behaviour of a liquid jet-in-crossflow, an experimental setup was devised which can create desired liquid and gas flow conditions. This chapter will begin by describing modifications made to the existing wind tunnel in order to attempt to increase the gas crossflow velocity. The description of the design of an injection system used to create a liquid jet in crossflowing gas will follow, as well as the components necessary to accommodate the introduction and removal of a liquid droplets within the wind tunnel. The experimental setups and techniques relevant to data capture, processing, and analyzing are also being described, which include the PIV algorithm and the droplet detection algorithm. The equations for the outcome metrics for each study are also presented.

2.1 Wind Tunnel Setup

The wind tunnel is located in the Gas Dynamics laboratory in Western university's Mechanical Engineering Department. The test section of the wind tunnel is $0.457 \text{ m} \times 0.457$ m in cross-section and 1.22 m long. Air is circulated through this wind tunnel using a Howden Buffalo Model 38-26-1770 Series fan, powered by a 30HP variable speed motor (Baldor-Reliance Model No. 10F312Y670G1). The typical configuration can achieve speeds of 3 m/s to 55 m/s in the test section with a freestream turbulence of less than $\pm 1\%$. The entire wind tunnel operates horizontally, with the test section at roughly the same height as the fan. Flow conditioning is achieved through four consecutive graduated flow conditioning screens (porosity of 60%) immediately upstream of the contraction section. Air temperature is controlled via a commercial chiller (Super Radiator Coils Model 45x45-3R-58/72) which extracts heat through a heat exchanger located upstream of the conditioning screens, to maintain constant air temperatures within $\pm 1°$ in the test section. In the present study, the temperature was not regulated using the heat exchanger as it was not necessary, due to the open loop configuration discussed later. Regardless, the air temperature entering the contraction of the wind tunnel was monitored throughout all studies using a four Channel Type K Data Logger (Omega model HH374) and temperatures

were found to vary by less than ±1°. The wind tunnel ducts are made of glass fiber reinforced composite (GFRP) over a balsa wood core, and it rests on rubber-in-shear mounts fastened to a frame made of structural steel tubing for vibration dampening.

A primary goal for this research work was to achieve wind tunnel speeds of up to Mach 0.5 to adequately simulate gas momentum effects found in an afterburner environment. In addition, the introduction of liquid into the wind tunnel necessitated that modifications to the wind tunnel be made to avoid circulation of liquid droplets within the tunnel. The following sections discuss the construction of a secondary contraction, a new diffuser, and a reduced cross section test section designed to increase freestream air velocity in the test section. Additionally, the implementation of a spray removal section and reconfiguration to an open-loop wind tunnel will be discussed.

2.1.1   Secondary Contraction Design

The addition of a secondary contraction was used to increase the test section speeds in the wind tunnel. The requirements for the new contraction were as follows:

1. The total length of the contraction and the new test section should be the same as that of the existing test section (1.22 m long),

2. The maximum wind tunnel air velocity should be increased from Mach 0.17 to Mach 0.5 by reducing the test section cross sectional area by a factor of approximately 3,

3. Maintain proper flow conditioning to minimize freestream turbulence to approximately ±1%.

The desired test section length was determined based on specific study parameters and will be discussed below, but here it is sufficient to say that the secondary contraction length was determined to be 0.457 m from inlet to outlet. The inlet cross-section is the same as the original test section (i.e. 0.457 m × 0.457 m) and the desired outlet cross-section of the new test section is 0.267 m × 0.267 m. The contraction shape was determined by a 5th order

polynomial (Equation (5)) shown by Bell and Mehta [48] to provide flow uniformity while avoiding flow separation.

$$y(x) = H_{inlet} - (H_{inlet} - H_{outlet}) * \left[6 \left(\frac{x}{L} \right)^5 - 15 \left(\frac{x}{L} \right)^4 + 10 \left(\frac{x}{L} \right)^3 \right] \qquad (5)$$

This equation is for a contraction of rectangular cross-section, where y is the distance from the center of the contraction to the wall, x is the axial distance from the contraction inlet, H_{inlet} is the half-height of the inlet (center axis to wall), H_{outlet} is the half-height of the outlet, and L is the length of the contraction. The corresponding profiles of the contraction section is shown in Figure 6.
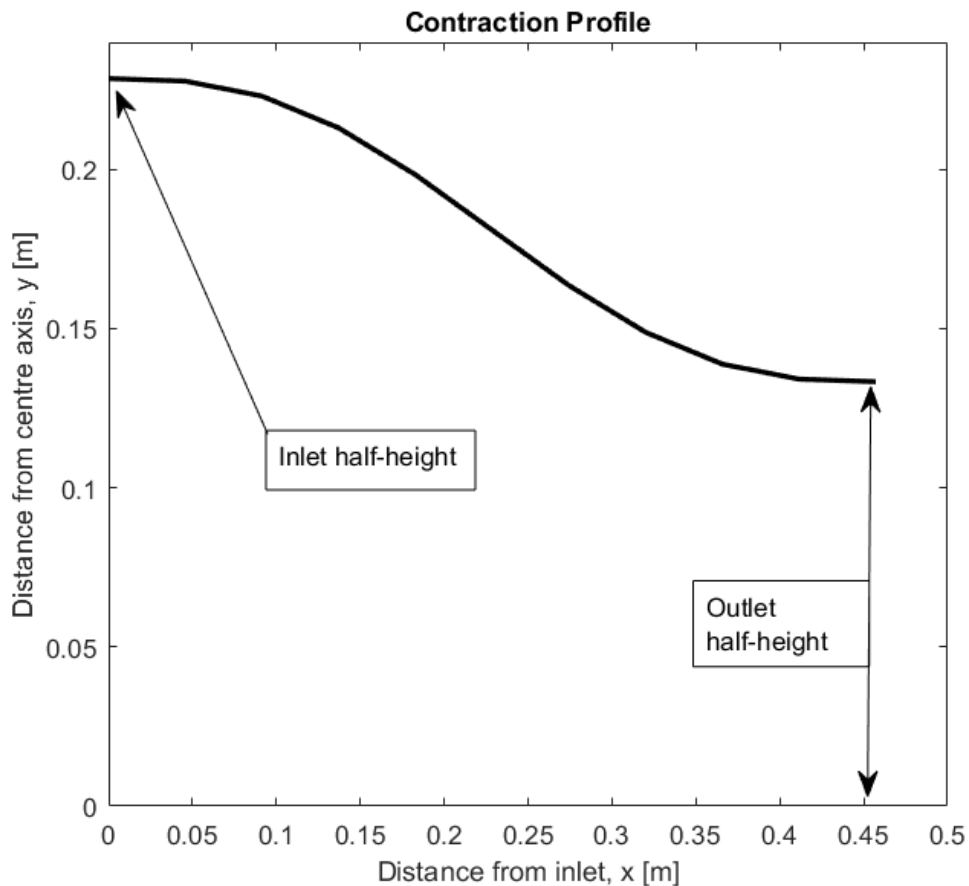
Figure 6: Profile of the secondary contraction wall. The x-axis is representative of the axis of symmetry of the contraction.

Once the contraction profile was determined, the design for manufacturing could proceed. In an effort to maintain homogeneity with part material, GFRP was considered for construction of the secondary contraction walls. After evaluating the cost and time requirements for either full or partial outsourcing of the manufacturing, it was determined that the fabrication of GFRP panels was unfeasible, as was forming the panels through other mold-based processes. Instead, the secondary contraction was fabricated from AISI 304 sheet metal by a local sheet metal fabrication shop. To achieve the desired curvature without precision forming, 16-gauge sheet metal stiffeners were laser cut with the desired wall profile and welded to the outside of 16-gauge sheets to form the walls. In addition, 3/16" plates were used to create a flange at the inlet and outlet. A 2B surface finish was specified for the inner surfaces of the wall sheets (average surface roughness of approx. 0.3-0.5µm). The finished contraction section is shown in Figure 7.

Figure 7: Secondary wind tunnel contraction

2.1.2   Test Section and Bluff Body Design

The original wind tunnel test section is modular and consists of 4 acrylic panels for optical access. An isometric drawing of the test section is shown in Figure 8 along with a set of references axis. The acrylic panels are mounted in slots within a mounting frame which is flanged to the contraction outlet and the diffuser inlet (Figure 9). The panels are fixed within the mounting frame slots using soft-tipped set screws which allow the panels to be adjusted until they are flush internally with the inlet and outlet. The panels are pulled flush against each other using plastic latches to minimize leaking out of the test section corners. Adhesive foam was also compressed in these corner gaps to ensure no air leakage.

In order to facilitate the use of the newly modified wind tunnel, the test section design mimicked the design and functionality of the original test section. For the purpose of this thesis study, the side panels of the test section contained only two holes for fixation of a bluff body, while the top and bottom panels contained holes for the insertion of a spray bar. Of the top and bottom panels, one only contained holes for the spray bar to pass through, while the other contained an opening in which a modular panel could be inserted based on the needs of the user. The current study required that this panel contain locating holes to aid in the angular orientation of the spray orifice on the spray bar.

ITEM NO.	DESCRIPTION	QTY.
1	HorizontalPanel_Modular	1
2	HorizontalPanel_Insert	1
8	VerticalPanel_BB	2
9	HorizontalPanel_SimpleHoles	1
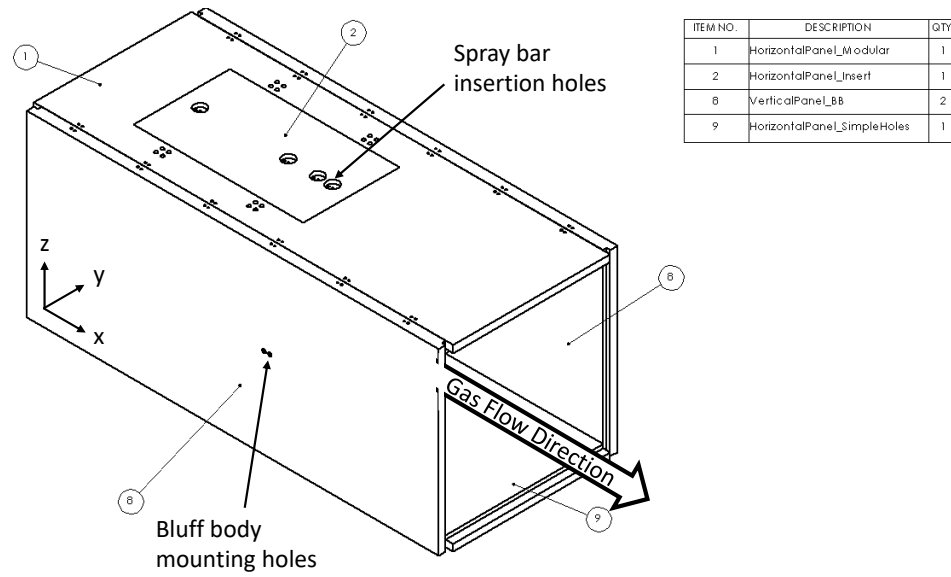
Figure 8: Isometric CAD drawing of the test section in the assembled configuration. The gas flow direction, the insertion holes for the spray bar, and the mounting holes for the bluff body are annotated for clarity. A parts list is also included identifying different panels of the test section.
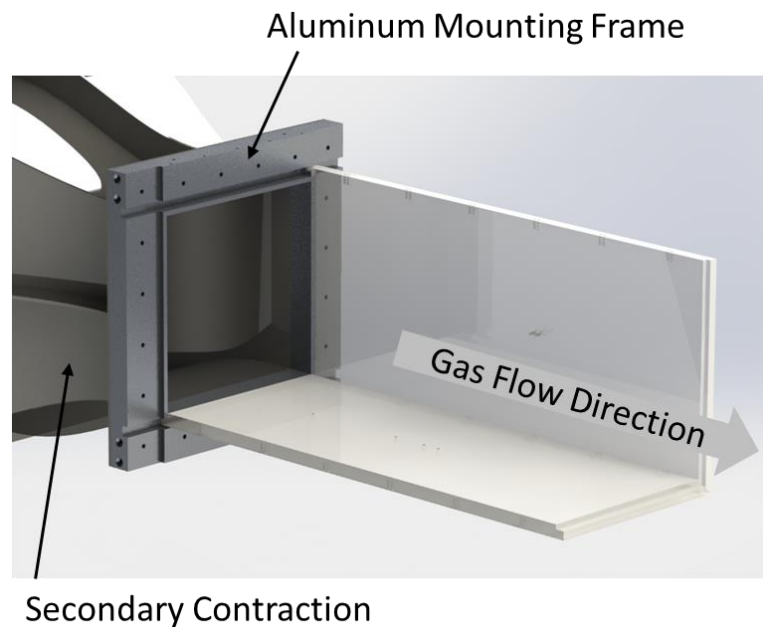
Figure 9: CAD rendering of the test section mounting frame on the contraction outlet, along with the back and bottom test section walls.

The test section length was determined to be 0.76 m (0.71 m of optical access) based on experimental parameters for the bluff body portion of the study. The three geometric considerations used to determine the test section length were: 1) The distance between the bluff body trailing edge and the test section outlet, 2) the distance between the bluff body leading edge and the spray bar, and 3) the distance from the test section inlet to the spray bar. The maximum distance between the bluff body and the spray bar was desired to be $5w_{BB}$ (where w_{BB} is the bluff body width across the trailing edge) to allow for various fractions of gas-liquid premixing upstream of the bluff body. The distance from the test section inlet to the spray bar was kept to approximately $2w_{BB}$ to avoid any flow disturbances caused by the contraction. Most importantly, the distance between the bluff body trailing edge and the test section outlet is defined by the geometry of the bluff body.

The bluff body used in this study has a 30° vee-gutter shape, i.e., a hollow bluff body with no backside or leeward surface, with a characteristic length $w_{BB} = 5.5cm$ (see Figure 10). The bluff body shape was similar to the flame holder used in the fighter jet afterburners [2]. It was fabricated by bending acrylic, resulting in a radiused leading edge rather than a sharp leading edge. This size was chosen based on common bluff body sizes as well as blockage area ratio. It is necessary to ensure that blockage effects do not cause the bluff body recirculation zone (RZ) to extend into the diffuser section.

Initial sizing of the bluff body was estimated based on previously used designs found in literature which have bluff body widths between 3.5cm and 5cm [2], [18]. Typically, the bluff body RZ is around 3 to 4 times w_{BB}, however the flow around a bluff body can be affected by wall constraints such as those found in a closed test section wind tunnel. Typically, blockage ratios of much less than 10% can be considered acceptable but not ideal for modeling unbounded flow around a bluff body in a closed wind tunnel [49]. However, in the afterburning, the bluff body is located inside the afterburner duct (i.e. within a wall bounded flow) and the area blockages are typically quite high, around 20 to 30% [50], [18]. The primary concern of blockage effects is the change in the behaviour and size of the bluff body wake. Zukoski [2] showed that the length of the wake is approximately fixed at 4 times the wake width, which was assumed to be of comparable size to the bluff body width, although a correlation by Zukoski also illustrates that a 20%

blockage ratio vee-gutter bluff body showed the length of the bluff body wake could be up to 6 times the bluff body width. Ultimately, the limited length within the new test section constrained the upper limit of the bluff body size to be around 5cm which has a 20% blockage ratio, which is consistent with the blockage ratio in a typical afterburner.

Given the reduced cross section of the test section, the mounting frames were also remade. These frames were milled out of 6061 aluminum alloy. On the test section inlet, the mounting frame was fastened to the secondary contraction outlet and at the test section outlet, the mounting frame was fastened to a newly constructed diffuser. This diffuser could not be supported by the existing wind tunnel support structure, therefore additional structural support was included between the test section inlet and outlet to help support the secondary contraction, test section, and diffuser.
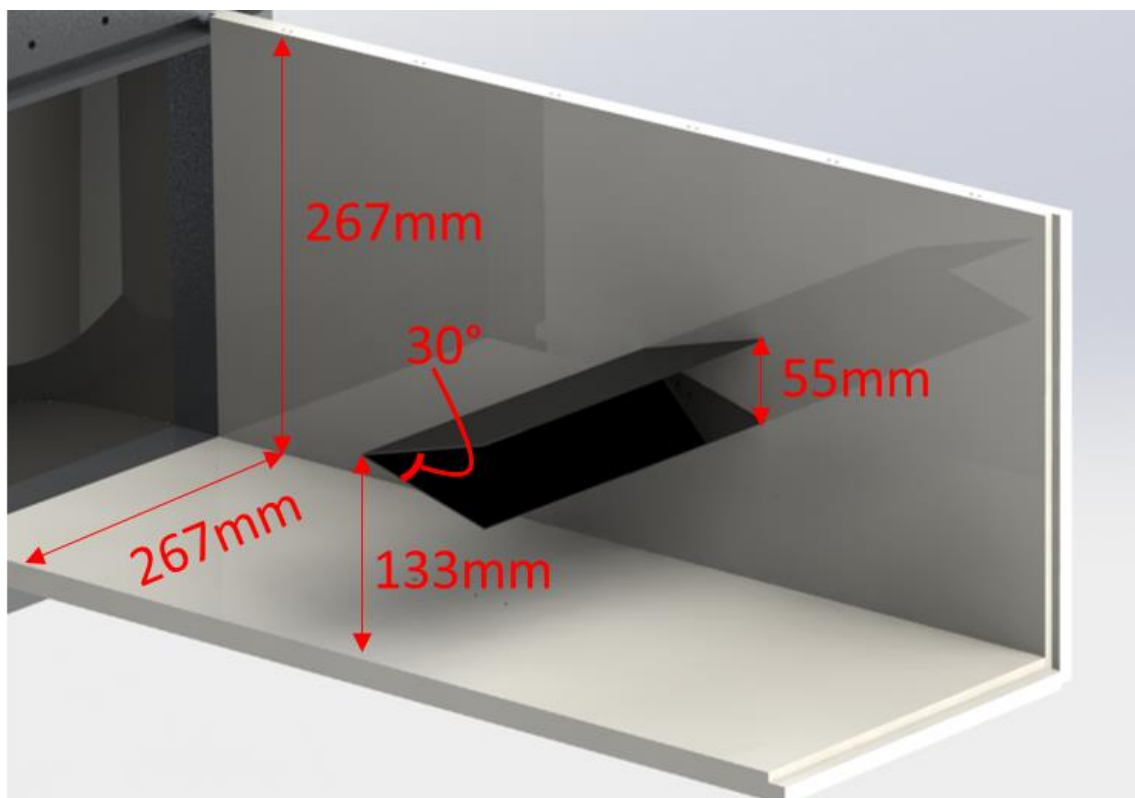
Figure 10: CAD rendering of the vee-gutter bluff body (black) within the test section (front and top panels omitted for clarity).

2.1.3   Diffuser

Given the number of components necessary to operate a wind tunnel, it is easy to overlook the importance of the diffuser. The diffuser is responsible for pressure recovery as the flow exiting the test section is fast (i.e., lower static pressure), and it is prone to fluid instability. The onset of instability greatly decreases the performance of the wind tunnel due to pressure loss, and given the desired wind tunnel speeds, poor diffuser performance can drastically affect the ability to achieve high test section velocities. In addition, flow instability increases the risk that flow near the test section outlet becomes affected by interaction with unstable/unsteady flow at the diffuser inlet. The Diffuser Data Book [51] provides an excellent reference for diffuser design. Key design parameters include the area of the inlet and outlet, the divergence angle (measured as 2 times the angle from the diffuser axis to the wall), the aspect ratio (width over height of the inlet), the area ratio (outlet over inlet), and the ratio of diffuser length over inlet height. The inlet area and length for this diffuser were fixed at 0.2667m by 0.2667m and approximately 1.62m. Given the stability map found in the Diffuser Data Book [51] as well as the Fluid Mechanics textbook by F. White [52], maximum pressure recovery, as well as fairly stable flow, can be achieved with a diffuser divergence angle of $6°$.

The diffuser is the largest part being added to the current wind tunnel. Given the unknown loading capacity of the existing support structure and the GFRP flanges of the existing wind tunnel, plywood was chosen as the construction material for the diffuser given its strength to weight ratio. Specifically, 19mm thick sheets of plywood were used due to its estimated bending stiffness, crucial to reducing response to potential vibrations created via unsteady diffuser flow. The surface of this plywood was also smooth and free of visible damage which may lead to loosening and release of wood debris into the wind tunnel. An aluminum screen mesh was also added at the diffuser exit to reduce the risk of foreign object debris.

2.1.4   Spray Removal

The only working fluid typically used in the wind tunnel is air and seed particle, which in the present study is composed primarily of dipropylene glycol in n a fine mist (droplet

diameter on the order of 1µm [53]). The introduction of any bulk liquid into the wind tunnel environment may risk causing unnecessary corrosion or pooling of the working liquid within unreachable areas of the wind tunnel. It is desirable to operate in closed-loop configuration due to higher achievable levels of control over the seed particle concentration, as well as over the temperature of the air.

A commercially produced mist eliminator (Munters T100 Impingement Separator – Fort Myers, FL, USA) was purchased in the hopes that it would remove 100% of the liquid injected through the spray bar during experimentation (see Figure 11). The mist eliminator consists of a polypropylene vane pack in which the vanes are aerodynamically engineered for minimum performance loss; the expected pressure drop is around 100Pa at the designated gas velocity. As air carrying various sizes of droplets passes in between the vanes, the vanes cause the air to briefly change directions and the inertia of the liquid droplets forces the droplets into a collection channel. Liquid that collects in this channel drains with the aid of gravity. Limited resources necessitated that the operating gas velocity at the mist eliminator be larger than the design velocity. This led to high amounts of water removal, but due to incomplete (<100%) removal the decision was made to operate the wind tunnel in open-loop configuration to ensure all liquid was confidently removed. Fortunately, the open-loop configuration was able to achieve test section velocities equivalent to that of the close-loop configuration.
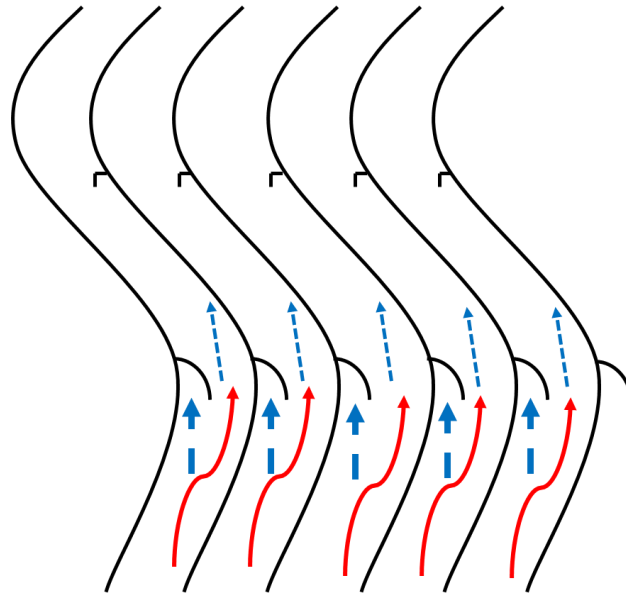
Figure 11: Illustration of the vane profile. As the air flows around the first bend, the large droplets (thick dashed arrow) are carried into the first channel due to the droplet's inertia. As the air flow (solid arrow) continues along the vane profile, the smaller droplets (thinner dashed line) are forced into the second channel.

2.2   Spray Delivery System

Jet-in-crossflow studies have historically been performed by injecting the liquid jet through an orifice flush with the test section wall. In practice, spray is injected through spray bars, fuel nozzles, and occasionally, through the walls of a bluff body. Afterburners have been known to use simple injection mechanisms such as spray bars or ring manifolds with many small orifices, rather than fuel nozzle such as those used in primary gas turbine combustors.

In the present research, the gas flow surrounding the jet-in-crossflow spray is of interest so a single spray bar with a single orifice was used to inject the liquid jet. Figure 12 illustrates the positioning of the spray bar within the test section as well as the location of the injection orifice which is used as a point of origin throughout this study. The spray is injected in the y-direction. The spray bar was constructed using 4 mm OD stainless steel tubing with a 2 mm ID. The spray bar was straight and extended across the entire test section in order to simulate the 2D behavior of a spray bar (see Figure 13). The spray bar material was chosen to allow for the use of different liquids without risk of corrosion. The spray bar contained a singular orifice 0.8 mm in diameter (see Figure 13).
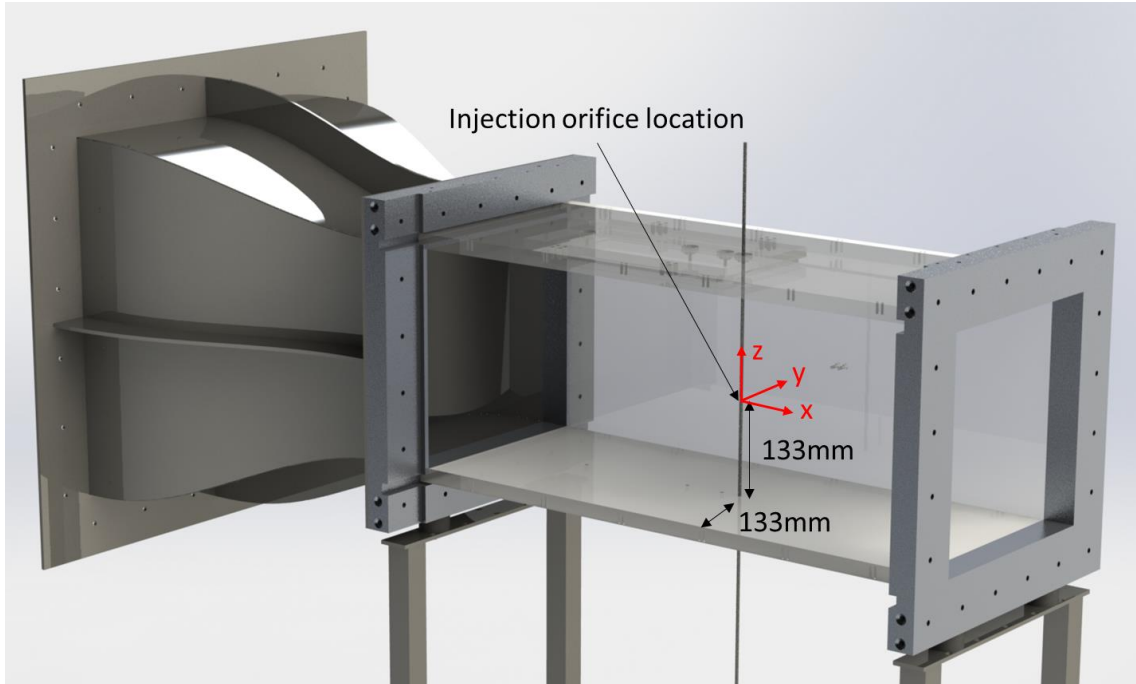
Figure 12: CAD rendering of the working section of the wind tunnel, illustrating the placement of the spray bar and the location of the injection orifice which is used as a point of origin. The liquid jet is injected in the y-direction.

Figure 13: Setup of the spray bar in the test section

One of the test section panels contains locating holes used to precisely control the angular orientation of the spray bar. An aluminum collar was constructed which could be fastened to the spray bar. This collar contains a set screw with an extended tip which fit within the locating holes in the test section panel (see Figure 14). Multiple locating holes allow the orifice to be oriented from 0° (facing upstream/counterflow) to 180° (facing downstream/co-flow) in 30° increments.
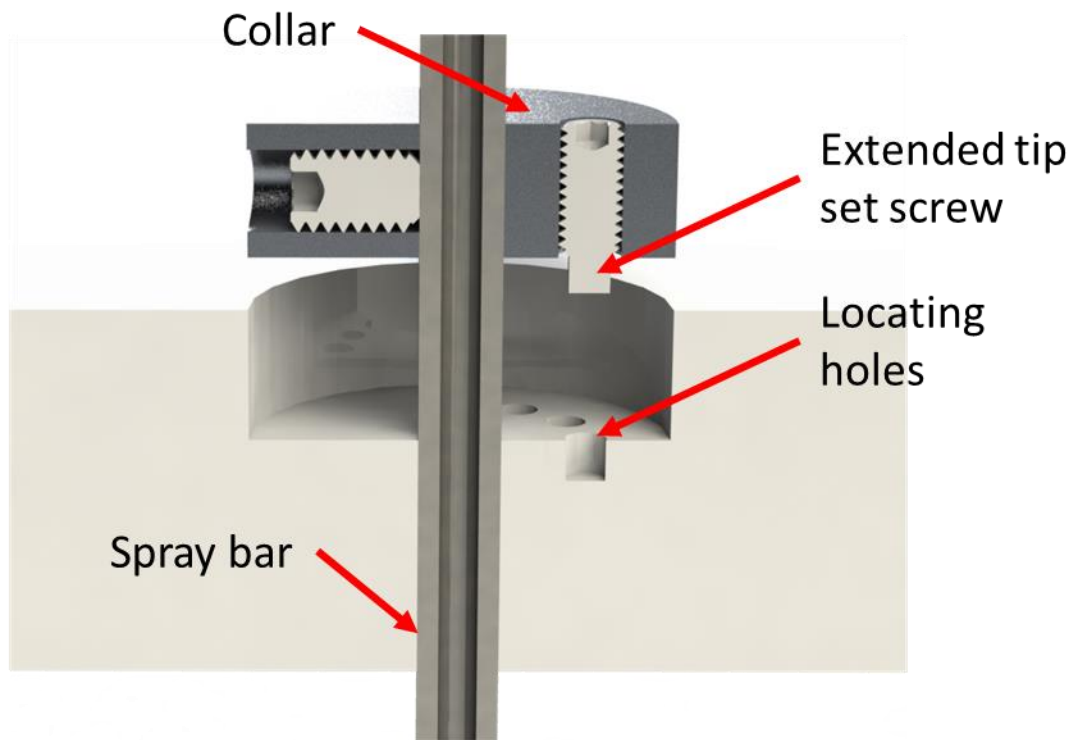
Figure 14: CAD rendering of a section view of the locating mechanism used for angular orientation of the spray bar

Given the length and small inner diameter of the spray bar, the pressure required to deliver the fluid is expected to create some design challenges with regards to the pumping system. Two methods of circulating fluid through the spray bar were considered; the first is to use a pump with a reservoir large enough to supply continuous flow for up to several minutes, and the second is to use a pressurized reservoir with flow rates controlled using valves.

In order to evaluate the pump option, an estimate of the system losses would be required in order to be able to begin narrowing down the selection of pump types. The desired injection velocity for jet-in-crossflow tests using gaseous air and liquid water for a gas crossflow velocity of 35m/s range from approximately 3.8 m/s to 16.3 m/s, using an injection orifice of 0.8 mm in diameter, to achieve the desired momentum flux ratio range of 10 to 180. This corresponds to an approximate liquid flow rate range of 0.1 liters per minute (lpm) to 0.5 lpm. The injection orifice diameter was chosen based on the diameter of the injection orifice of an existing, proprietary injector design made available for this project, and the range of momentum flux ratio was determined based on existing work relating to jet-in-crossflow for aeroengine application [44], [47], [54]–[56]. An estimation of head loss from the reservoir to the injection orifice was performed based on a preliminary experimental setup and after accounting for friction losses in both the spray bar and the tubing, as well as component losses caused by valves, tees, and other fittings, it was determined that losses on the order of 69 kPa at a relatively low flow rate would require some type of positive displacement pump. Some fuel pumps were also considered but typically had low pressure capacity for the desired flow rate.

A positive displacement pump (PDP) was purchased capable of flow rates up to 4 lpm in a zero-loss system, as well as having a maximum pressure rating of 0.69 MPa. The high-pressure rating was chosen to account for major additional losses caused by using a valve to throttle the flow rate. However, upon testing the system, pressure gage readings were consistently above 0.345 MPa even when the pump was operated under reduced power (e.g., 2 lpm). Any attempt to further reduce pump power in order to reduce pressure would cause the pump to shut down. The pulsatile flow created by the PDP was not completely damped at the injection orifice and the liquid jet exhibited undesirable periodic behavior. Throttling of the PDP flow rate using a globe valve did not provide adequate flow control. Ultimately, the described performance of the pump system in combination with project time constraints led the exploration of the second option.

The use of a pressurized liquid reservoir has the advantage that system losses caused by throttling the flow rate do not put any strain on any mechanical components as it would with a pump. Figure 15 illustrates a diagram of the final liquid delivery system. Pressurized

air lines in the lab capable of up to 0.965 MPa output were used to control the static pressure of a pressure vessel rated for 0.483 MPa. A pressure regulator was used at both the 0.965 MPa line as well as the tank inlet to ensure that pressure vessel limits were not exceeded. Both locations were also equipped with shutoff valves. A pressure relief valve rated for 0.483MPa was located at the top of the tank, and a separate nozzle was fitted with a shutoff valve for pressure relief when the tank was not in use. Located toward the bottom of the tank, within the area expected to contain liquid, was an inlet used to fill the tank with water, and an outlet leading to some instrumentation, flow control valves, and the spray bar.
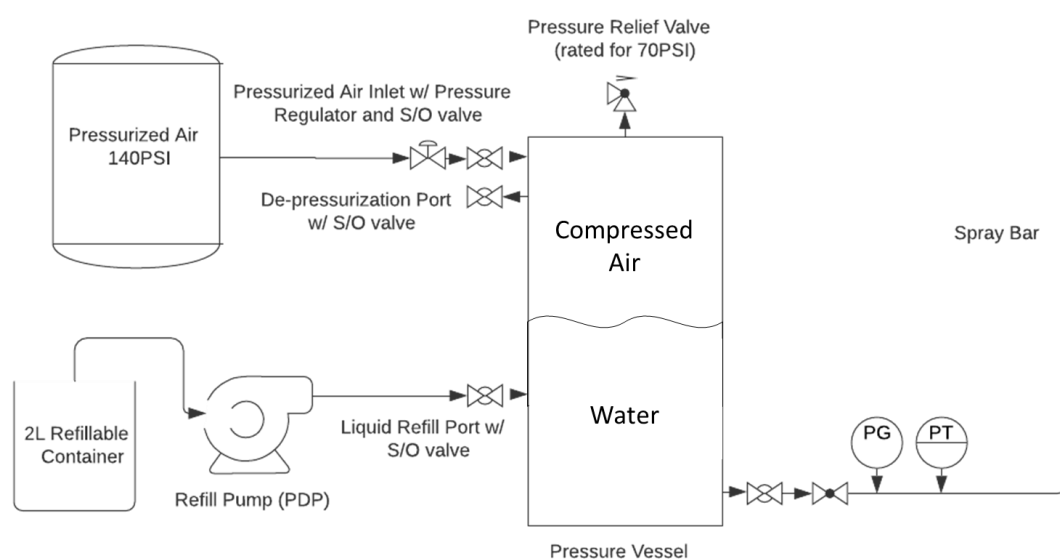
Figure 15: Piping and Instrumentation Diagram (P&ID) of the spray delivery system. (PG: pressure gage, PT: pressure transducer)

A "stopwatch and bucket" method was used for flow rate calibration. The flow rate was measured by weighing the water exiting the injection orifice with a scale (axGear Digital Scale) over a fixed period of time. The uncertainty associated with determining the flow rate using the pressure transducer was determined to be ±19.2% at q of 10 primarily due to increased uncertainty in the pressure transducer at low flow rate. The uncertainty reduced substantially at higher q values and was ±7.5%, ±3.0%, and ±1.7% for q of 20, q of 60, and q of 120 respectively. The time was repeatably determined by recording (at 30 frames per second) the output display of the scale and checking the initial mass and the final mass

after a fixed number of frames. By measuring the flow rate simultaneously with pressure, a calibration curve (see Figure 16) was created for spray delivery system. The coefficient of determination (R^2 value) for the line of best fit equation was 0.9994 indicating close agreement with experimental data. An Omega model PX309-100A5V pressure transducer with an accuracy (linearity, hysteresis, and repeatability) of ±6.9kPa (±10.34kPa @ 34.5kPa system pressure) was used to record the pressure at the lowest point in the system (Figure 15). Data from the pressure transducer was monitored and recorded using LabVIEW instrumentation software and the flow rate was accurately determined using the calibrated system curve.
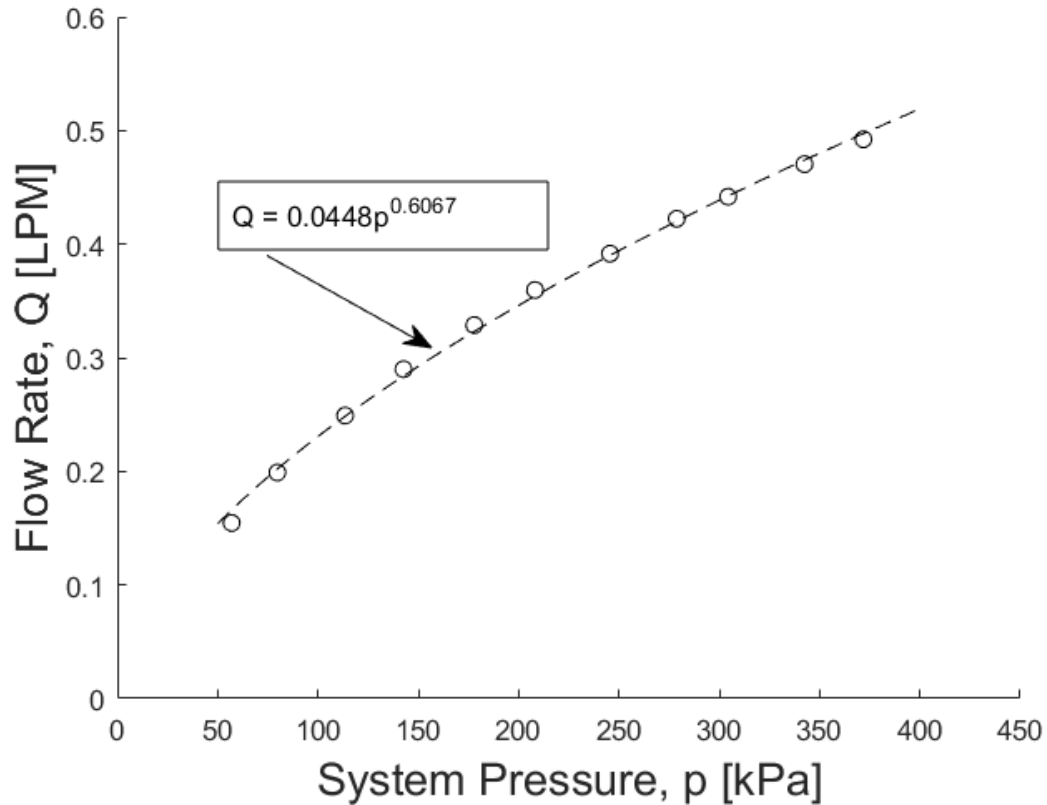
Figure 16: Spray delivery calibration curve used to control the liquid injection rate.

2.3   Free Spray Particle Image Velocimetry (PIV)

The first part of this thesis study, the base characterization of a jet-in-crossflow and a jet-in-counterflow, utilizes PIV to investigate the flow field around the spray and to detect and identify droplet sizes and their distribution. PIV is an optical flow measurement technique which measures flow velocities simultaneously over a plane, providing a high-resolution map of velocity vectors, describing detailed behaviour of the flow field under investigation. A PIV system requires carefully aligned optics to visualize the flow, an image acquisition system to capture the tracer particles in the flow, and a data processing algorithm to compute velocity vectors fields based on the movement of tracer particles.

2.3.1   PIV Setup and Experimental Parameters

PIV requires that the fluid under investigation be seeded with tiny particles capable of reflecting, refracting, or emitting some source of light. The particles must be neutrally buoyant so that they follow the flow accurately. Typically, the Stokes number, given in Equation (6), is used to determine whether a given particle is suitable to act as a tracer (Stk << 1). The Stokes number is characterized by the relaxation time of the particle t_p, which describes the time required for a particle of characteristic length l_p to respond to the motion of the surrounding flow at a velocity of U.

$$Stk = \frac{t_p U}{l_p} \qquad\qquad (6)$$

In the present study, Theatrical fog was used as tracer particles. It comprised of Director's Choice Fog Fluid (Ultratec Special Effects Inc. - London, ON, Canada), which is primarily composed of dipropylene glycol. A fog machine was used to create the fine mist of liquid droplets. Given that the tracer particle chosen satisfies the requirement defined by the Stokes number, the particles are considered to accurately follow the flow and the motion of these particles can be tracked to determine the motion of the fluid under investigation. For seed particles used in this study, the Stokes number was determined using Equations (6) through (8). If the Reynolds number of the particle, where the characteristic length is the particle diameter d_p, the characteristic velocity is the freestream velocity U, and the density and viscosity are that of the gas surrounding the particle ρ_g and μ_g, is less than 1

($Re_p < 1$), then the inertial forces of the particle are considered negligible compared to the viscous forces and the particle relaxation time can be determined using Equation (7). Substituting Equation (7) into (6) and rearranging the terms results in Equation (8) which shows that if the Re_p and the density ratio ρ_p/ρ_g are on the order of 1, then Stk < 1 must follow.

$$t_o = \frac{\rho_p d_p^{\,2}}{18\mu_p} \qquad\qquad (7)$$

$$Stk = \frac{Re_p}{18}\frac{\rho_p}{\rho_g} \qquad\qquad (8)$$

Using a maximum particle diameter of 1μm and a freestream velocity of 35m/s, the Re_p was determined to be 2.3, and with a density ratio ρ_p/ρ_g of 4.63 the resulting Stk is 0.6. This is larger than *Stk* of 0.1 which has been shown to result in particle tracing accuracy errors of less than 1%, however it remains less than unity [57] and therefore seed particles up to 1μm have reasonable accuracy for PIV applications.

To obtain PIV images, a laser sheet illuminates a 2D region of interest and Mie scattering of the particles is captured by a camera. Mie scattering is the process by which light is scattered by a spherical particle of comparable size to the wavelength of incident light, and the scattering intensity is proportional to the particle's size. Therefore, the seed particles scatter light with more intensity than the background flow which allows the particles and background to be distinguishable. This also applies to liquid droplets less than 1 mm in diameter.

The PIV setup described here served two purposes. First, this study aimed to simultaneously investigate the behaviour liquid droplets and surrounding gaseous flow for jet-in-crossflow and jet-in-counterflow using PIV and image processing techniques. Second, it provided a base characterization which formed the foundation for the following bluff body study.

Figure 17 shows the PIV setup used for the free spray study. A 120 mJ dual-cavity Nd:YAG laser (120XT 532nm, SoloPIV) was used as the light source. Each cavity in this laser device

emits a beam at a rate of 15Hz with a pulse width of 3 to 5ns which is passed through a cylindrical focus lens to create a laser sheet or plane as well as a spherical focus lens to aid in reducing the laser sheet thickness to approximately 1mm. When the laser sheet interacts with the seeded flow Mie scattering occurs, as previously discussed.

The laser sheet thickness of 1mm is the smallest achievable with the equipment available and it is larger than the injection orifice which is 0.8mm in diameter. However, the investigation of the spray droplets primarily concerns the investigation of droplets sub-millimeter in size and the flow surrounding these droplets. Therefore, the similarity in size of the injection orifice and the laser sheet thickness is of no concern.

Images of the flow were acquired using a 12MP CCD camera (IO Industries Flare) at a resolution of 4100×3072 pixels with a field of view of 185 pixels/cm. The camera was equipped with a Nikon AF NIKKOR 50mm, f/1.4 lens. The image acquisition system is comprised of two digital video recorders (DVRs, IO Industries DVR Express CORE) in which the minimum achievable inter-frame time, which is typically limited by the image capture rates, could be reduced by clever synchronization of the lasers with respect to the camera exposure timing and DVR recording rates. This method greatly reduces the time between images in pair, while keeping the camera and laser rate of 15Hz from one pair to the next. The time separation between images in pair was $\Delta t = 39$ μs while time from one pair to the next was $\Delta t = 1/15$s. Synchronization between the camera and PIV system was achieved by passing the camera trigger through a pulse/delay generator (Berkeley Nucleonics model 575) to the PIV system. Background reflections were minimized by covering background surfaces with 50μm thick matte black aluminum foil (Cinefoil, Rosco Canada).
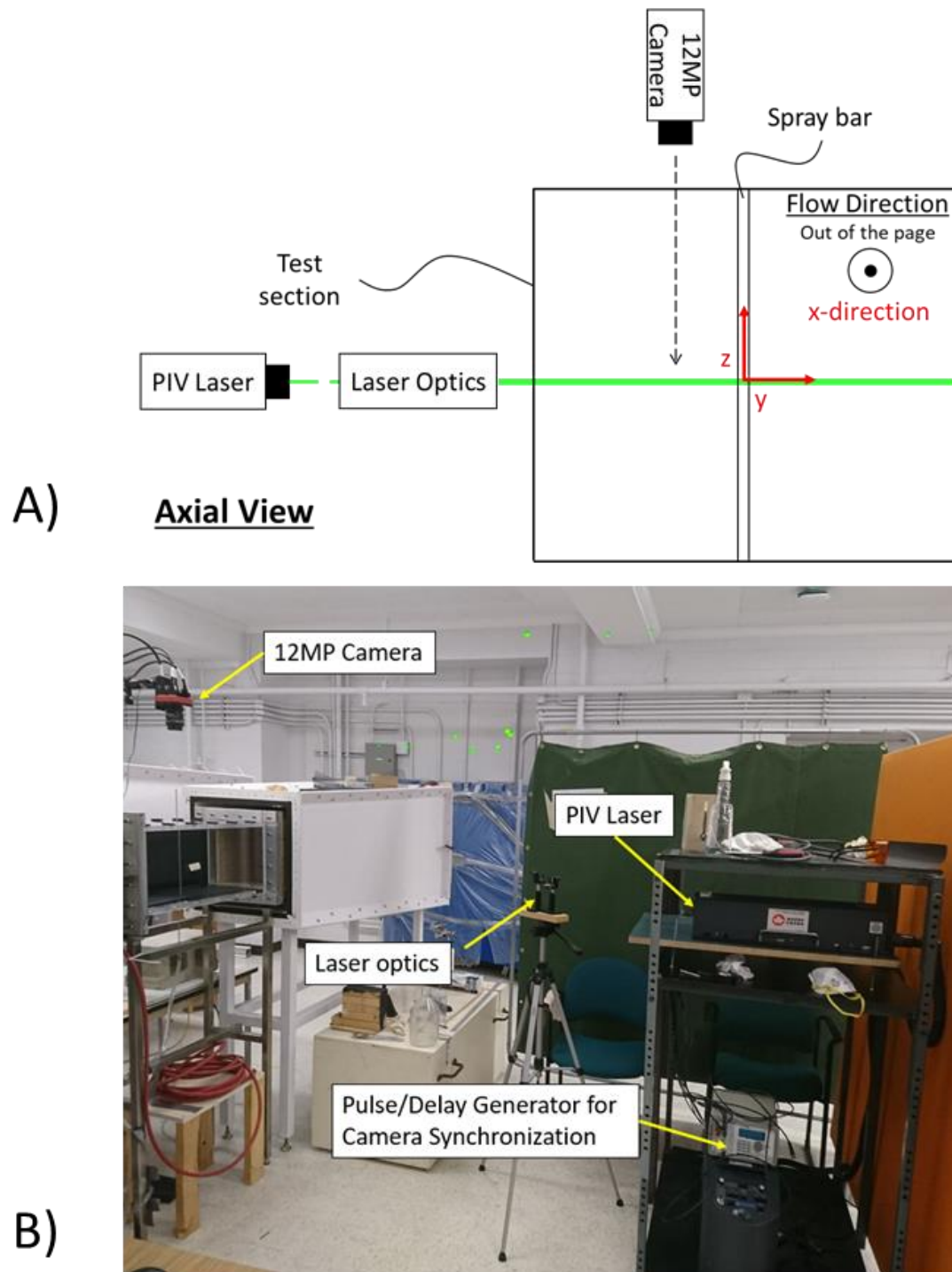
Figure 17: A) View of a cross section of the test section looking upstream. The PIV laser enters from one side of the test section while the 12MP camera views the laser sheet from above. B) Labeled Photograph of the PIV setup for the first study.

In order to study the jet-in-crossflow/counterflow fluid dynamics, the spray bar was inserted through the vertical span of the test section in such a manner that the bar created a 2D cylindrical wake. This is representative of the configuration of the injectors found in many afterburners in which the injectors span across the annular inlet diffuser (from the outer afterburner casing to the diffuser inner cone). A schematic diagram is shown in Figure 18 illustrating the 2D plane under investigation and identifying the directions of flow as well as key areas which will be examined. The locating mechanism shown in Figure 14 was used for precise angular orientation of the liquid jet with respect to the gas flow. Various momentum flux ratios were investigated by changing the liquid mass flow rate and keeping the freestream air speed constant. The parameters for the first study are shown in Table 1. The jet Reynolds number Re_l was defined using the properties of water, ρ_{water} and μ_{water}, the injection velocity of the jet, $v_{injection}$ which is dependent on q, and the diameter of the injection orifice, d_o. The spray bar Reynolds number Re_{sb} was defined using the properties of air, ρ_{air} and μ_{air}, the freestream gas velocity, $\overline{u_\infty}$, and the diameter of the injection spray bar, d_{sb}.
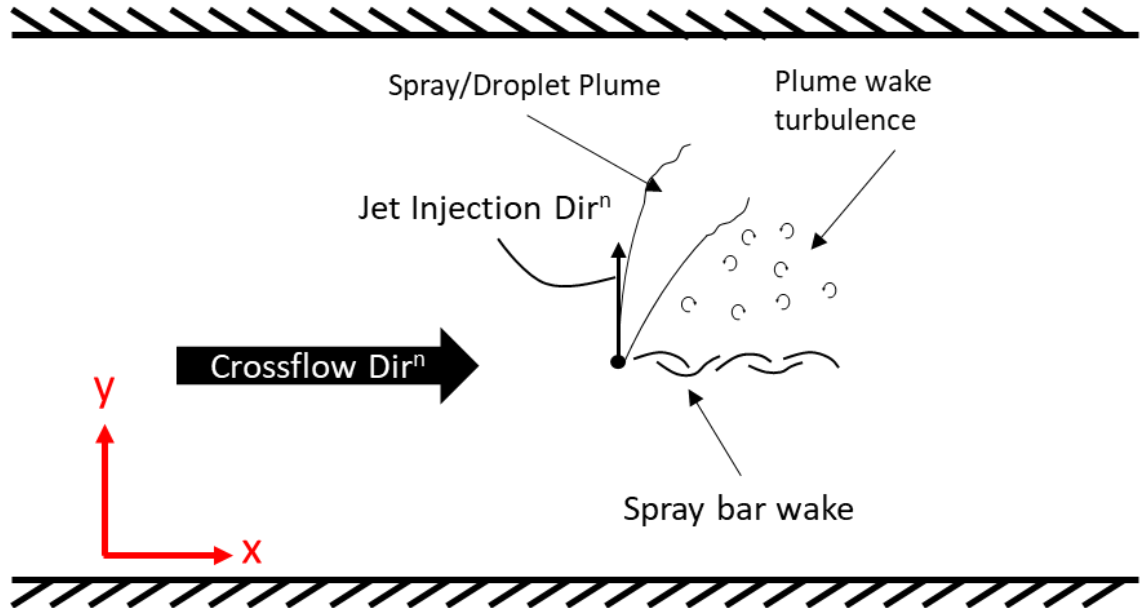
Figure 18: Schematic diagram of the 2D under investigation (not to scale). The direction of gas and liquid flow are identified, along with key regions of interest including the spray plume, the plume wake, and the spray bar wake.

Table 1: Study conditions for the free spray configuration of the jet-in-crossflow/counterflow.

Parameters	Values
Gas	Air
Gas Velocity, v_g [m/s]	35
Gas Temperature, T_g [°K]	295 to 296
Gas pressure, P_g [kPa]	101.3
Gas Density, ρ_g [kg/m^3]	1.2
Gas Relative Humidity, ϕ_g [%]	35 to 70
Liquid	Water
Liquid Velocity, v_l [m/s]	3.8 to 13.3
Momentum flux ratio, q	10 to 120
Weber gas number, We_g	16
Liquid Jet Reynold number, Re_l	3000 to 10600
Spraybar Reynolds number, Re_{sb}	9333

2.4   Bluff Body High Speed Imaging (HSI)

The purpose of this second investigation was to examine the two-phase flow behaviour around the bluff body. However, the present study will only examine the droplet behaviour using high-speed images. The bluff body study first examines droplets qualitatively to discuss behaviours which could only be observed using HSI, followed by a quantitative analysis of the droplet sizes, distributions, and velocity magnitudes. Although both the free spray and bluff body experimental setups were designed with variability in mind, such as the ability to change the distance between the spray bar and bluff body, a fixed configuration was used for this study due to unforeseen timeline constraints imposed by the COVID pandemic.

High speed imaging is a photographic technique which produces images at a high sampling rate, and typically at very fast shutter speeds. When used to capture events of objects in motion, the displacement of the objects from frame to frame is reduced. The motion of objects can therefore be tracked closely between successive frames. If an object if moving too quickly to be captured without motion blur, the shutter speed can be increased to

"freeze" the appearance of the moving object. Both a higher sampling rate and an increased shutter speed come at the cost of reduce exposure time on the photosensors of the camera, therefore requiring increased lighting to illuminate the objects under investigation.

In the bluff body study, high speed imaging was used to capture the behaviour of droplets in the vicinity of a bluff body. In order to provide illumination for proper exposure of the droplets, a continuous wave laser (15 W DPSS, 532 nm, Laser Glow Technologies) was used in a configuration very similar to the PIV configuration used for the free spray configuration (Figure 19). A schematic diagram is shown in Figure 20 illustrating the 2D plane of investigation along with key regions of interest such as the bluff body recirculation zone.
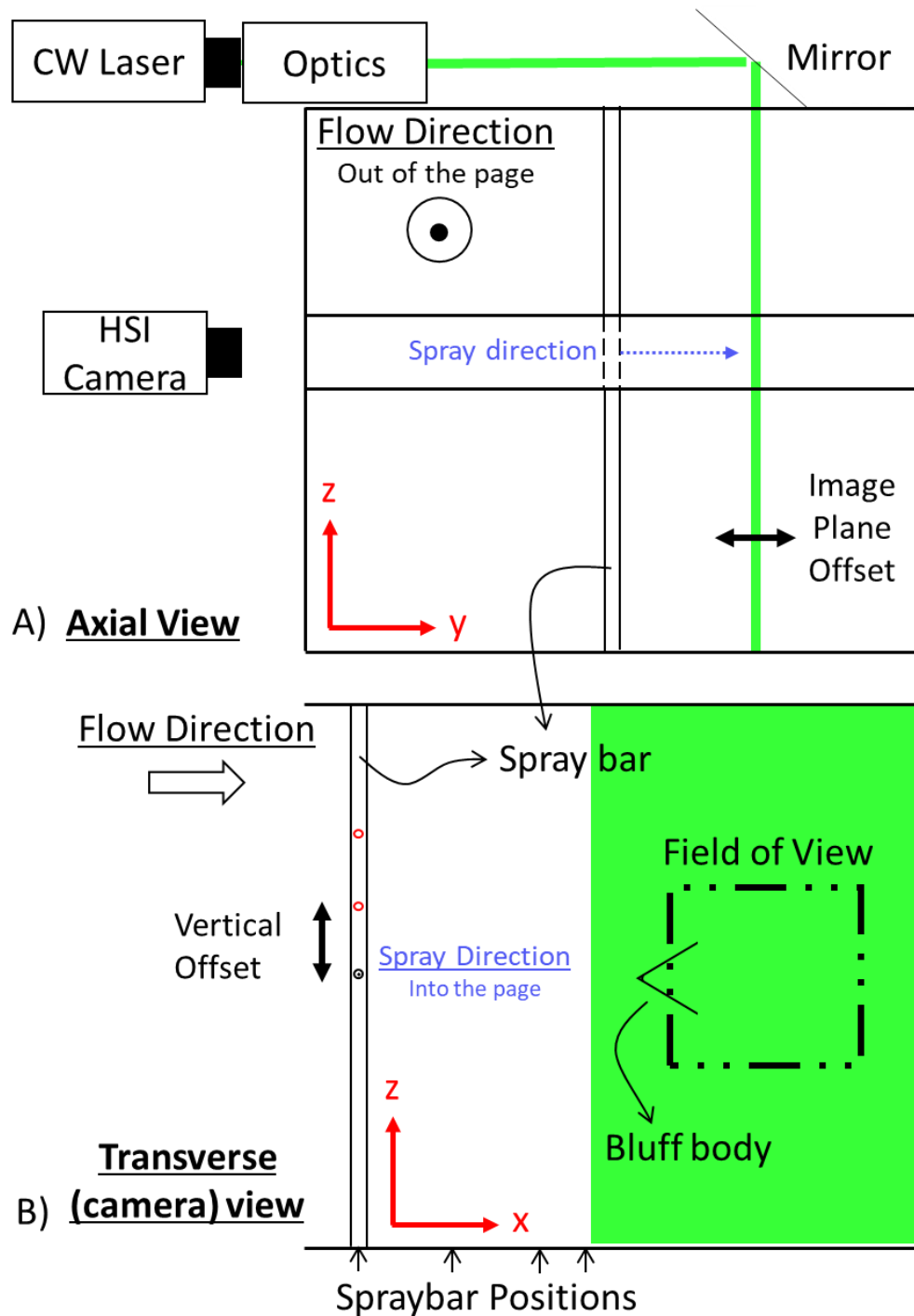
Figure 19: A) View of the test section cross section illustrating the change in equipment position as well as the plane offset created by movement of a mirror. B) View of the illuminated 2D plane from the camera's perspective, illustrating the various spray bar related offset positions.
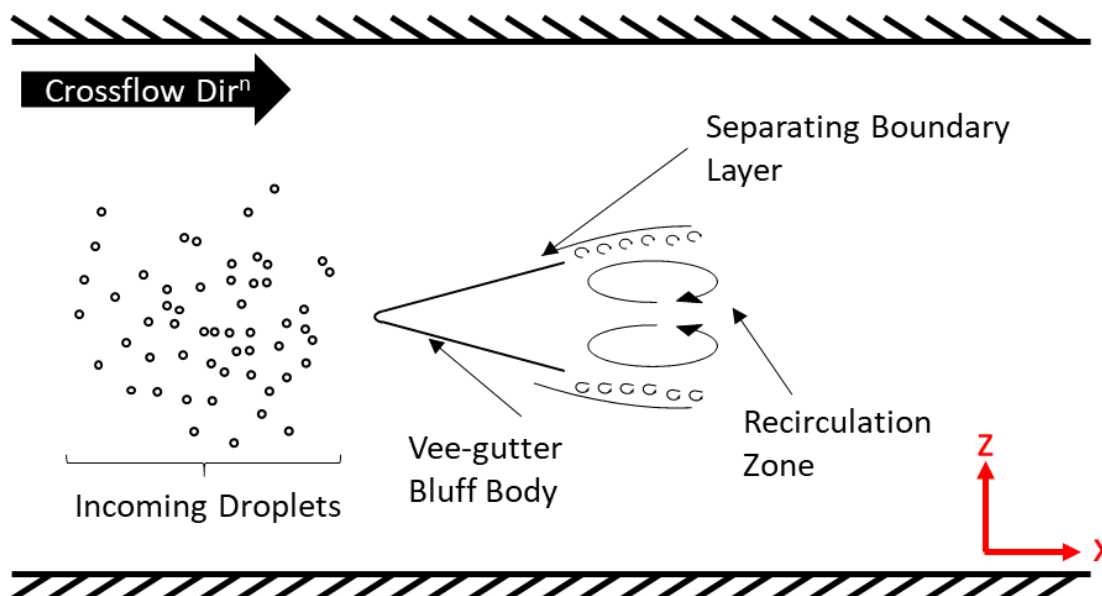
Figure 20: Schematic diagram of the 2D plane of investigation (not to scale). This diagram illustrates the oncoming droplets relative to the bluff body, as well as the general shape of the vee-gutter bluff body and the recirculation created in the bluff body wake.

2.4.1   HSI Setup and Experimental Parameters

The high-speed camera used is a Photron Fastcam SA5 which was operated at a fixed frame rate of 8,000 frames per second which corresponds to a frame-to-frame $\Delta t = 125\mu s$. Although this is 3.2 times the Δt between paired images from the PIV study, it is much faster than the time between PIV pairs, and this frame rate was found to be sufficient for proper droplet illumination as well as qualitative tracking via frame-by-frame playback. Also, camera field of view was limited by frame rate and 8,000fps provided a sufficiently large field of view (resolution: 896×752, scale: 62px/cm) to capture the bluff body trailing edge and some of the surrounding freestream. Two image exposures were used. First, images were captured using a vert short frame exposure time of 8.26μs. This essentially provided a "freeze frame" of the droplets to eliminate any motion blur created at 8,000fps. These images were used to determine droplet sizes and their distribution similar to the PIV droplets. Second, a longer exposure time of 50μs was used to create streak images for droplet velocity computations (Figure 21). This time was sufficiently long to create streaks which were sufficiently long for the algorithm to detect the particle's shift during the

exposure time and the streak shape to remain linear in shape. A non-linear shape would indicate 2D motion over the exposure time of the image, making the estimation of velocity magnitude more complex, requiring information about the vector orientation which currently has not been estimated.
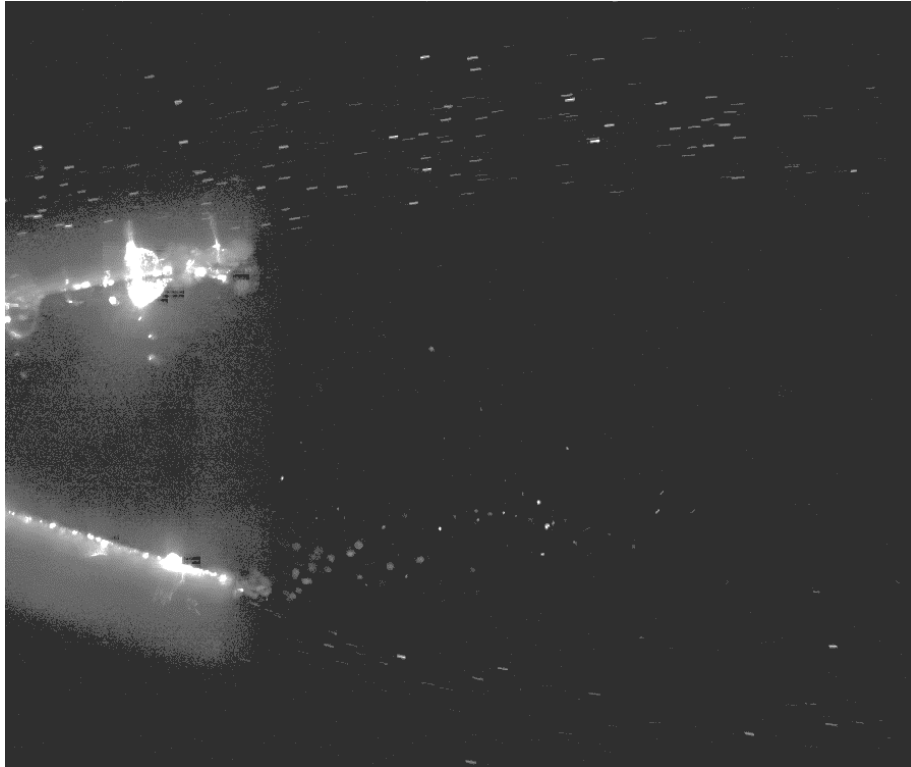
Figure 21: Image from the high-speed camera illustrating the streaks created by droplets travelling at high velocity. The streaks are primarily observed above the upper portion of the bluff body.

As mentioned earlier, for illumination, a continuous wave (CW) laser was used in a setup similar to the PIV setup for the free spray configuration (Figure 19). The output beam was passed through a 30° sheet diffuser, and the resulting sheet was then reduced in thickness using a spherical lens, resulting in a sheet thickness of ~1mm within the test section.

The spray bar was located $2w_{BB}$ upstream of the bluff body trailing edge, and the laser sheet was placed at $y \cong +70d_o$ which is the location corresponding to the bulk of spray volume for q=20.

For all experimental tests using HSI, a total of 3,000 images were captured at a frame rate of 8,000 Hz which results in a total time elapsed per recording of 0.375 seconds. The number of images acquired during each run was restricted by the on-board memory of the high-speed camera. The chosen frame rate was determined to be a good compromise between image resolution (which decreases with an increase in frame rate) and temporal resolution of droplet motion. Images were taken from continuous recordings, and therefore, were not randomly sampled.

The momentum flux ratios examined for the bluff body work were q of 20, 30, 40, 50, and 60. It was concluded that due to time constraints, only a fixed configuration would be examined, i.e., the spray bar, bluff body, and investigation plane would be only measured at one fixed location each. In order to get the most data, it was decided that the laser sheet be placed in a location were the majority of droplets at q of 20 would pass over the bluff body. In the PIV study, the q of 20 spray was found to be mostly visible in the field of view, while higher flux ratios (60 and 120) were not entirely in view. For the lower q of 10, jet penetration would be insufficient to reach the investigation plane. At any q greater than 20, shearing from the spray column would still be visible therefore they were not excluded from the analysis.

2.5   Methodology

Following acquisition of the PIV images for all desired tests, data processing is required to extract any useful information about the mean and turbulent flow fields and the liquid spray behaviour. The data processing methodology consists of a classical PIV image processing method which uses a fast Fourier transform (FFT) to perform image cross correlation to track the displacement of seed particles. A droplet detection algorithm, capable of extracting information such as droplet size and quantity, was also developed. Both codes were developed in-house using MATLAB and can be performed independently of each other, although the removal of droplets from PIV images improves the quality of the PIV data. As such, a less robust but less computationally expensive version of the droplet detection algorithm was utilized to remove droplets pre-PIV processing. These methodologies were also intended for the bluff body portion of the study however, due to unforeseen interruptions (equipment malfunction and COVID-19 pandemic) the bluff body

study was conducted using HSI techniques. Droplets were identified in size using short-exposure images and the same algorithm mentioned above, while droplet velocity magnitudes were determined using long-exposure images to create droplet streaks. Gas velocities were not determined in the bluff body study. All image processing and data analysis for the bluff body study was also conducted using in-house MATLAB code.

2.5.1   PIV data processing

PIV data analysis was performed using an in-house MATLAB code, which performs a fast Fourier transform (FFT) correlation to track groupings of seed particles (pixel pattern) using a 64×64 pixels interrogation window and 128×128 pixels search window. To increase the nominal resolution of the velocity vector fields, 50% overlap between consecutive interrogation windows were used, resulting in a vector field with 32×32 pixels per vector. Vector outliers were corrected using adaptive Gaussian weighting and a local median test.

2.5.1.1   Pre-processing

The code begins by pre-processing the images to remove stationary background information and to reduce noise in the image. A background image is used to subtract stationary objects from the primary PIV image wherever a background "object" was highly visible (gray value > 100). This process removes any static background, as well as droplets which are dynamic and change from frame to frame. Pre-processing is concluded by performing a convolution on the image using a Gaussian convolution kernel of size 3×3 pixels to reduce noise within the image.

2.5.1.2   Vector Field Computation

The main PIV processing occurs between 2 successive PIV images or frames, the so-called image pair. The interrogation window, which is a 64×64 pixels section of the PIV image, is retrieved from the first chronological frame of the pair (Figure 22) and a Gaussian mask equal to the size of the interrogation window is applied which increases the importance of tracking the central pixels. The interrogation window is then searched for within a 128×128 pixels search window in the second frame of the image pair using a FFT correlation. This

returns a spatial frequency map which identifies correlation peaks between frames (i.e., regions where the pattern of tracer particles between the interrogation and search windows strongly correlate). From the largest correlation peak, the most likely direction of tracer particles' movement (i.e., flow motion) can be determined, resulting in a vector with both magnitude and direction. The process is continued for all interrogation windows in the image, providing a velocity vector field for each image pair.

Once the displacement vector is determined, this vector magnitude is compared with the central mean of the eight nearest neighbouring vectors. If the difference between the chosen correlation peak and the central mean of neighbours is within acceptable limits, then the chosen peak is used for further processing.
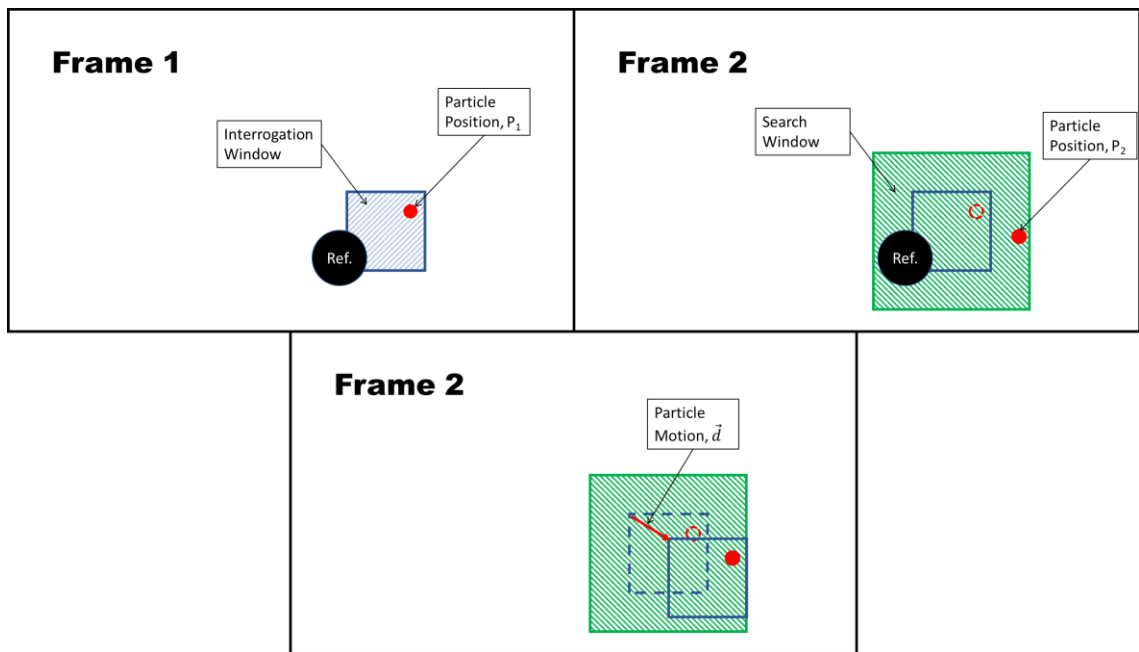
Figure 22: The interrogation window is taken in the first of two consecutive frames and the searched for within the search window in the second frame (top). When the peak correlation is found between the interrogation and search windows (bottom), the vector displacement can be determined.

2.5.1.3   Spurious Vector Correction

The full displacement vector field needs to be examined in order to identify and correct any spurious vectors. The two methods used to correct spurious vectors are local median filtering and adaptive gaussian weighting. Often spurious vectors are created in locations where visual obstruction exist; therefore, a mask is applied before proceeding with vector correction in order to remove vectors in regions of the image where no data is obtainable or where obstructions resulted in bad vectors. For local median filtering, the magnitude and orientation of the displacement vector is compared to that of the median vector of its eight nearest neighbours. If it falls within appropriate limits the vector is remains unmodified and if this filtering determines a spurious vector exists, the local median vector replaces the spurious vector. Careful attention is required during data collection and processing in order to ensure that the local median filtering is only applied to isolated bad vectors and not groups of bad vectors. This involved a manual, visual check of approximately 10% of the instantaneous, uncorrected vector fields to ensure sufficient vector field quality. Finally, a 2D gaussian function of size 5 is applied to improve noise reduction and to ensure a smooth continuous vector field. Figure 23a and Figure 23b shows a sample instantaneous vector field before and after correction for the jet-in-crossflow study.

To assess uncertainty inherent in the use of digital PIV (PIV which uses digital imagery rather than photographs), the work of Cowen and Monismith [58] was referenced. The uncertainty associated with PIV measurements and techniques was determined to be ±0.18m/s.
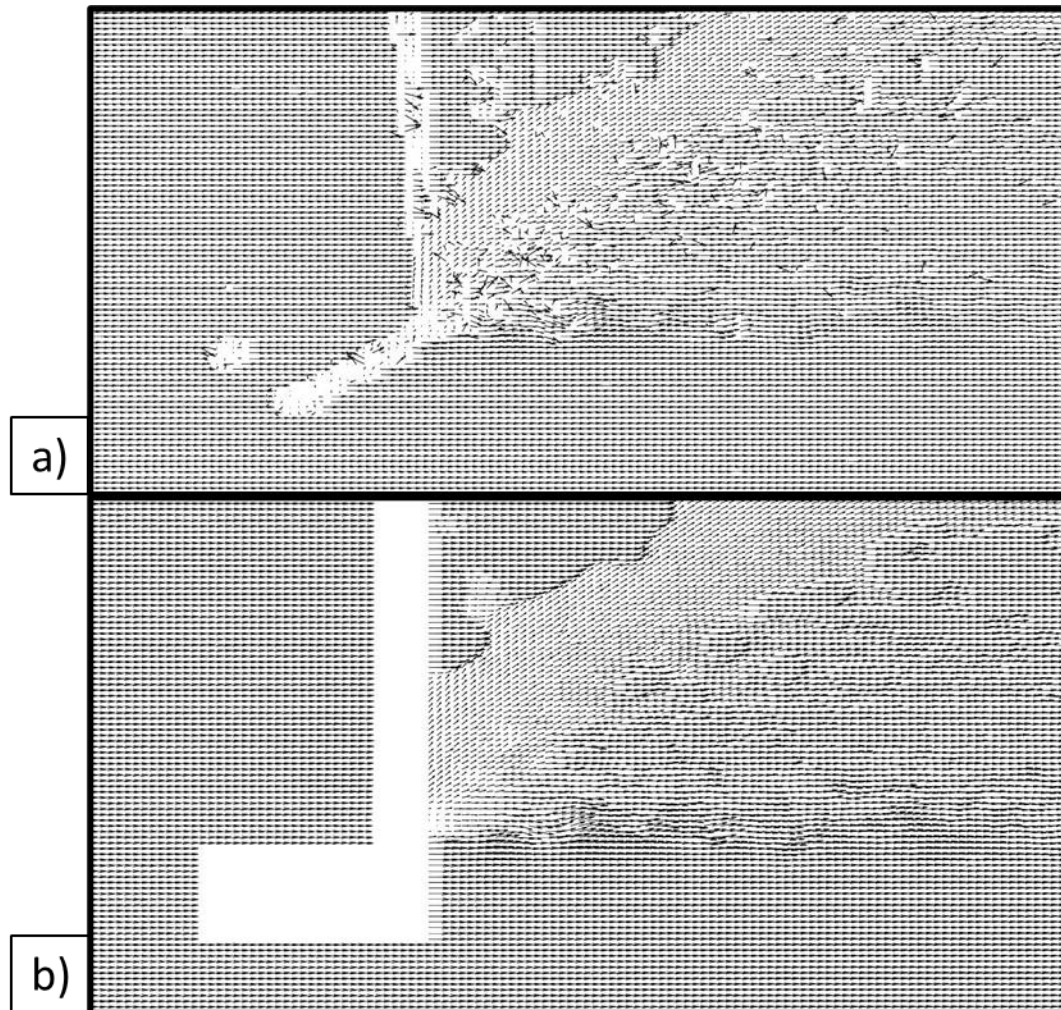
Figure 23: A sample instantaneous vector field of the jet-in-crossflow study (q=60)
(a) before correction and (b) after correction (with mask).

2.5.1.4   Computation of Various Flow Properties

The resulting instantaneous velocity vector fields can then be used to determine turbulent flow characteristics. Reynolds decomposition can be performed to obtain the mean and fluctuating components of velocity, as demonstrated by the x-component of velocity, *u,* in Equation (9). Using the instantaneous vector fields, the instantaneous velocity gradients $\frac{\partial \tilde{u}}{\partial x}, \frac{\partial \tilde{u}}{\partial y}, \frac{\partial \tilde{v}}{\partial x}, \frac{\partial \tilde{v}}{\partial y}$ were also determined.

Mean values were computed from a number of discrete samples in time, indicated by an overbar. The mean flow characteristics investigated were the streamwise and spanwise velocities, $\bar{u}$ and $\bar{v}$. The turbulent characteristics investigated were the root mean squared (RMS) streamwise and spanwise velocity fluctuations u'_{RMS} and v'_{RMS}, Equation (10), the turbulent kinetic energy K, Equation (11), the fluctuating component of vorticity ω', Equation (12) , and the Reynolds shear stress τ_{xy}, Equation (13). Note that to compute quantities of spanwise velocity, u in Equations (9) and (10) is replaced by v.

$$\tilde{u} = \bar{u} + u' \tag{9}$$

$$u'_{RMS} = \sqrt{\overline{u'(t)^2}} \tag{10}$$

$$K = \left[\frac{\overline{u'(t)^2 + 2v'(t)^2}}{2} \right] \tag{11}$$

$$\omega'_z = \frac{1}{2}\left(\frac{\partial u'}{\partial y} - \frac{\partial v'}{\partial x} \right) \tag{12}$$

$$\tau_{xy} = \overline{[u'(t) * v'(t)]} \tag{13}$$

The turbulent kinetic energy has been expressed only using on the x and y components of velocity, but this does not exclude the third, out-of-plane z component. In order to properly estimate K, the magnitude of the out-of-plane component also need to be estimated. Since the streamwise component of velocity is expected to be significantly larger in magnitude than either the spanwise or out-of-plane component, the out-of-plane component is assumed to be of comparable magnitude to the spanwise component. This assumption may be less accurate in regions of the flow which are near stalled conditions. Under this condition, a more appropriate assumption would be to assume all three velocity components carry roughly equivalent contributions. Regardless, for the current work the kinetic energy was calculated as shown in Equation (11) at all locations.

As mentioned previously, a mask is applied to the PIV field in areas where the field was obstructed. The regions appear in the PIV data as blank regions. Due to slightly different fields of view, this blank region is different between the low momentum flux cases (q of 10 and 20) and the higher momentum flux cases (q of 60 and 120). Figure 24a and Figure 24b highlights these regions for both scenarios, overlaid on a raw PIV image to hopefully give the reader a sense of the obstruction objects.
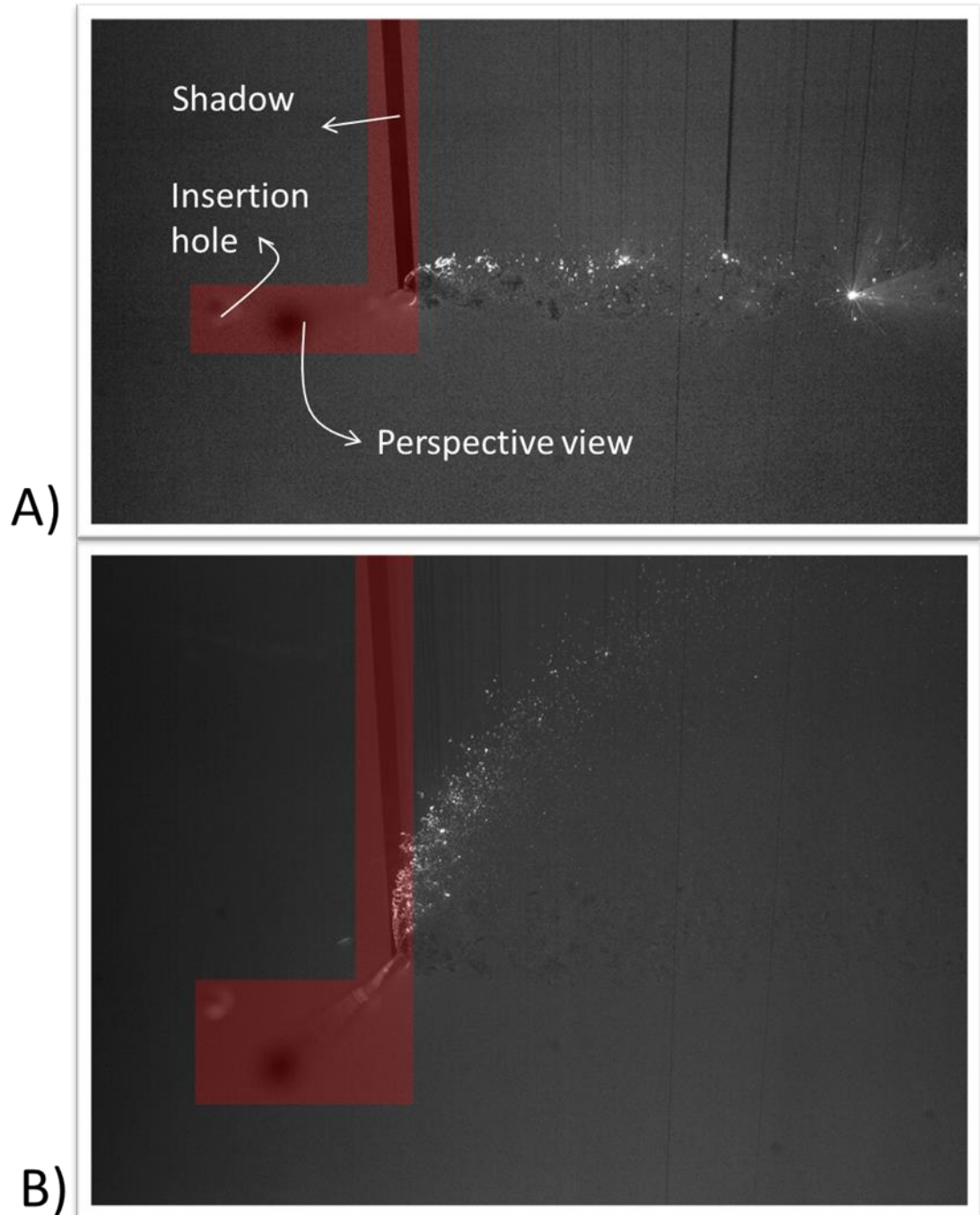
Figure 24: Raw PIV images for A) *q* = 10 and B) *q* = 60, **overlayed with a highlight indicating regions where spray bar obstructions exist and were masked out of the PIV data.**

A fluctuating vector field and some sample colour plots for a jet-in-crossflow test at a momentum flux of 60 are shown in Figure 25 and Figure 26. The plots show distinct features such as the turbulence, the spray shear layers bounding the spray as well as traces of the wake created by the spray bar.
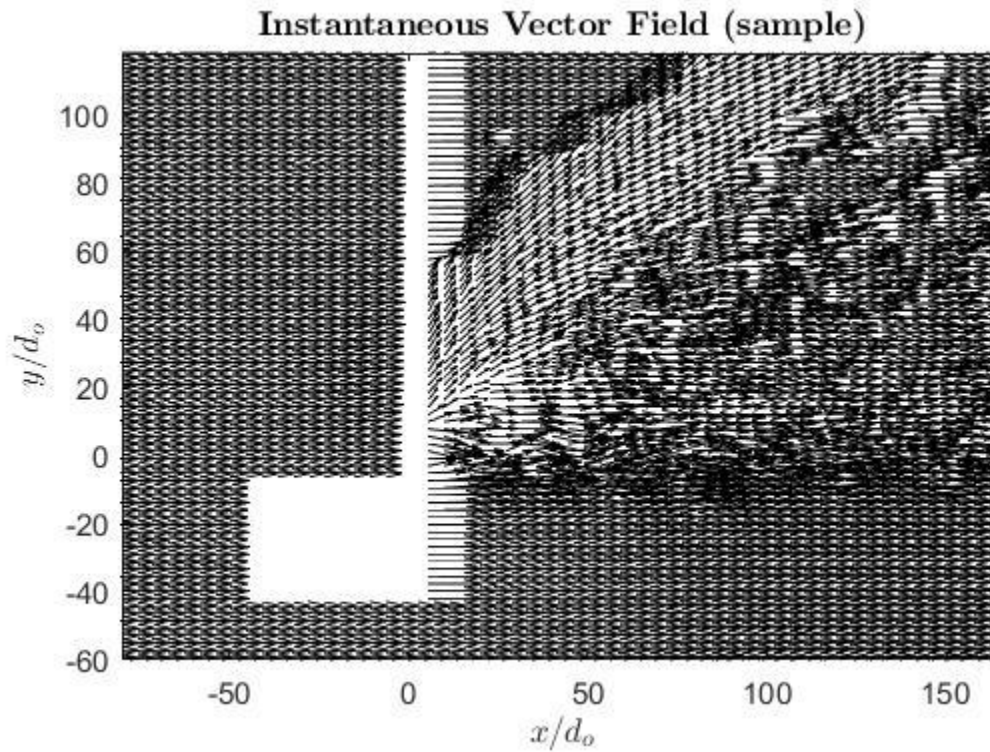
Figure 25: Randomly sample of the fluctuating vector field for $q = 60$.
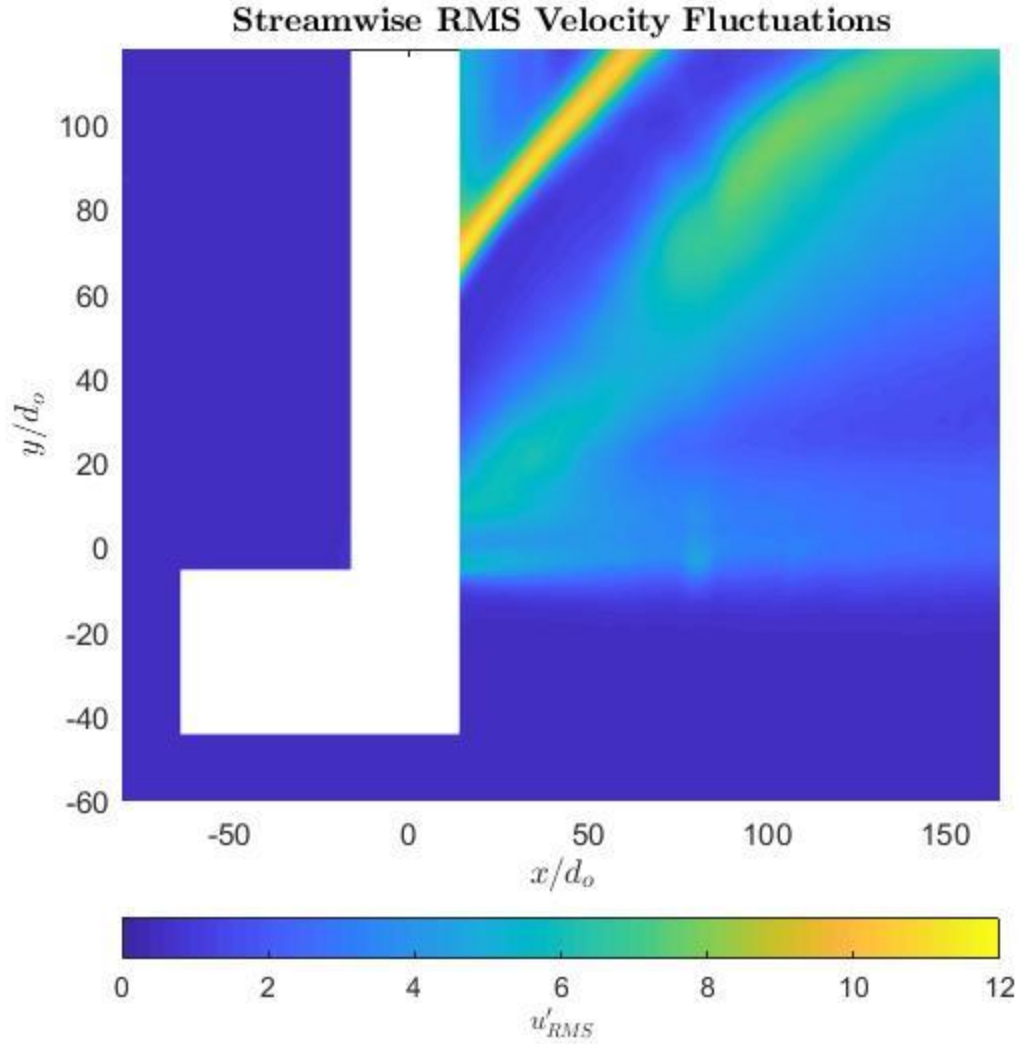
Figure 26: Color map of the RMS streamwise velocity fluctuations for a jet-in-crossflow at *q* of 60. The white region corresponds to the noisy regions that were masked out.

2.5.1.5   Background Flow Characterization

Before proceeding with any PIV experiments, the quality of flow through the new wind tunnel modifications was performed. The flow quality resulting from the new wind tunnel modifications was quantified using the turbulence results of a gas-only flow field (no spray). The background flow was characterized upstream of the spray bar with the spray bar present in the test section, serving as both a characterization of flow quality as well as an analysis of the freestream flow for the free spray study. First, the newly achievable wind

tunnel speeds were examined over the range of frequencies used to control the fan motor. The line of best fit is shown in Figure 27 and has a coefficient of determination of 0.998. Figure 28 shows a scatter plot of the mean streamwise velocity and the streamwise turbulent intensity upstream of the spray bar. The turbulence intensity is less than 1.5% as indicated by the solid horizontal line.
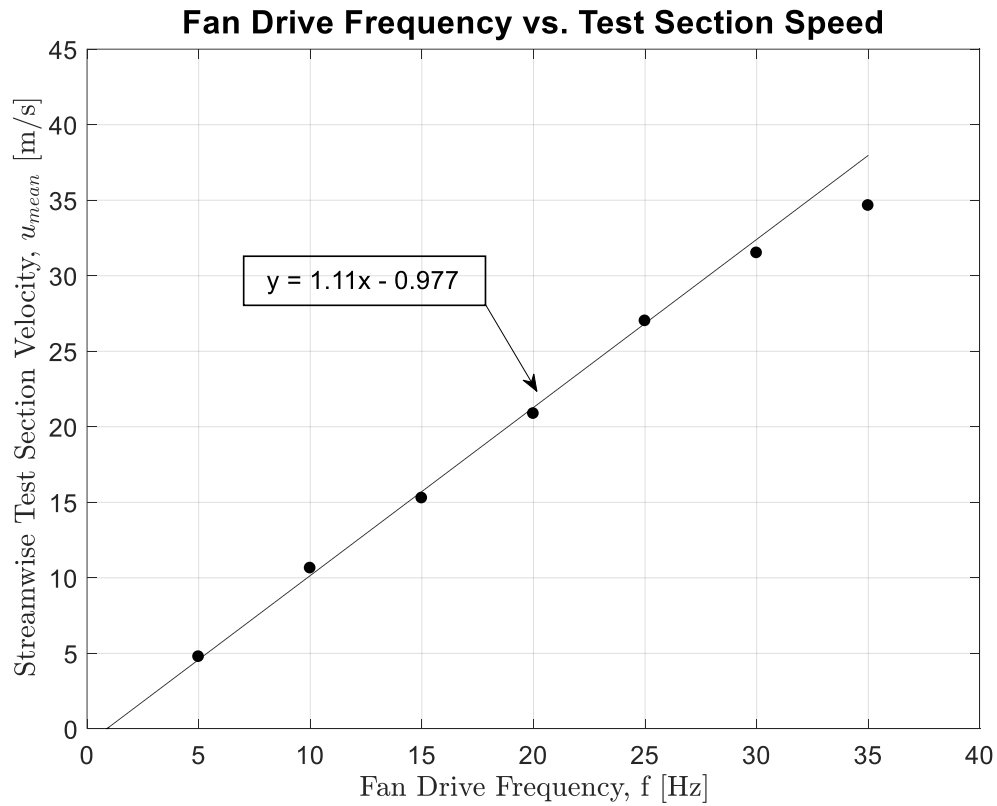
Figure 27: Wind tunnel streamwise velocity as a function of fan motor drive frequency
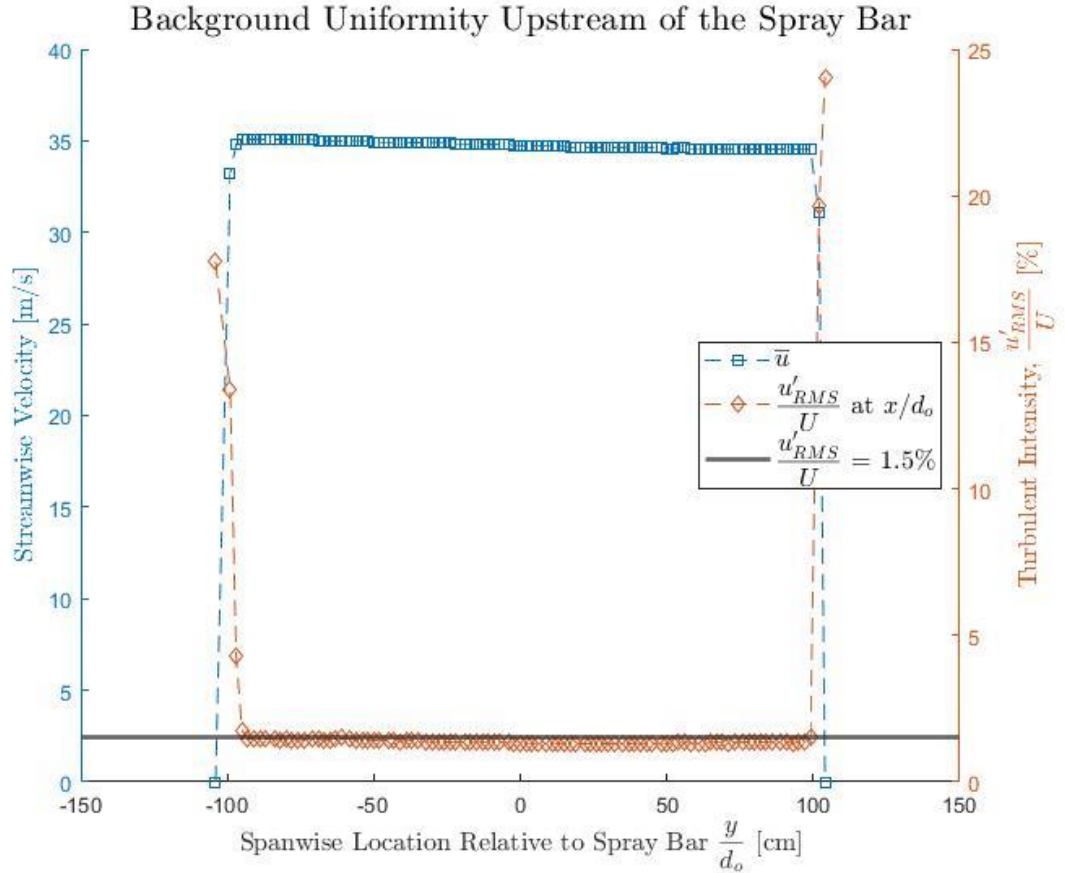
Figure 28: Mean streamwise velocity and turbulent intensity across the span of the test section, upstream of the spray bar.

In order to account for potential changes in bulk freestream velocity created by additional pressure losses in the wind tunnel system due to area blockage created by the bluff body, it was desired to perform another calibration with the spray bar and bluff body in place. However, the PIV equipment malfunction occurred before the bluff body tests were carried out. Regardless, an effort was made to collect PIV data for calibration. A very small group of approximately 10×20 poor quality vectors was obtained so the calibration was not continued. Calibration with a pitot tube should be performed before any further work, followed by PIV calibration once the equipment issues have been resolved.

2.5.2   Morphologic Droplet Characterization

Droplet characterization was performed on only one of the two images in each PIV image pair, in order to eliminate duplication of the data therefore, the number of PIV images processed for droplet detection is equivalent to the number of vector fields obtained. For the high-speed images, it was necessary to select images with a large enough Δt that consecutive images can be considered independent in the analysis. That is, it should be ensured that any single droplet is not measured more than once within a given measurement region. For global (whole image) measures such as probability distribution of droplet diameter, every 30th frame was sampled resulting in a total of 100 samples. For local measures, which in this study was a grid of bins 32×32 pixels in size, every 5th image was sampled, resulting in 600 total samples.

The liquid present in the imaging plane (i.e., laser sheet) was identifiable due to pixel saturation, as illustrated by the histogram in Figure 29. The majority of the image area consist of the seeded flow which is represented by gray values of approximately 70 or less, while there is essentially no signal between gray values of 70 and 254. However, there is a small peak at the maximum gray value intensity of 255, indicative of saturated pixels from the light scattering of larger accumulations of liquid such as the liquid jet, ligaments, and droplets as well as some image artefacts which will be removed.
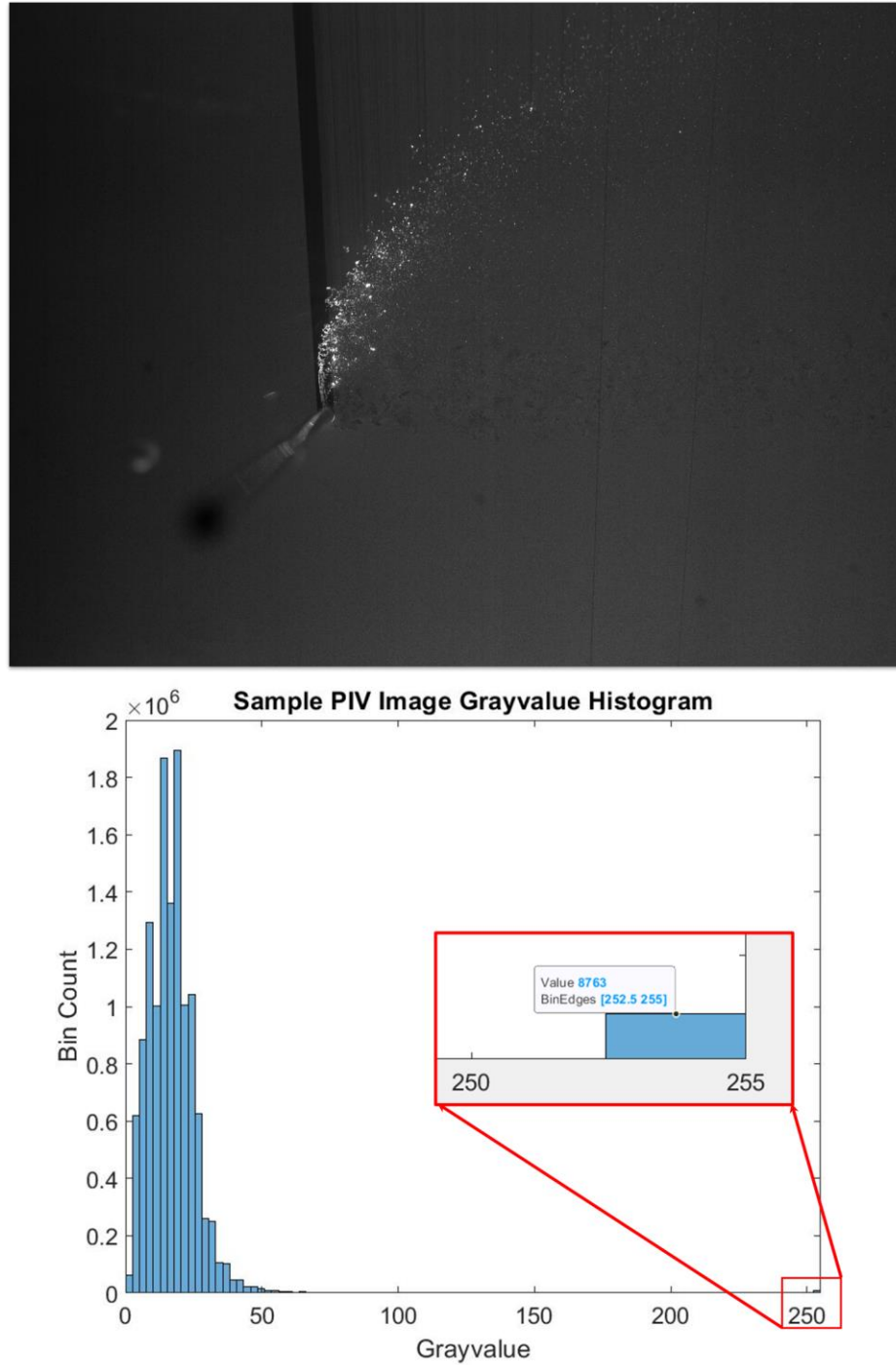
Figure 29: Raw PIV image (top) and image histogram (bottom) for a jet-in-crossflow spray at q of 60. The majority of the PIV information (seed particle) is found at gray values below 70, but a small peak occurs at 255, indicating the presence of liquid.

2.5.2.1   Image Preprocessing

The images were cropped to the area of interest in order to reduce size and capture as little extraneous information as possible. The image was converted to a binary image using a threshold conservatively determined to be 30% of 255. The preprocessing of objects in the HSI image did not have background "noise" from the seed particles, so only noise from the image sensor needed to be removed. Sensor noise created gray values of a maximum of approximately 5 but droplets remained saturated at or near 255, and so the binary image threshold was set to a gray value of 10. The remaining steps were identical for PIV and HSI generated binary images.

Using the binary image, the basic properties of any 8-bit connected objects could be computed. These object properties used include equivalent diameter, area (total pixel count), centroids, bounding boxes, and extent. The equivalent diameter and the extent of an object are defined in Equations (14) and (15). The equivalent diameter is the measure used to quantify droplet diameter.

$$Extent = \frac{Area}{Area\ of\ Bounding\ Box} \qquad (14)$$

$$Equivalent\ Diameter = \frac{4 * Area}{\pi} \qquad (15)$$

Morphologic dilation was performed on the binary image to connect objects such as the spray column and ligaments, and to connect any objects detected that may be quite close to each other (e.g., a droplet located very near a ligament). These objects were filtered based on object area.

2.5.2.2   Droplet Detection

Droplet detection was performed by identifying all 8-bit connected objects in the filtered binary images. Any object with an extent less than $^2/_3$ was excluded from the analysis. In addition, since the laser sheet was approximately 1mm, any droplets found to be greater than 1mm in diameter was removed from the analysis. This corresponds to an equivalent diameter larger than 18.5 pixels for the PIV images and 6.2 pixels for the high-speed

images. Figure 30 identifies some objects often found in the binary images which are removed using the above processes.
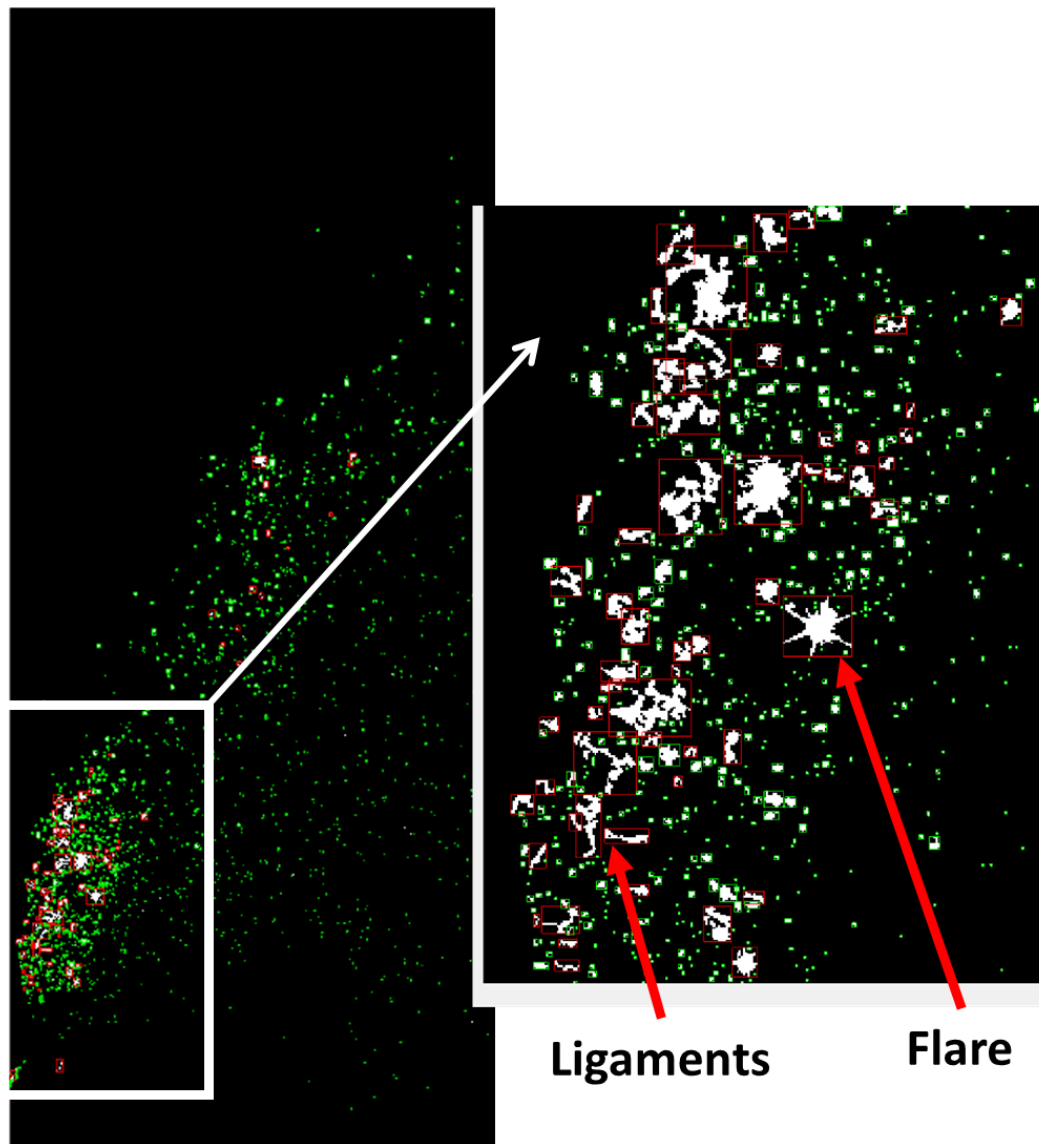
Figure 30: Droplet identification visualized using green and red bounding boxes to identify droplets and non-droplets respectively. Left: Binary image of the near spray region with large droplets, ligaments, and flares. Right: Identification of liquid packets from column breakup as well as flares from large water drops.

Ultimately, the near-spray region identified in Figure 30 above is a highly dense spray region, primarily filled with ligaments, large drops, and other undesired objects therefore

the dilation process described removes almost the entirety of this region. Figure 31 shows an original PIV image with the spray and the corresponding segmented image of the spray.

<div align="center">Original PIV Image   Segmented image</div>
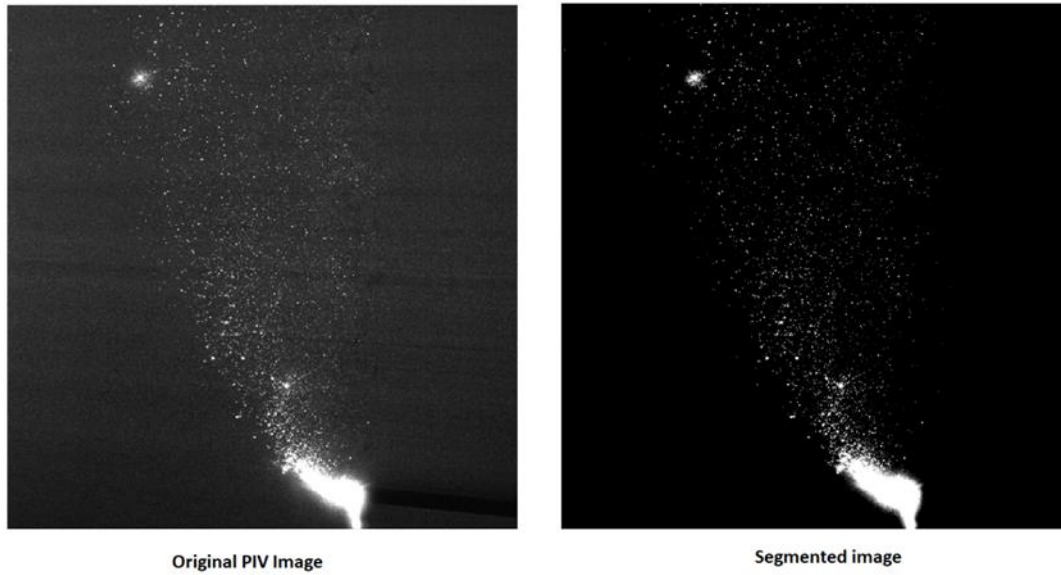
Figure 31: Original PIV image with the spray and the corresponding segmented image showing the spray only.

To examine the spatial distribution of droplet size, the image was divided into 32×32 pixels bins which overlap directly with the vector field from the PIV data, and the Sauter mean diameter (Equation (16)) was calculated for each bin. The function $f(D)$ represents the frequency, or number of droplets found for a given diameter D, similar to a probability density function.

$$D_{32} = \frac{\int_{D_{min}}^{D_{max}} D^3 * f(D)}{\int_{D_{min}}^{D_{max}} D^2 * f(D)} \tag{16}$$

Unfortunately, a major limitation of the droplet detection algorithm exists. The minimum droplet size is dependent on the field of view required for PIV vector characterization, as this directly impacts image resolution. For the free spray studies, the 185px/cm results in a minimum droplet size of approximately 61µm which is not much larger than the minimum expected of 30µm. However, for the bluff body study the 62 px/cm results in a minimum visible droplet size of 182µm. The resolution is also quite poor particularly at lower droplet

sizes. Droplets of the size of a one-pixel diameter can also be difficult to reliably identify and is susceptible to Type II error (false positives).

2.5.2.3   Droplet Velocity Analysis (High speed imaging data)

Object properties relevant to streak detection are called the Feret properties. Essentially, these properties measure the maximum and minimum antipodal distance of an object. Assuming the droplet travels in approximately a straight line during the exposure time of 50μs, it was assumed that the minimum antipodal distance of a streak object was comparable to the diameter of the droplet from which it was created. Then, the maximum antipodal distance was considered to be the linear direction of travel. Therefore, the displacement of the droplet was determined as,

$$|d| = (max.\,antipodal\,distance) - (min.\,antipodal\,distance)$$

The velocity was calculated as,

$$|v| = \frac{|d|}{\Delta t_{exposure}}$$

This velocity magnitude was the only metric examined for the streak images. Unfortunately, as the streak method was developed very last minute it lacks functionality and testing.

2.6   Summary

This thesis research is comprised of two major experiments studies examining the dynamics of liquid droplets in a stream of high-speed gas flow. The test section of the existing wind tunnel was modified primarily with the objective to increase the speed in the test section in order to achieve better similarity to afterburner flows, but also to facilitate the removal of the injected liquid from the wind tunnel. Unfortunately, some design issues did not lead to a sufficient increase in wind tunnel speeds (closer the afterburner conditions) however, it was also later discovered that current PIV equipment was not capable of measuring flow at such speeds. Regardless, achieving the desired speeds could have changed the focus from a PIV analysis to a HSI analysis.

The first part of the thesis study was to examine the spray behaviour of a jet-in-crossflow and a jet-in-counterflow which were created using simple orifice spray bar injection. This study utilized PIV to characterize the flow turbulence of the gas crossflow. The PIV laser illuminated the spray droplets in addition to the seeded flow making the droplets detectable. These droplets were detected and analysed using in-house MATLAB software, and turbulent flow quantities and droplet size distributions were investigated.

The second part of the thesis study involved diverting the jet-in-crossflow spray around a vee-gutter bluff body. Due to PIV equipment issues, high-speed imaging was used to record the behaviour of the spray droplets without information of the gas flow field around the bluff body. Droplet behaviour was identified qualitatively over 0.375s of recording, and droplet sizes and velocity magnitudes were examined quantitatively. Droplet sizes were analysed using the same algorithm as for the PIV work, while droplet velocities were determined using streak images. The streak images are slightly longer in exposure time allowing the droplet to create a small streak revealing its motion.

Both PIV and HSI studies were conducted at a range of momentum flux ratios, varied by varying the liquid mass flow rate at a constant freestream crossflow speed. The HSI study was limited in scope and rigour due to time constraints imposed by the malfunctioning PIV equipment as well as the COVID-19 pandemic.

Chapter 3

3   Jet-in-Crossflow and Jet-in-Counterflow Characterization

The PIV images acquired during the experiments contained information about the gas velocity field as well as the spray behaviour. The analysis of these images allowed for simultaneous collection of information about the spray characteristics, particularly the droplet sizes, and the associated gas flow behaviour. This investigation is unique in identifying local interaction between a liquid jet-in-crossflow (JIX) and jet-in-counterflow (JIC) spray and the gas crossflow. Such investigations have not been reported in the previous literature and it is vital for a better understanding of the spatio-temporal coupling between the gas flow and the liquid spray.

The jet breakup regime of interest in the thermoacoustic environment of an afterburning duct is dominated by shear breakup resulting from aerodynamic forces. Due to limited capabilities of the PIV system, the investigation was performed at a fixed gas crossflow velocity of 35m/s corresponding to a We_g of 16 which is outside of the desired shear breakup region. At this We_g, jet breakup is expected to demonstrate bag breakup behaviour [30]. The values of momentum flux ratios, q, examined are 10, 20, 60, and 120, which correspond to Re_j of 3000, 4300, 7500, and 10,600 respectively. Based on these Re_j, breakup of the jet-in-crossflow was expected to be primarily due to aerodynamic forces of the crossflow for the low values of q (10 and 20), and primarily due to turbulence within the liquid jet at the larger values of q (60 and 120).

In the following sections, confirmation of the expected jet-in-crossflow spray regime is described, followed by the characteristics of the spray droplets and by presentation of the mean and turbulent gas flow characteristics. The resulting local interaction between the spray and crossflow turbulence are then described.

3.1   Jet-in-Crossflow

Qualitative review of the PIV images confirms that jet breakup falls within the bag breakup regime expected for the We_g of 16 in this work [30]. Figure 32 shows the jet as

viewed within a PIV image for all q investigated, and evidence of bag breakup can be seen in all images, but most strongly at low values of q due to the aerodynamic (non-turbulent) nature of the jet breakup. The transition from aerodynamic to non-aerodynamic jet breakup is evidenced in these images; for Figure 32a and Figure 32b the jet column remains unbroken under bending until bag breakup causes column breakup, whereas Figure 32c and Figure 32d illustrate that the jet column appears to split and break without external influence of the gas crossflow (that is, without bending of the column). Bag breakup, a characteristic of aerodynamic dominated breakup, is present at low and high values of q, and since the increase in droplet shedding near the jet column for the high q flow suggests increased shearing of the droplets from the jet column, the regime examined is likely some mix between aerodynamic jet breakup and non-aerodynamic breakup. In fact, the Re_j of 7,500 and 10,600 for these cases is in line with the expected transition region characterized by Madabhushi et al. [39] and Sallam et al. [38] found between Re_j of 6,000 and 60,000.
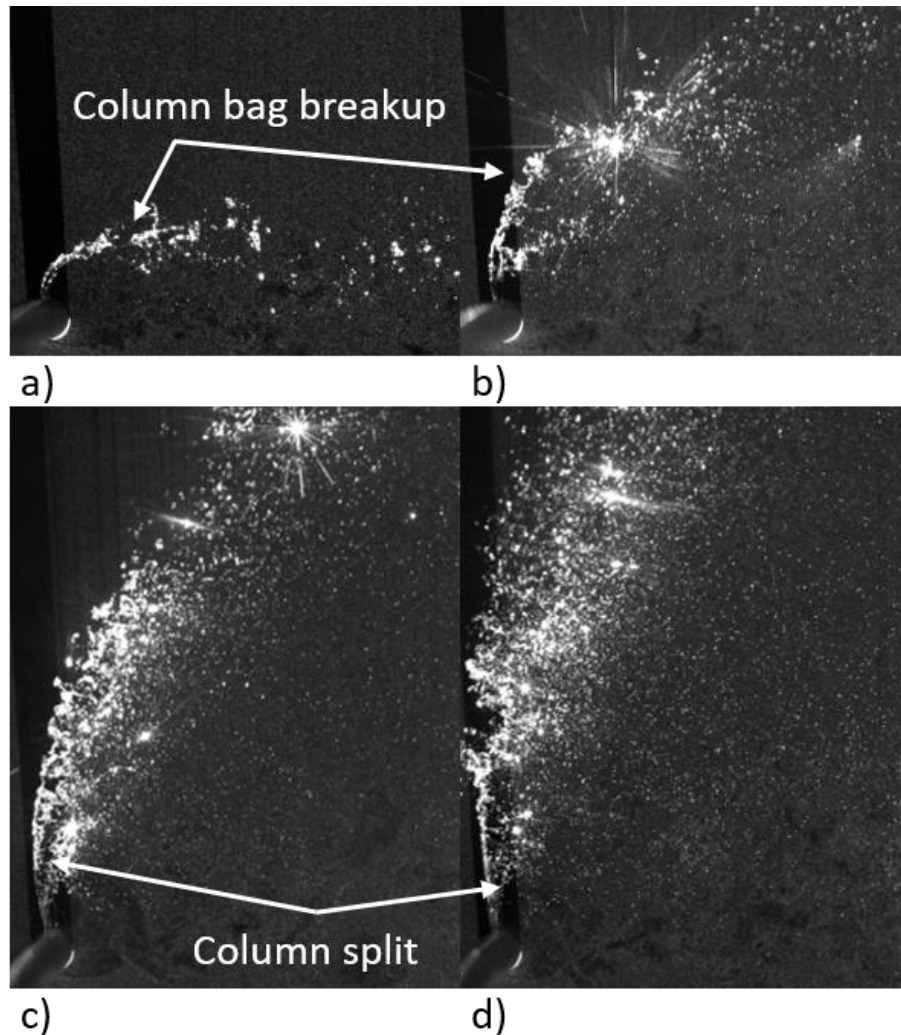
Figure 32: Raw PIV images of jet-in-crossflow for momentum flux ratios of a) 10, b) 20, c) 60, d) 120. Evidence of bag breakup can be found in all cases and the column breakup processes differs for a) & b) (aerodynamic breakup) and for c) & d) (liquid turbulence).

3.1.1   Spray Characteristics

The global and local distribution of droplet sizes was characterized using the droplet detection methods describe in the previous chapter. Figure 33 shows the probability distribution of the equivalent droplet diameter. It can be seen that the majority of droplets for all momentum flux ratios (q of 10, 20, 60, 120) were of the smallest discrete droplet size (~61µm) since 87.6%, 86.7%, 77.7%, and 73.7% of droplets were of this size for a

momentum flux of 10, 20, 60, and 120 respectively. At a momentum flux of 60 and 120, there was a slightly larger proportion of 86μm droplets, the second smallest size, than for the 10 and 20 cases. This may have been a result of decreased aerodynamic breakup at high q due to the liquid momentum being a more dominant inertial force. These two smallest droplet sizes accounted for approximately 96% of total droplets for q of 10, 20 and 60, and 87% for q of 120. Although no direct (near identical We_g and q) comparison could be made to published droplet distributions, the size distribution found in this experiment seems to agree with known trends, which indicate that the droplet size distribution is contained within a narrow size range of ±20μm at near atmospheric freestream pressure, with the range increasing at higher ambient pressure [59]. Although the majority of droplets contained in that study were of approximately 20μm, the lower We_g and freestream velocity would be expected to produce a larger overall droplet size [32].
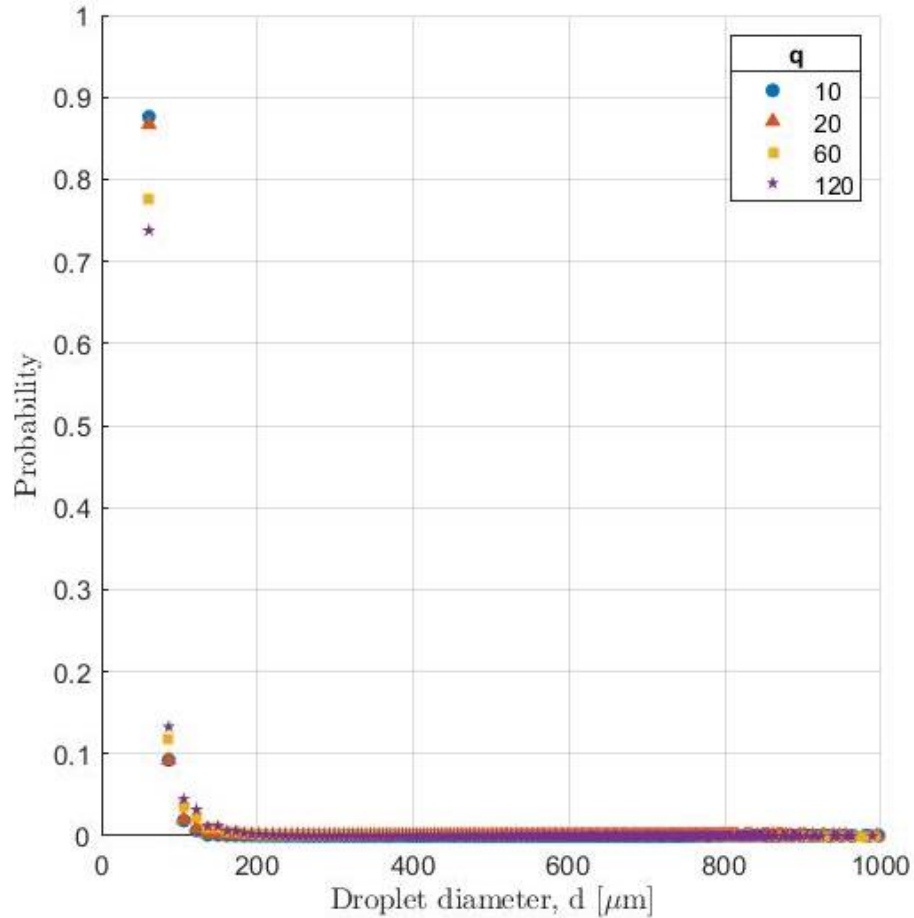
Figure 33: Probability distribution of droplet diameters over the entire 2D field of view of the spray

In addition, [46] found that within 50 x/d_o downstream of the injector all droplets were less than 75µm in diameter agreeing with the current work. Outside of the bag breakup regime and into the shear breakup regime, Lubarsky et al., Song et al. (2013), and Song et al. (2015) all found that measures of droplet size for JIX were below 100µm[47], [54], [55].

In order to characterise any effects of the spray bar wake, measurements of droplet size distribution were investigated within the wake region, which was defined by the boundaries of $y \approx \pm 10d_o$ from the axial centerline of the spray bar. One of two behaviours was expected to be found due to spray bar turbulence. Either the increased momentum transfer due to wake turbulence could promote droplet breakup or, the gas velocity in the wake region would promote droplet relaxation due to decreased relative motion between the droplets

and the gas phase. Figure 34 shows a distribution similar to the overall spray field measurements; the two smallest diameters contained 92% (q of 120) to 95% (q of 20) of the total droplets within the wake. The variation between different momentum flux ratios is markedly lower in the wake region, with a noticeable difference only for 61µm diameter droplets. This is likely not an effect of momentum transfer producing smaller droplets therefore not supporting the initial speculation, but rather a consequence of larger droplets penetrating the gas crossflow leaving an overall smaller population size of droplets in the wake region.

Johnson et al. [46] were the only ones to previously examine JIX from a spray bar injection orifice, rather than from a wall mounted injection orifice, however they did not compare differences between droplets measured in the bulk spray field against spray droplets in the wake created by the spray bar.
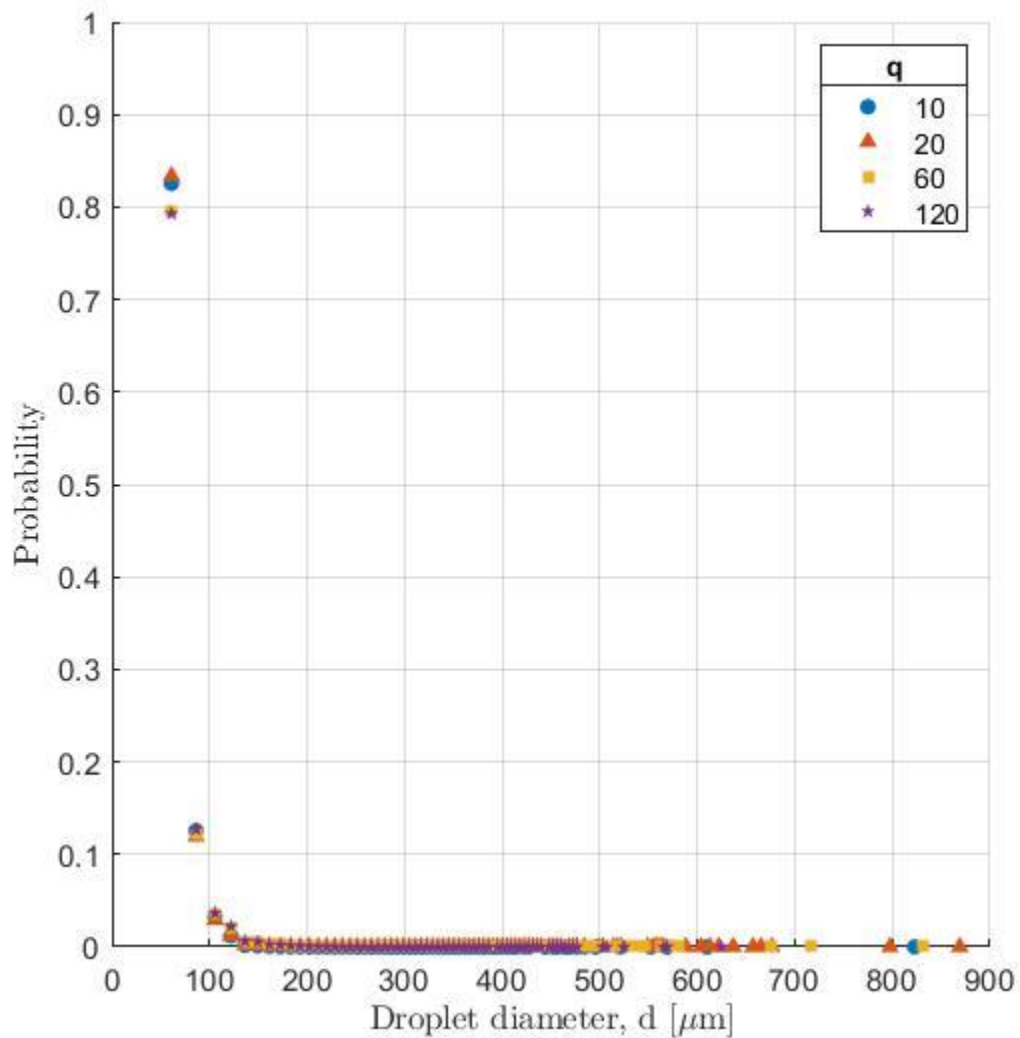
Figure 34: Probability distribution of droplet diameters in the spray bar wake region (in the range of $y \approx \pm 10 d_o$ from the spray bar).

It was expected that an increased proportion of smaller droplets would be present at higher momentum flux ratios due to enhanced atomization processes. This is conceptually supported by the literature which has demonstrated that droplet size is primarily determined by We_g and also, to some extent, by Re_j which has the effect of enhancing primary jet breakup via jet turbulence in the non-aerodynamic breakup regime ($Re_j > 5{,}000$). It is also qualitatively supported by the images shown in Figure 32 however, the droplet distribution measurements shown in Figure 33 presents opposing evidence.

While investigating this finding, the total droplet counts for q of 10, 20, 60, and 120 were determined to be 47.6x10^6, 52.4x10^6, 39.7 x10^6, and 47.8 x10^6, which shows that a nearly equivalent (all on the order of 10^6) total number of droplets was detected globally across all cases.

This discrepancy could plausibly be due to an operation in the image processing algorithm which serves to eliminate large objects to reduce the detection of flaring, ligaments, and large drops (diameter > 1mm). This technique may also have resulted in the removal of groups of large droplets (diameter < 1mm individually, but in close proximity and larger than 1mm collectively) for low q flows whose sprays were not as disperse as the high q flows, thereby reducing large droplet count and thus affecting overall distributions. It is also possible that the probability distributions for q of 60 and 120 is lacking in small droplet counts because the entirety of the spray atomization is not contained within the measurement field of view due to increased jet penetration. Sharma [60] has shown that a larger quantity of droplets is found somewhere between the upper and lower bounds of the spray cloud in the y-direction in the far-field region ($\frac{x}{d_o} > 50$), however no studies have provided data on sprays whose penetration is similar in extent to the higher q cases examined in the current work making it difficult to draw conclusion.

Although the measurement technique may need refinement and further validation in order to accurately determine droplet counts (therefore distributions), the sizes of droplets detected in this work match what has been found in the literature. Ultimately, increasing the field of view to capture the entirety of the spray field at high q is an experimental challenge for the technique used to quantify droplet size as an increase in field of view will reduce image resolution and therefore further increasing the value of the measurable, discrete droplet sizes.

Figure 35 shows the spatial distribution of the calculated Sauter mean diameter, SMD (D_{32}) using a color map for different momentum flux ratio cases. The blank white spaces indicate the bins (32x32 pixel areas) where no droplets are detected and a SMD could not be determined. This generally coincides with a portion of the shadow cast by the PIV laser sheet over the spray bar.
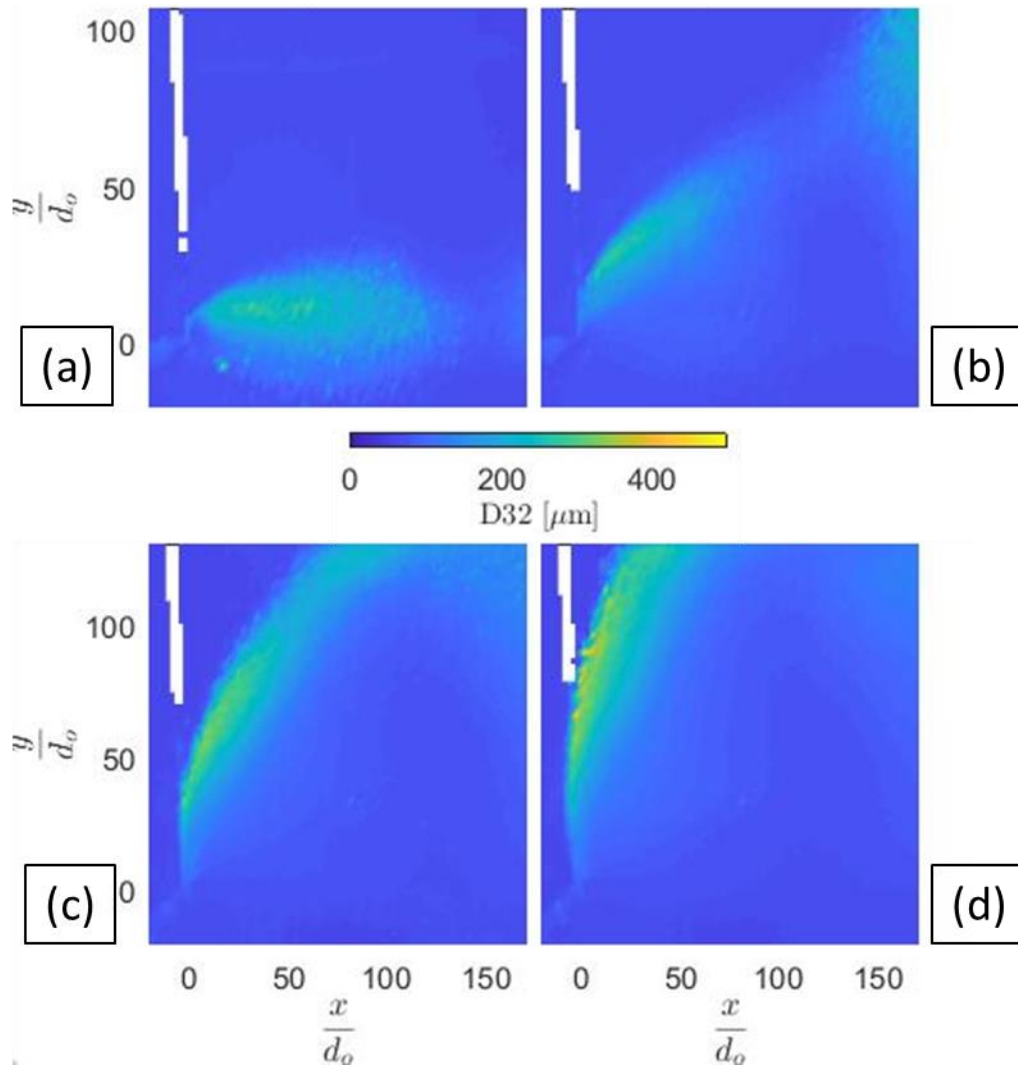
Figure 35: Color map illustrating the distribution of Sauter mean diameter for momentum flux ratios of (a) *q*= 10, (b) *q*= 20, (c) *q*= 60, (d) *q*= 120.

The spray fields found at lower momentum flux ratios of 10 and 20 in Figure 35a and Figure 35b are well contained within the field of view and the spray plume shape is clearly illustrated for all cases. Figure 35c and Figure 35d show that at *q* of 60 and 120, the SMD is larger than for low *q* flow, particularly on the windward side of the spray plume within the jet column.

Of note in Figure 35b, there is an increase in droplet size near the edge of the field of view. The presence of these droplets was confirmed in the raw PIV images and does not appear to be an image artifact. However, it may be that this is a result of non-uniform brightness

across the width of the image, particularly near the edges, resulting in higher contrast between droplets and the background seeded flow. It is suspected that the light intensity illuminating the droplets plays a role in the detected size, and increased contrast between droplet and background may play a similar role. However, these factors were not investigated during this study.

The detailed spatial distribution of droplet sizes was determined by looking at spanwise SMD distributions at fixed downstream locations of $\frac{x}{d_o} = 20, 50, 100$, and 150. Figure 16 shows the spanwise SMD distribution for different momentum flux ratio cases at these downstream locations.

At q of 10, the plot (Figure 36a) shows that the droplets within the spray plume are generally large, which may seem to be in direct contrast to the histogram in Figure 33 and Figure 34. However, the magnitude of the SMD is strongly affected by the presence of large droplets and as such, a large SMD indicates that there exists a significant quantity of larger droplets locally. The droplet sizes decrease rapidly between $100d_o$ and $150d_o$ downstream of the spray bar which is a may be an indication of droplet breakup. No studies were found investigating droplet size this far downstream of the injector. As expected at this low liquid flow rate, the lack of jet penetration results in a location of peak droplet sizes which does not change.
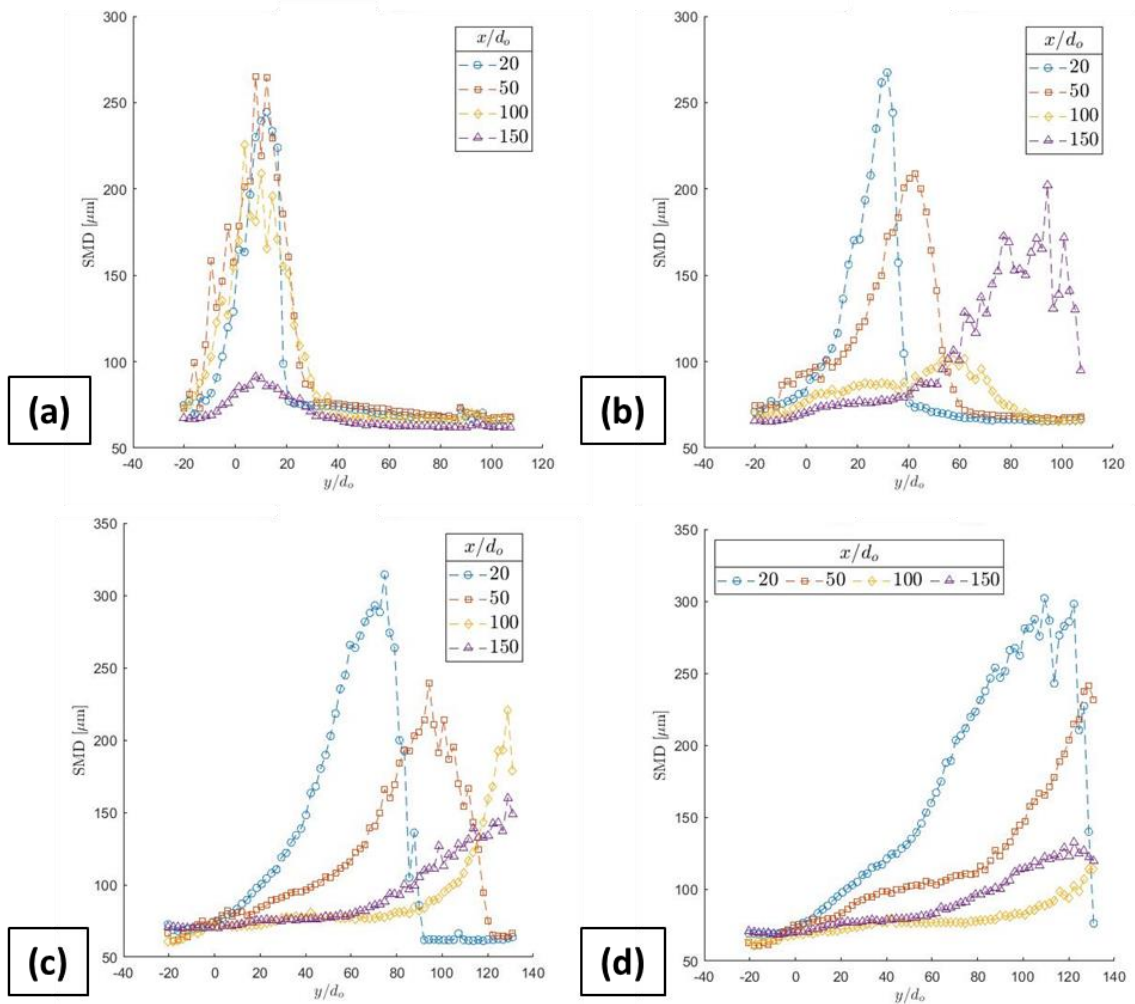
Figure 36: Spanwise distribution of Sauter mean diameter at various downstream locations for (a) *q*= 10, (b) *q*= 20, (c) *q*= 60, (d) *q*= 120.

For the other cases where *q* is 20, 60 and 120, the peak SMD was overall found to decrease with downstream distance from the spray bar, and the location of maximum SMD (i.e., the location of larger droplets) also moved further in the cross-stream direction (see Figure 36b, Figure 36c, Figure 36d). This indicates progressive levels of droplet atomization as the jet trajectory is followed downstream. Although literature does report a decrease in SMD with downstream measurement [44], [46], there is no consensus on the rate at which SMD decreases (i.e., the rate *a* in the general function of SMD ~ -*a*(x/d$_o$)*). In addition, it appears that the maximum SMD is approximately 40µm larger for high (*q* > 60) momentum flux ratios compared to low (*q* of 20). This is illustrated in Figure 37, which shows the

SMD distribution at 20d$_o$ downstream of the spray bar at all momentum flux ratios. The figure shows an increase in the crossflow spread of large droplets.
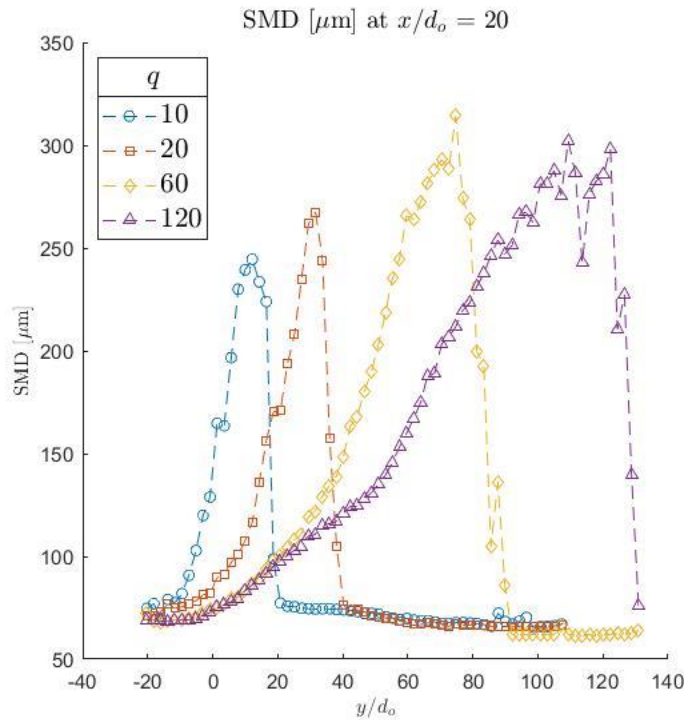
Figure 37: Spanwise distribution of Sauter mean diameter 20d$_o$ downstream from the spray bar for *q* of 10, 20, 60, 120.

3.1.2   Mean Flow

In order to further investigate the JIX spray and droplet behaviour, the velocity fields were characterized at all momentum flux ratios. A sample mean vector field at *q* of 20 can be seen in Figure 38. The mean freestream velocity immediately upstream of the spray bar was approximately 35 m/s. The colour maps of the mean streamwise velocity fields at different momentum flux ratios are shown in Figure 39. As plots show, the free-stream velocity upstream of the spray bar and far away from the spray is uniform while the velocity magnitudes in the spray and spray bar wake regions are reduced. Changes in the momentum flux ratio resulted in varying spray trajectories however, only flow near the jet column and adjacent spray field showed reduced mean flow velocities. At higher momentum flux ratios, as the liquid spray penetrated deeper in the cross-stream direction,

wake behaviour downstream of the spray region is evident. The proximity of the contour lines to each other at the upstream edge of the spray region in Figure 39 show the presence of strong velocity gradients in the mean flow at all q. The spatial variation in mean flow velocity magnitude indicates some form of momentum transfer, which will be further examined through turbulence quantities.
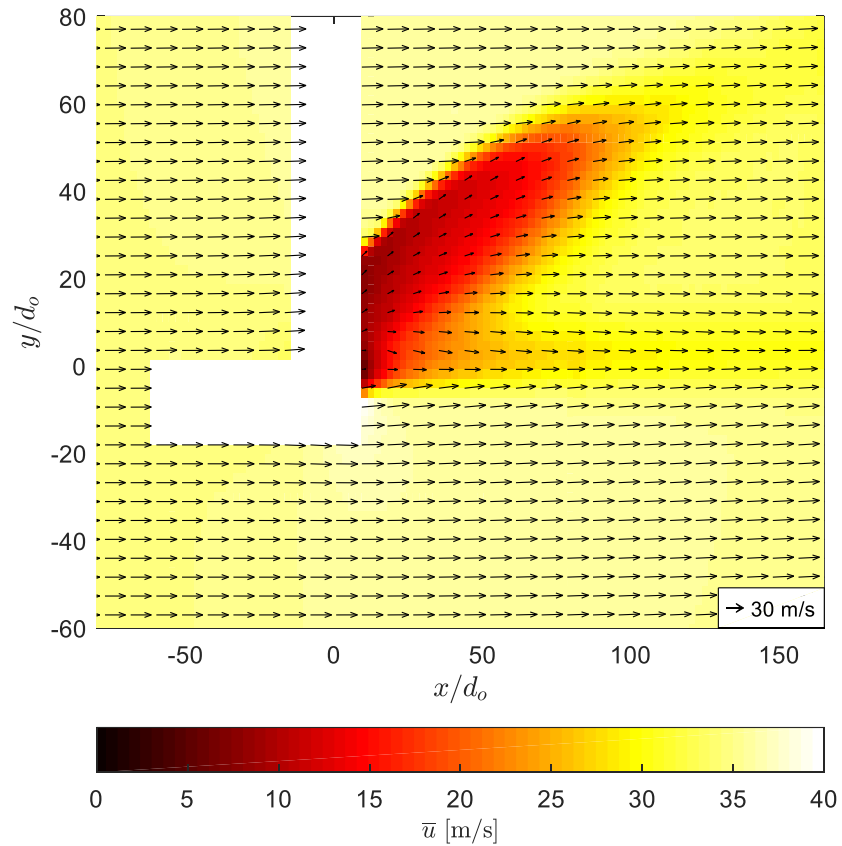
Figure 38: Mean vector field superimposed on a colour map for mean streamwise velocity $\overline{u}$ for a momentum flux ratio of 20
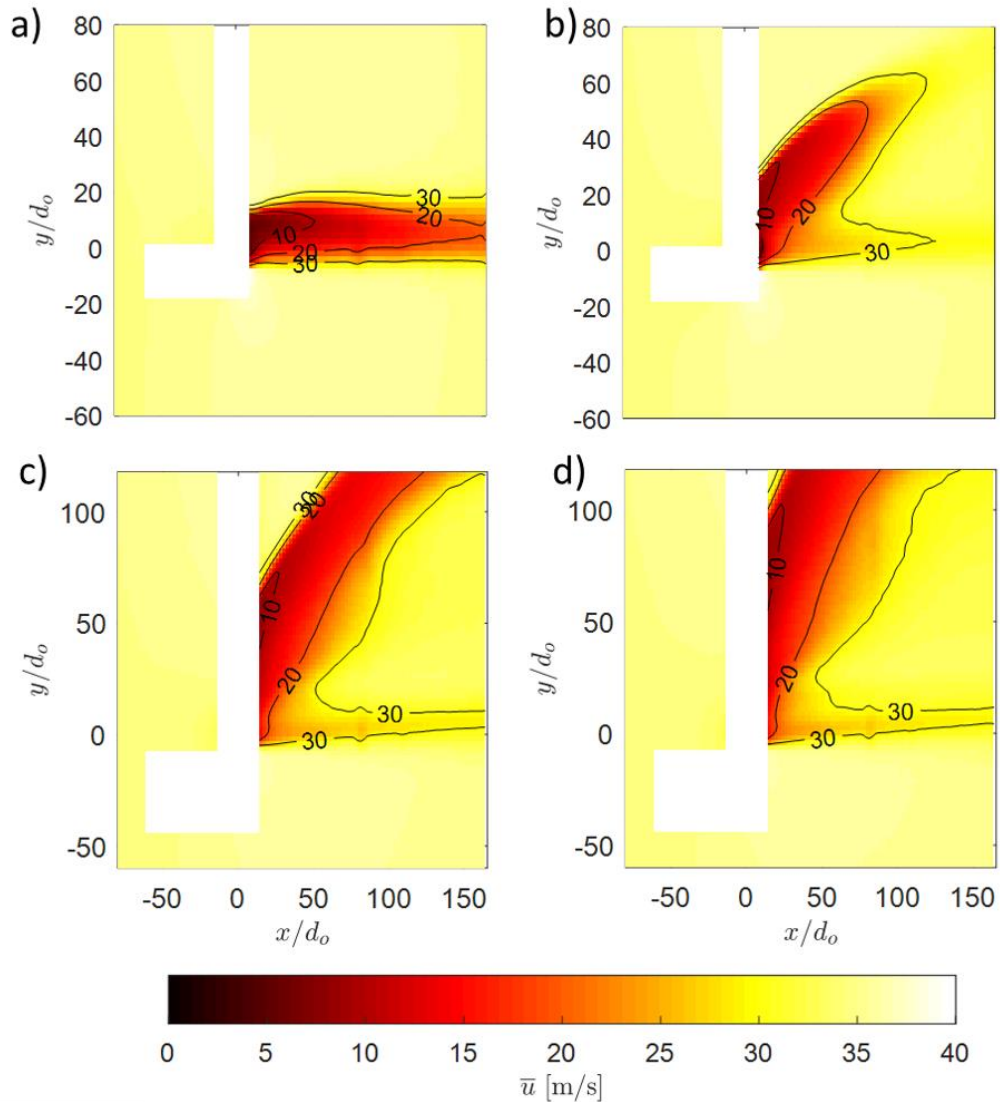
Figure 39: Colour maps with contour lines of the mean streamwise velocity for q = 10 (a), 20 (b), 60 (c), and 120 (d).

The difference between the local mean velocity and the free stream velocity was calculated. Figure 40 presents the areas of the flow which are faster than the freestream velocity of 35m/s. There is an increase in velocity around the spray plume and spray bar wake, which is expected in order to satisfy the conservation of mass principle. As the gas flow velocities are reduced within the spray region, the flow external to this region must accelerate to conserve mass. At q of 10, the velocity increases by up to approximately 1.2 m/s (3.5% of the freestream velocity) in most locations with a peak increase of up to 5.3 m/s (15% of the

freestream) directly adjacent to the spray bar on the side opposite of the injection orifice. The same acceleration behaviour can be seen for all momentum flux ratios examined. The acceleration of the flow in the vicinity of the spray has not been well-reported in the literature. Few numerical studies have reported slight acceleration in the gas flow near to the jet column, however, they did not quantify the acceleration magnitude [35], [61], [62].
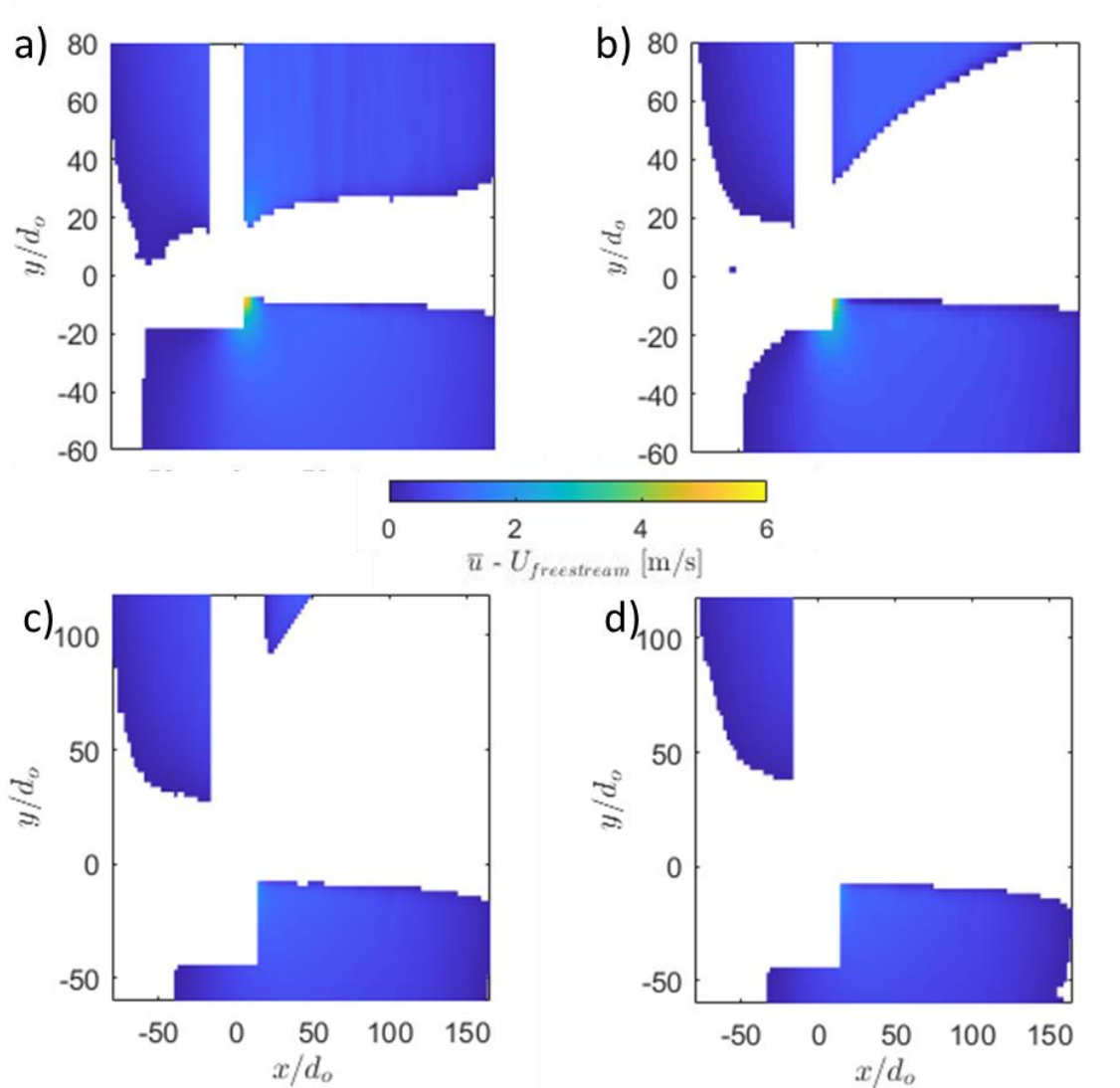
Figure 40: Colour maps of the velocity difference between the freestream and local mean velocities for $q = 10$ (a), 20 (b), 60 (c), and 120 (d). N.B. These maps only show regions with speeds above the freestream velocity (>35m/s).

3.1.3　Turbulence

In order to investigate the influence of turbulence local to the JIX spray on jet breakup processes, characterization of the turbulent kinetic energy (TKE), *K* and Reynolds shear stress, $\overline{u'v'}$ was performed. The Reynolds shear stress was studied in order to investigate momentum transfer from the mean flow of the gas and liquid phases into the turbulent field, and to investigate the influence of the momentum transfer on droplet and spray characteristics.

The overall spatial structure of the flow turbulence is depicted via color maps of the turbulent kinetic energy (TKE) for all momentum flux cases, in Figure 41. The plots show distinct regions of high TKE values.
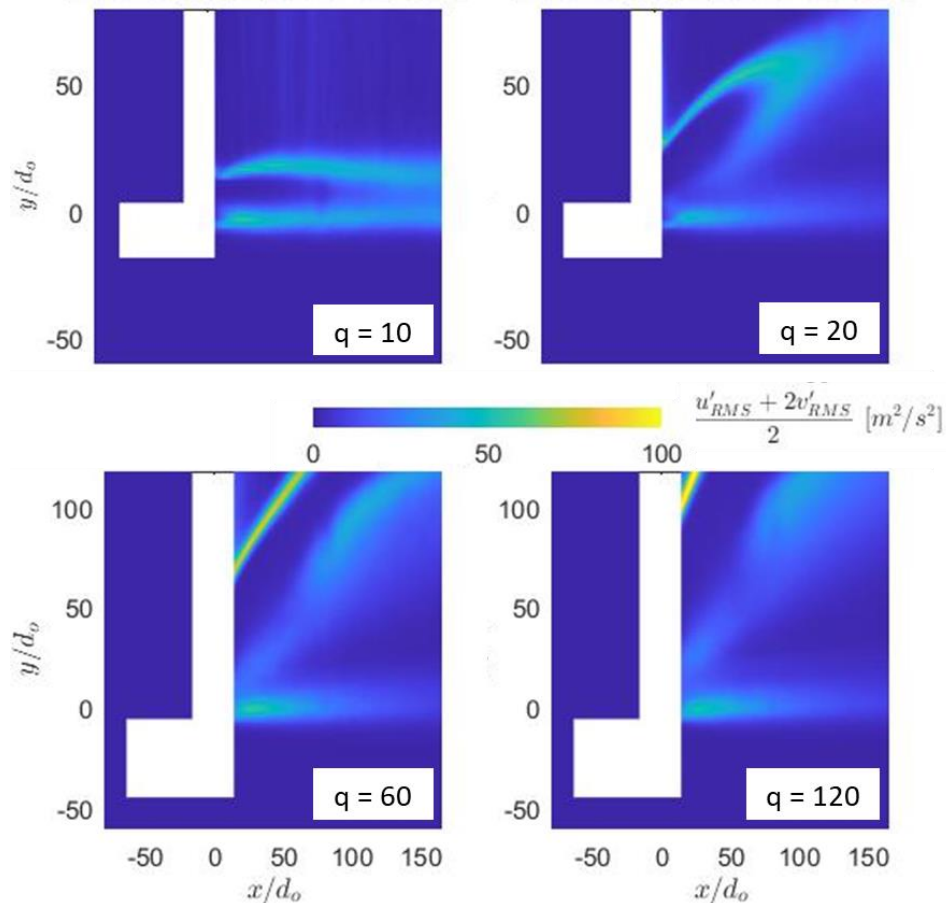
Figure 41: Turbulent kinetic energy illustrating the turbulence occurring in the windward side of the spray plume, as well as in the wake.

The spray region is shown to be bounded on the windward side of the droplet plume by a strong turbulent velocity signature present where a shear layer exists between the droplet plume and the incoming gas. For any given momentum flux ratio case, the highest magnitudes of TKE are observed in the shear layer. The results show that the magnitude of TKE in the shear layer increased with an increase in the momentum flux ratio.

Weak TKE signatures are also observed in the wake regions (i.e., the wake due to the spray bar and the wake formed by the spray droplets. The weaker turbulent signature slightly downstream of the windward boundary illustrates turbulence create in the wake of the spray plume, and this signature indicates the presence of the leeward boundary of the droplet plume. Here, a boundary is defined as a change in turbulence relative to the organized flow of the droplet/spray plume. In addition to outlining the droplet plume, a turbulent signature is also present in the spray bar wake horizontally and downstream of the spray bar but offset laterally from the spray bar at approximately $\frac{y}{d_o} = \pm 10$. For lower jet penetration (q of 10) the leeward plume boundary mixes with the spray bar wake whereas better jet penetration leads to distinct regions of spray wake and spray bar wake). The spatial extent of the enhanced turbulence in both wake regions expanded with an increase in the momentum flux ratio.

In the upper portion of Figure 41 for q of 10, outside the active spray region, streaks can be seen which are absent in the other cases. The streaks are a result of shadows created by larger droplets and are an indication that the presence of shadows was significant enough to create spurious turbulent signatures over an otherwise smooth background. Since the droplet plumes for the other cases extend out of the field of view quite rapidly, it is presumed this signature would also persist in those cases. But enhanced atomization from cross-stream mixing reduces droplet sizes and reduced droplet sizes may lessen this effect.

The Reynolds shear stress magnitudes are shown in Figure 42 for different momentum flux ratio cases. The results show similar spatial signatures as observed for the TKE. That is, the Reynolds shear stress magnitudes are highest in the shear layer of the spray plume and are also significant in the wake regions of the spray and spray bar. The results also show

that the spatial extent of the Reynolds shear stress increased with an increase in the momentum flux ratio.

In order to characterize, the changes in turbulence downstream of the spray, the spanwise profiles of the Reynolds stress, $\overline{u'v'}$ are extracted at various downstream locations, $\frac{x}{d_o} = 20, 50, 100$, and 150 (see Figure 43). Figure 44 illustrates the profiles of $\overline{u'v'}$ in the spanwise direction at the above-mentioned measurement locations for q of 20. With the exception of q of 10 due to its lack of crossflow penetration, all momentum flux ratios showed very similar turbulence distribution in the spanwise direction. So, q of 20 was used as it was fully visible within the field of view.
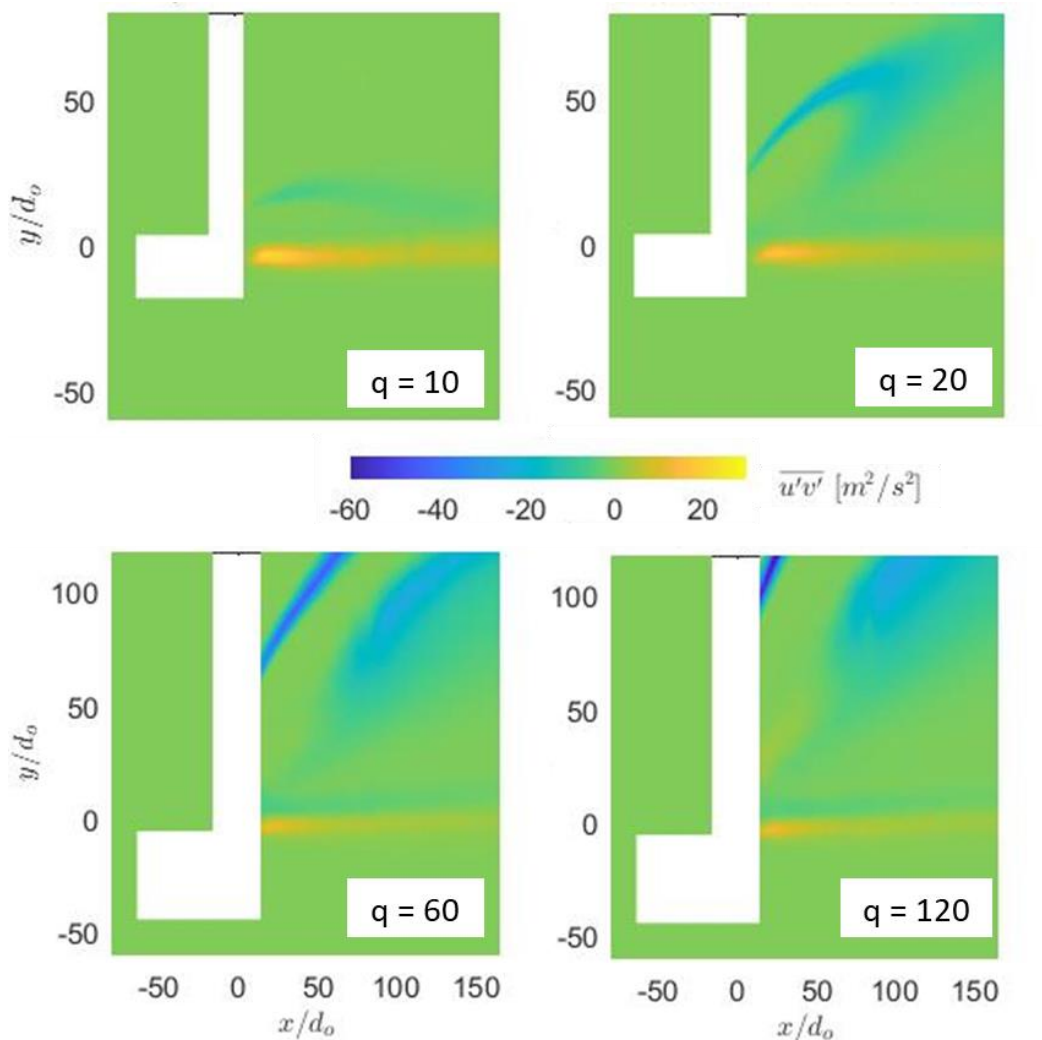
Figure 42: Colourmap of the Reynolds shear stress $\overline{u'v'}$
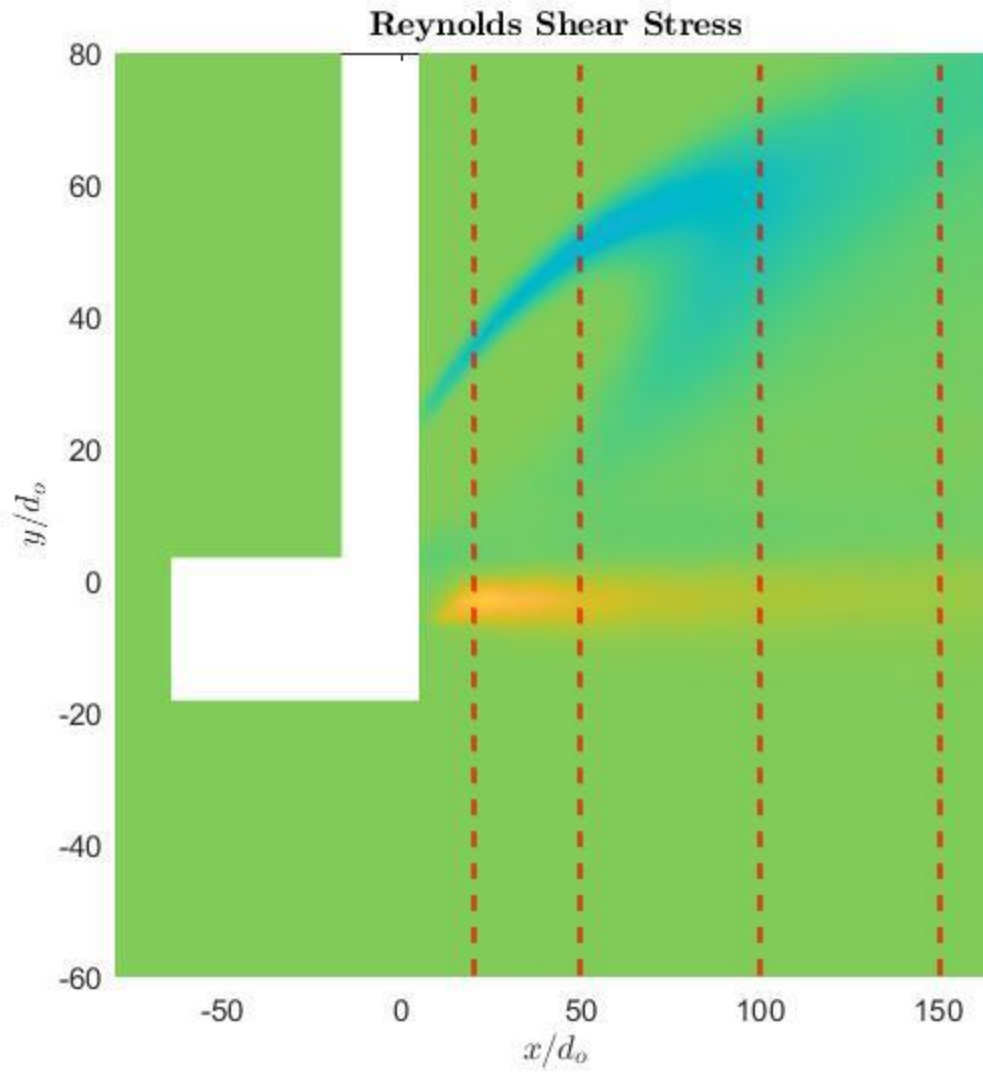
Figure 43: Colormap of Reynolds shear stress at q = 20. Downstream markers (red dashed lines) indicate the examined locations.
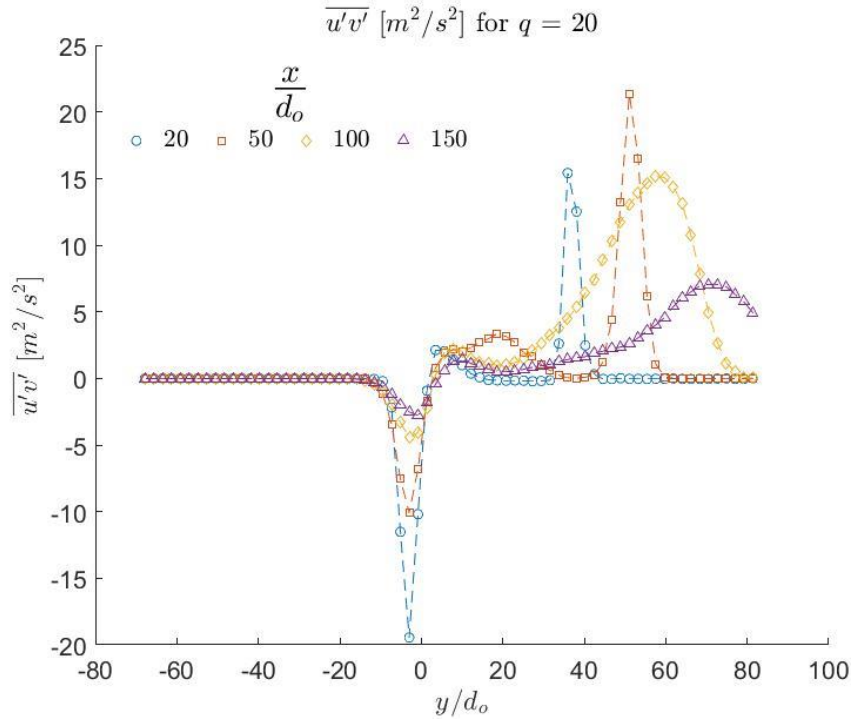
Figure 44: Crossflow distribution of Reynolds shear stress at various locations downstream from the spray bar (q = 20).

The signature from the spray bar wake is present around $\frac{y}{d_o} = 0$ and is stronger on the freestream side of the spray bar where the velocity gradients are large. The windward boundary of the spray plume can be identified in Figure 44 by the large peak moving further away from the spray bar (increasing $\frac{y}{d_o}$) with each downstream measurement. The magnitude of the Reynolds stress in the shear layer is shown to decrease with an increase in the downstream distance, likely due to droplet relaxation, which is the response of a particle to its surrounding flow (faster response time means a droplet is more relaxed). As the difference in droplet and gas velocity decreases (both in magnitude and direction) bulk droplet velocity approaches the gas velocity in both magnitude and direction, the interference of gas flow caused by the droplets decreases, resulting in smaller gradients between the two fluids. Although the stress peak reduces in magnitude, it does not disappear altogether. This is suspected to be an indication that the momentum, which is being transferred from the mean flow to the droplets, is no longer being used for droplet breakup, but rather to accelerate the droplets. A number of studies have shown that droplet

acceleration does occur downstream of the jet column wake, supporting the current findings [42], [61], [63].

Figure 45 compares the spanwise Reynolds shear stress profiles at $\frac{x}{d_o} = 100$ for all momentum flux ratio cases.
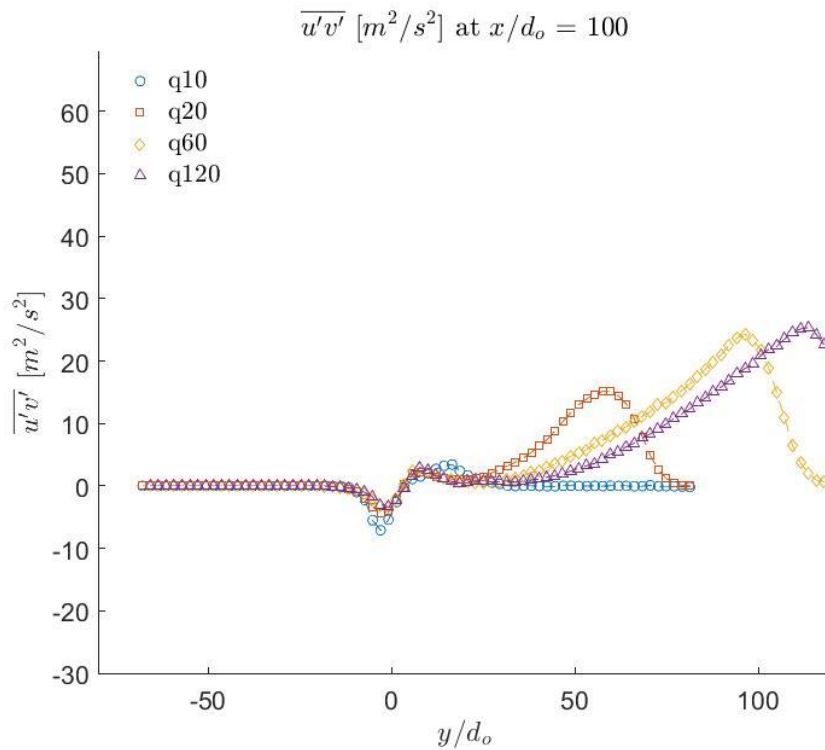
Figure 45: Reynolds shear stress $\overline{u'v'}$ for q = 10, 20, 60, and 120 at a downstream distance of 100d_o from the spray bar.

The plot shows that at this fixed downstream location, the lateral extent of the Reynolds shear stress increases with an increase in the momentum flux ratio. This is likely due to the extension of the wake region created by the spray plume. Jets-in-crossflow have been shown to create a recirculation zone similar to that of a bluff body [64]. As the spray plume increases in size (corresponding to increased q and jet penetration), this recirculation region may increase, therefore extending turbulence in the plume wake increasingly downstream in response to a larger recirculation zone. It can be speculated that this may produce one of two opposing behaviours.

First, the lower velocity and extended length (relative to the streamwise width of the spray plume) of this region may contribute to increased capacity for droplet relaxation as the droplets are progressively introduced to larger and larger gradients (low gradients and low speed in the wake, higher speed and higher gradients outside of the recirculation region). This would result in less atomization as a result of reduced magnitudes of the local gradients and increased droplet acceleration. On the other hand, an increase in volume/mass fraction of liquid in this region due to the progressive jet/droplet breakup process may encourage the formation of turbulence, particularly in JIX application using substantial liquid volumes or higher liquid densities. In contrast, larger spray droplets travelling on the windward side of the spray plume have a limited capacity for relaxation without sufficient reduction in size which in turn would slow the droplet relaxation process. Based on existing correlations for spray trajectories [29], there is no indication that the windward spray boundary, intrinsically bound to the motion of the larger droplets, ever achieves a fully relaxed state.

To further understand the flow energy distribution within the turbulent features, specifically through their interaction with spray droplets, proper orthogonal decomposition (POD) analysis was conducted. In the POD technique, a given quantity is decomposed into several POD modes, which are eigenfunctions. A coefficient is associated with each of these modes, which is a function of the calculated eigenvalues. In the present study, the snapshot proper orthogonal decomposition (POD) method was used [65]. It is important to note that these POD modes do not represent actual scales of turbulent flow, but previous studies have shown that the pattern of the flow energy associated with POD modes closely resemble that of turbulent structures. Figure 46 shows the fractional energy distribution in POD modes.
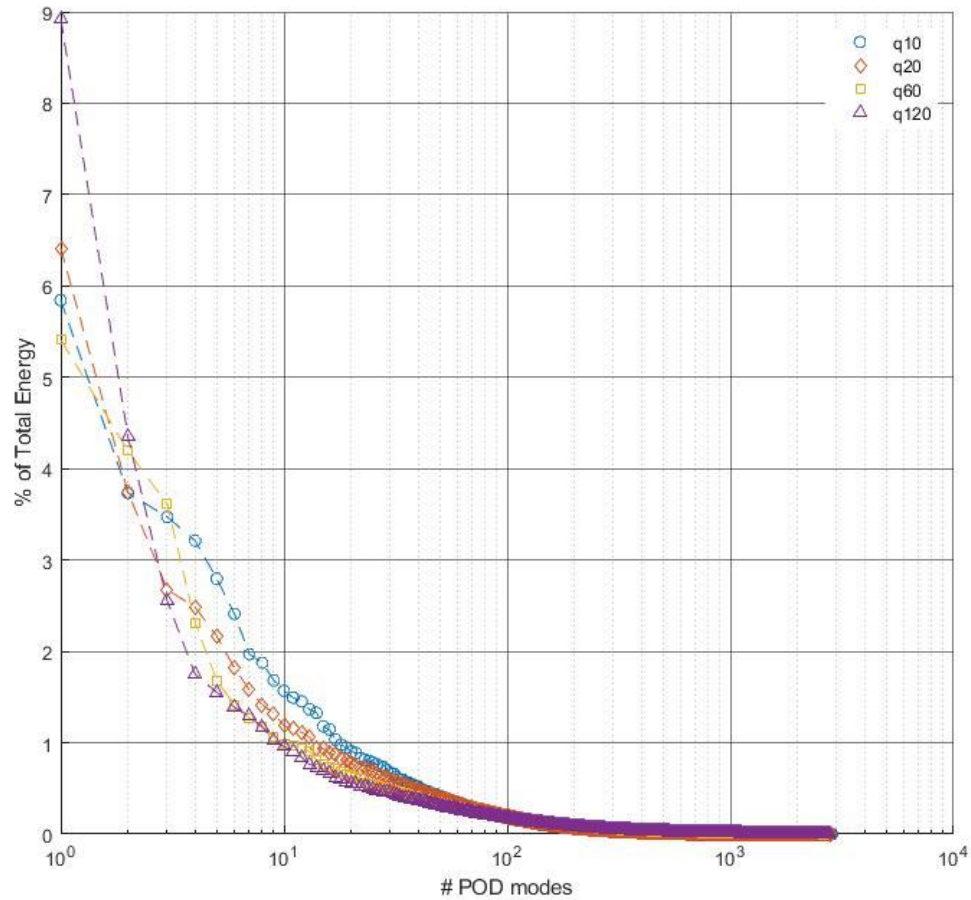
Figure 46: Energy fraction contained within each individual POD mode

The lower POD modes contain the largest fraction of the total flow energy and resemble the larger turbulent structures. The results show that in lower modes, the energy distribution varies with the momentum flux ratio. The fractional energy in the first mode is largest at the highest momentum flux ratio. In the mode range from about 5 to 40, the fractional energy distribution becomes largest at the lowest momentum flux ratio. Finally, as the POD modes continue to increase, the distribution of energy decreases with decreasing momentum flux ratio. This indicates that the flow energy is relatively more accumulated in lower modes (approx. modes 1 to 100) at the lowest momentum flux ratio. A suggested reason for the difference between momentum flux ratios is that in the given measurement region, and at the lowest momentum flux ratio, the flow field associated with the spray is

fully resolved, while at the highest momentum flux ratio it was partially resolved (i.e., the flow was not contained entirely within the field of view). Thus, it is likely that the turbulent flow scales associated with the spray in this modal range are not fully captured as the momentum flux ratio increased, and that the missing energy contributions lie in the toe of the horseshoe-like feature seen in the turbulence color maps.

This trend is further evident in Figure 47, which shows the cumulative distribution of energy with increasing POD modes at different momentum flux ratios. As the momentum flux increases (and as has been shown the magnitudes of turbulence) the energy is increasingly distributed amongst the higher POD modes, which could be related to smaller turbulent scales. For example, at the momentum flux ratio of 10, 50% of the flow energy was contained in about 30 modes, whereas at the momentum flux ratio of 120, 50% of the flow energy was distributed in 70 modes. Similarly, the 90% of the flow energy was distributed in about 350 and 1000 modes at the momentum flux ratios of 10 and 120, respectively. These results indicate that as the influence of turbulence increases with an increase in the momentum flux ratio, the energy distribution extends to the higher modes. This may be interpreted as saying that the mid-range turbulent structures become more energetic with an increase in the momentum flux ratio.
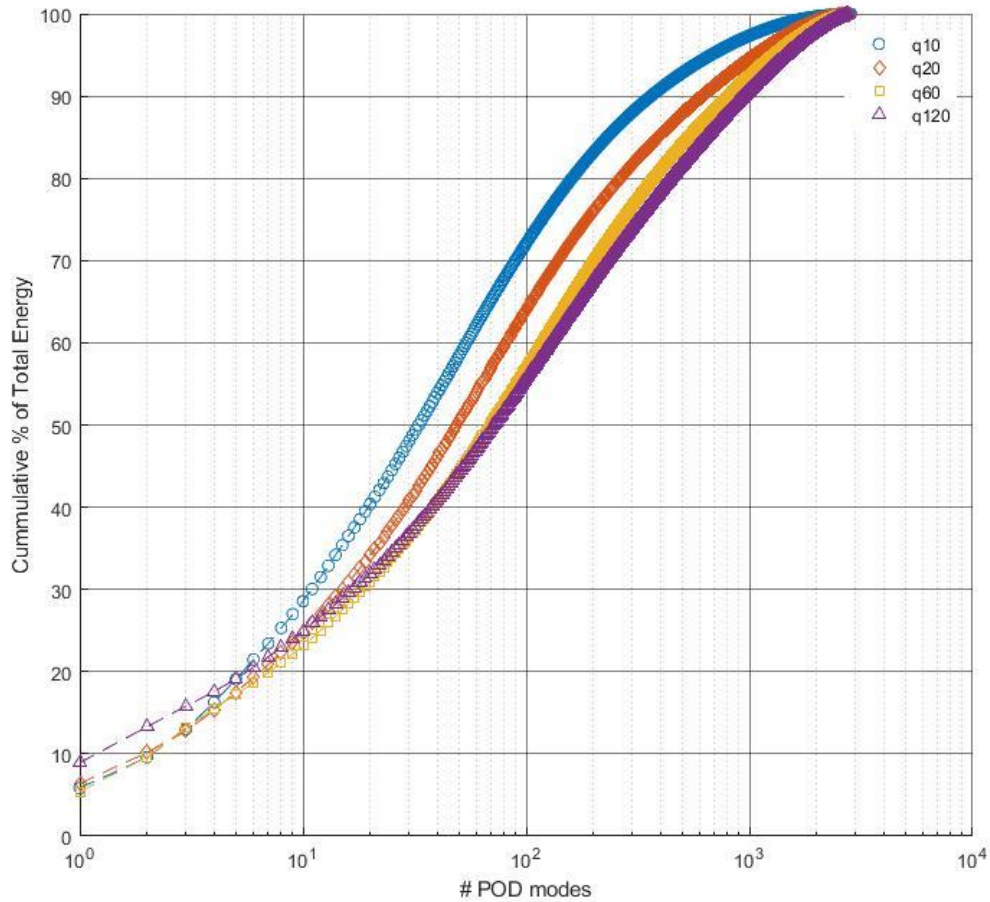
Figure 47: Cumulative energy as a function of increasing POD modes.

3.1.4   Liquid-Gas Interactions

The spatial characterization of both the droplet size distribution and the background gas flow turbulence behaviours have both been characterized and discussed independently however, since the droplets are locally interacting with the gas flow turbulence, there is certainly some relation that exists between them which has not yet been explored in the scientific literature. Such knowledge is crucial as it provides a deeper insight to better understand the interaction between the droplets and background turbulence, which is crucial to understand the underlying physical process. As the data from PIV images provide information about droplets and background turbulence locally, the size of individual

droplets and the corresponding local flow properties in the vicinity of droplets were combined to investigate relationships between these variables.

The Sauter mean diameter (SMD) is plotted versus the local mean streamwise velocity in Figure 48 for all four momentum flux ratios. The results show that the momentum flux ratio significantly influences the relationship between the droplet size and the local mean velocity. The lowest momentum flux ratio does not show any strong relation between the droplet size and the local mean velocity. Figure 48a illustrates the large concentration of droplets less than 100µm and of velocity vectors between 30-35 m/s in the bottom left-hand corner of the scatter plot. This is a result of quantity rather than any relationship between the two parameters, and it was seen in all scatter plots. There also appears to be a rather weak correlation that larger droplets are found in regions of lower velocity gas. Intuitively, the gas momentum absorbed by larger droplets would be greater, which implies that the gas flow surrounding large droplets is slower. Figure 48b shows that for q of 20, small droplets were found to exist within a large range of mean streamwise velocities, perhaps indicating that droplet relaxation is occurring for these smaller droplets. There is also a moderate trend indicating that the fluid surrounding larger droplets is much closer to the freestream velocity, but slightly decreasing with increasing SMD. Figure 48c and Figure 48d show that at higher momentum flux ratios there is a strong non-linear and inverse relationship between SMD and mean streamwise velocity. The results show that the SMD decreases rapidly from about 300 µm to 100 µm as the mean velocity increases in the lower range (10-20 m/s). In the higher velocity range (greater than 20 m/s), there is gradual decrease in the SMD. The smaller of the droplets (<100µm) primarily exists in the spray plume wake as a result of jet atomization and the wake of the spray also contains a large velocity range as the relatively stagnant flow within the wake slowly returns to freestream velocity which describes the linear trend below 100µm. Larger droplets with SMD >100µm are typically found nearer to the windward edge of the spray plume where velocities also tend to be the slowest. The non-linear shape of this relationship may also be an indication that for SMD < 100µm, and gas velocities >15m/s, droplet relaxation is strong, which allows these droplets to accelerate with the gas; whereas it is more difficult

for larger droplets to advect with the flow and therefore the range of velocities observed for larger droplets is quite small.
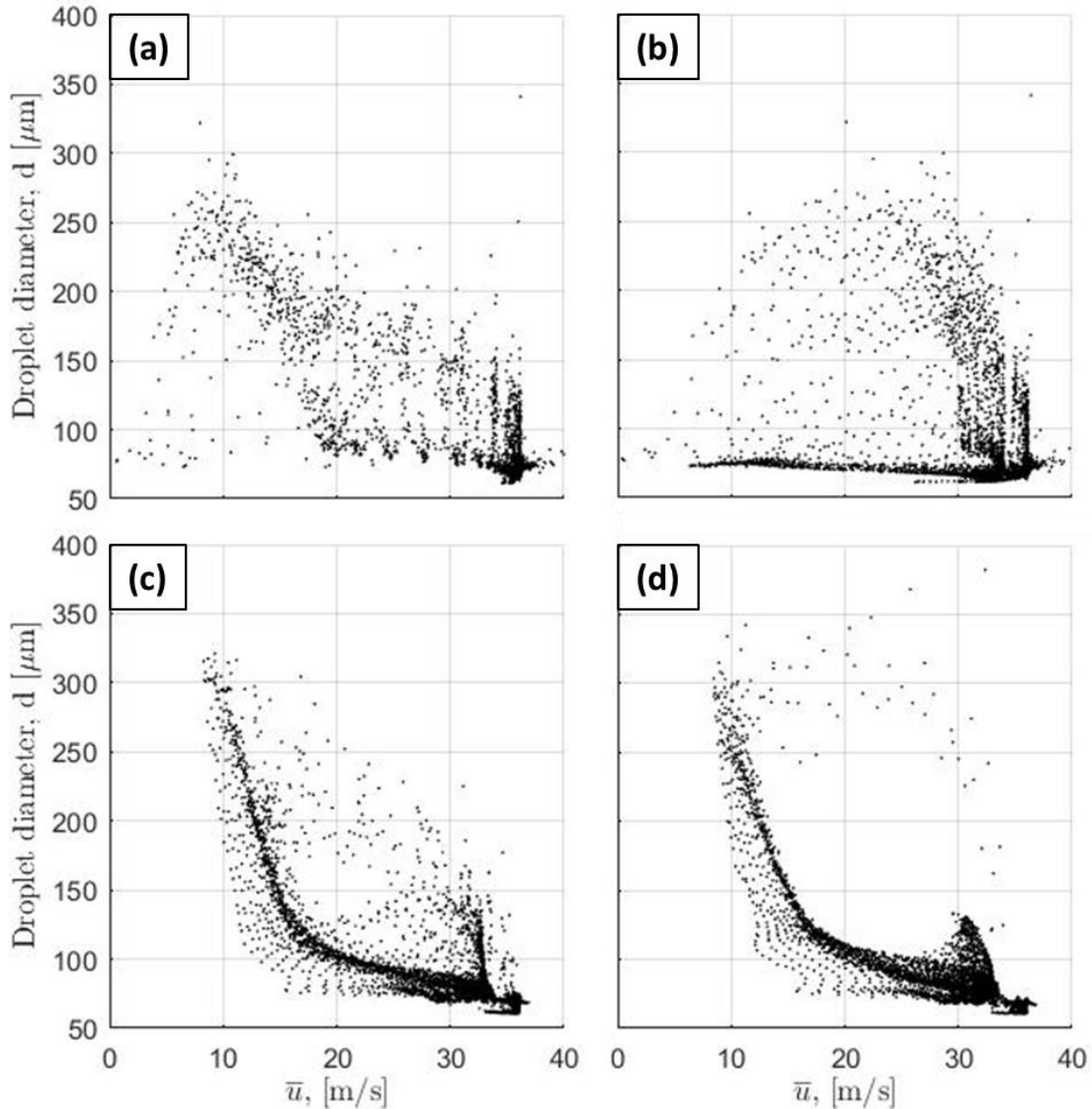
Figure 48: Mean streamwise velocity versus the droplet Sauter mean diameter, for (a) q of 10, (b) q of 20, (c) q of 60, (d) q of 120.

The interaction between droplet size (SMD) and turbulent kinetic energy is examined in Figure 49 for different momentum flux ratio cases. For low momentum flux (q of 10), there appears to be no significant correlation between TKE and SMD. In Figure 49b (q of 20), smaller droplets appear to be strongly uncorrelated with TKE, likely as smaller droplets

are well-dispersed and do not become trapped within any localized turbulent areas. A large range of SMD was found for a relatively narrow range of TKE, indicating that many droplets' sizes exist within the turbulent region of the spray plume. Higher momentum flux ratios show stronger relationships between the droplet size and local TKE as shown in Figure 49c and Figure 49d. The relation is also found to be non-linear between the droplet sizes of 50µm and 150µm with the inflection point occurring around 100µm. Overall, this indicates droplets of all sizes were found in areas with and without turbulence, and that droplets between 50µm and 150µm were found in weakly turbulent regions such as in the wake of the spray plume or in the spray bar wake. In fact, the spray plume wake is the more likely location, as these features were very similar between q of 60 and 120 in comparison to either q of 10 or 20.
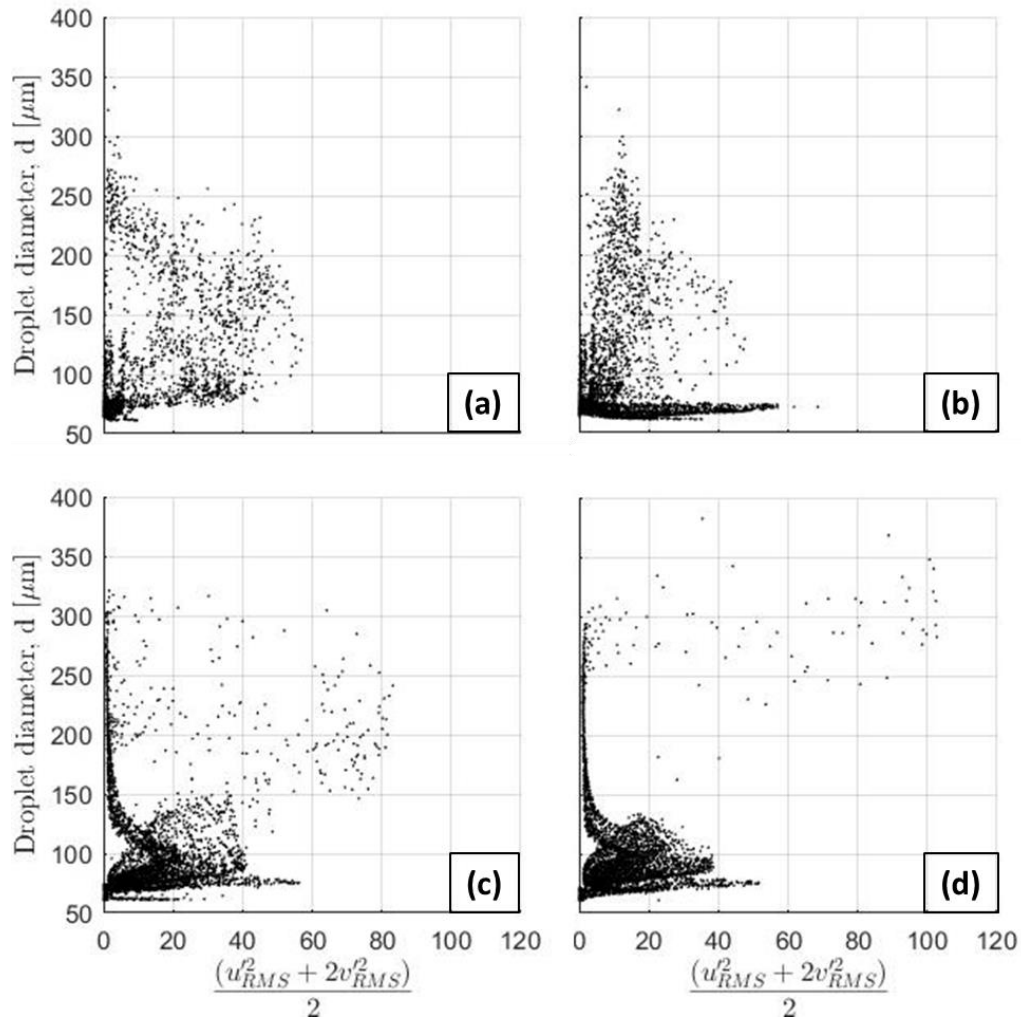
Figure 49: Turbulent kinetic energy (TKE) versus droplet Sauter mean diameter, for (a) *q*= 10, (b) *q*= 20, (c) *q*= 60, (d) *q*= 120.

Figure 50 shows the relationship between turbulent vorticity and droplet size. Similar to the relationship with TKE, low momentum flux ratios show fairly weak (if any) relationship between the droplet size and local turbulent vorticity, and primarily indicate that small droplets are found to be dispersed in areas with varying turbulent vorticity strength. No strong trend was found to suggest that droplets favour areas that have low strength vorticity, perhaps an indication of the mixing characteristics of turbulence. At higher momentum flux, a non-linear trend is found similar to that between the droplet size and TKE. Sauter mean diameters between 50µm and 150µm were found in regions with a fairly large range of vorticity strength.
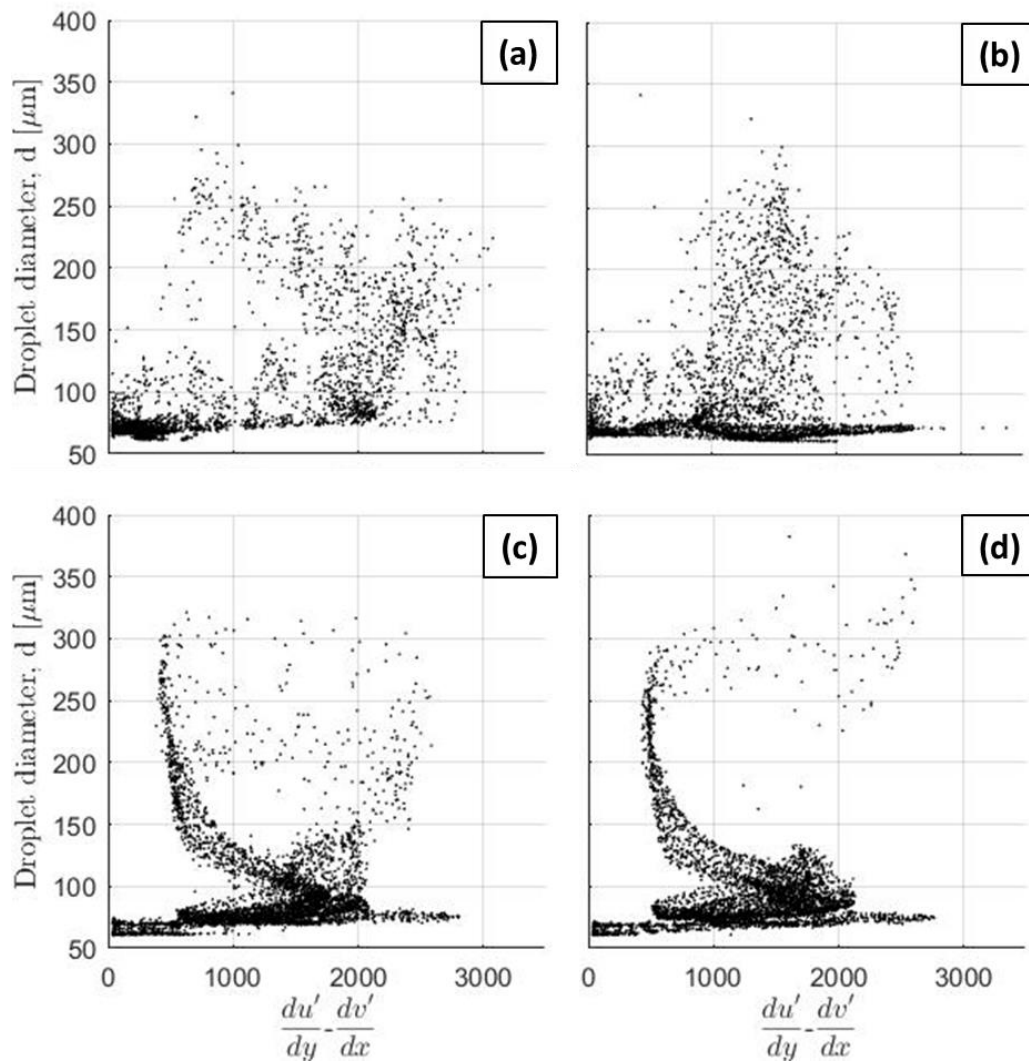
Figure 50: Turbulent vorticity versus droplet Sauter mean diameter, for (a) *q*= **10,**

(b) *q*= **20, (c)** *q*= **60, (d)** *q*= **120.**

3.2   Jet-in-Counterflow

A PIV analysis of a jet-in-counterflow configuration was also performed. Figure 51 shows sample PIV image to describe the behaviour occurring for jet-in-counterflow. Note the obstructions of the seeded gas flow upstream of the spray bar, which is due to the perspective view of the spray bar from the camera viewing angle as well as the high concentration of liquid phase injected upstream of the spray bar (the white saturated region). For this reason, the field of view under investigation for the jet-in-counterflow was considered that was downstream of the spray bar. As such, all results were only examined

downstream of the spray bar. It should also be noted that damage to the test section wall created two very thin shadows across the PIV field of view. Unfortunately, these shadows were consistent and resulted in poor vector quality in this region. Therefore, these regions were masked out in the data, interrupting the view, but not drastically affecting the visibility of the results. Figure 52 shows a raw PIV image at each momentum flux ratio (q of 10/20/60/120).
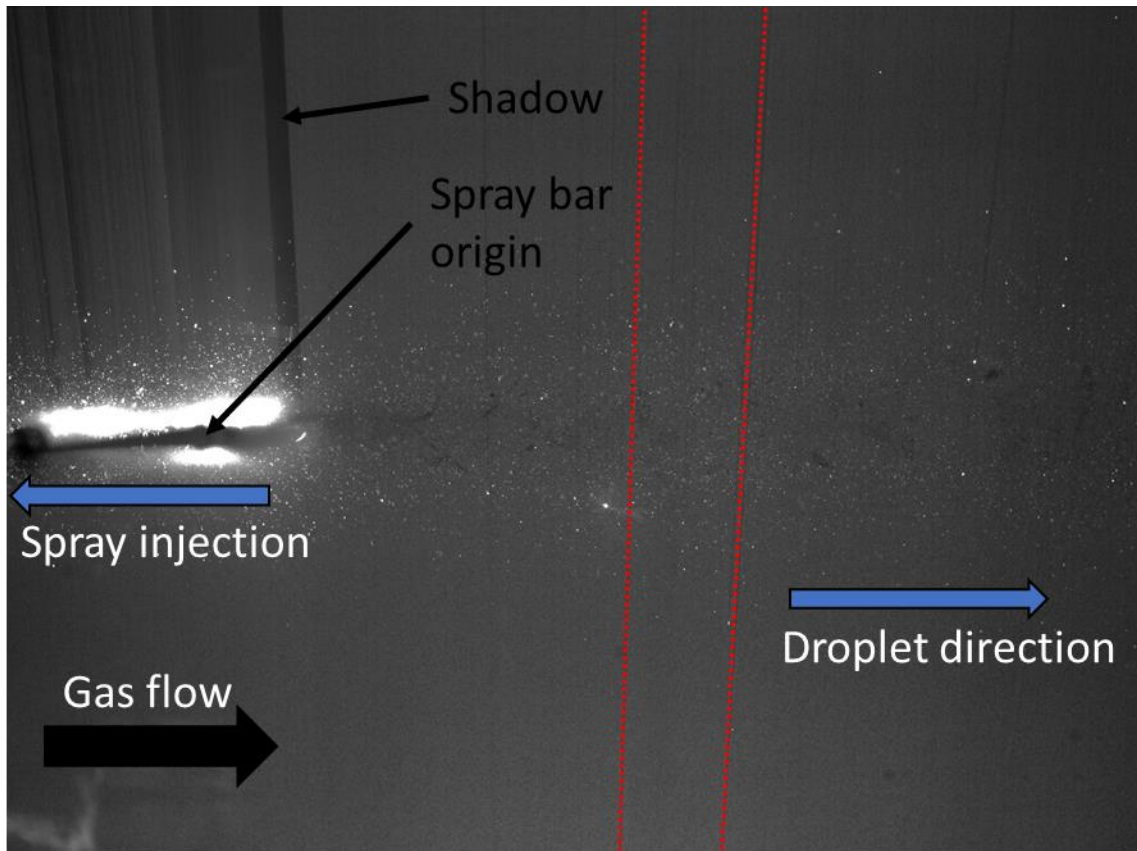
Figure 51: Sample raw PIV image of jet in crossflow identifying key features (q of 60). The red dotted lines shown identify very thin shadows created by scratches in the acrylic wall.
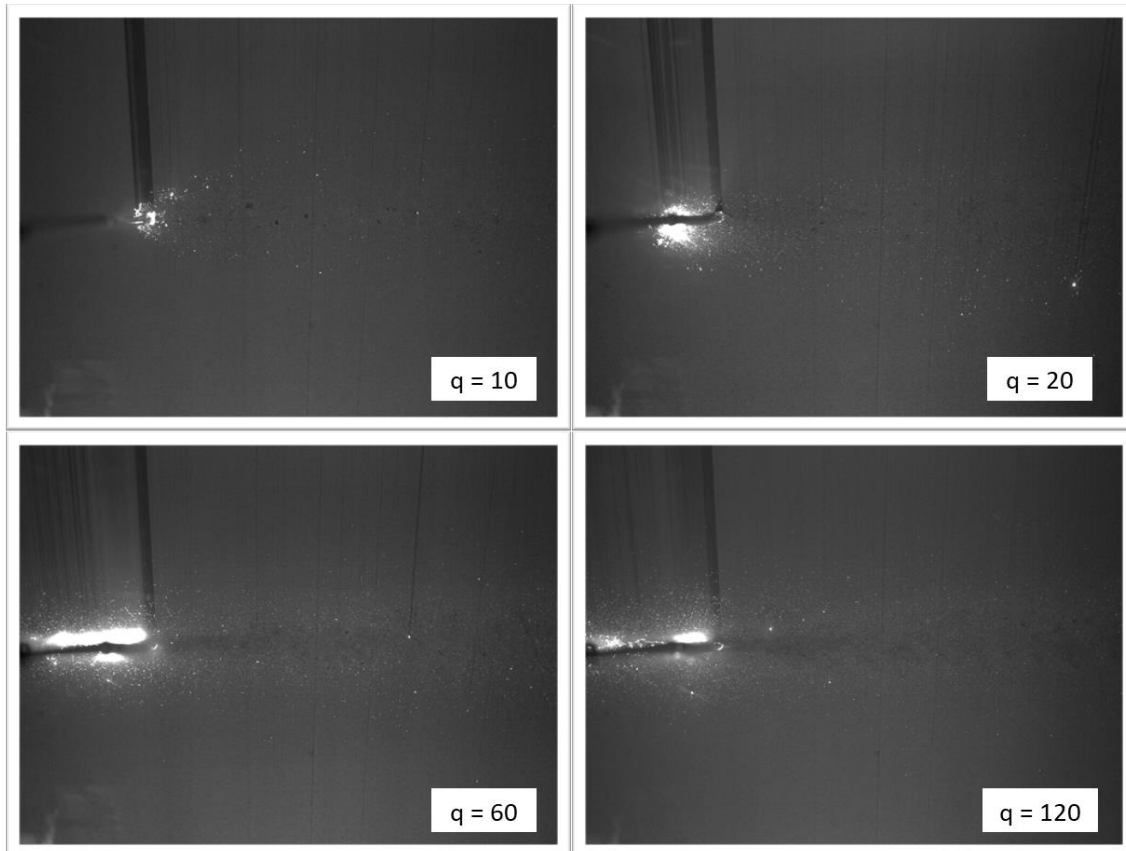
Figure 52: PIV image samples for the jet-in-counterflow spray at various momentum flux ratios. The air flow direction was from left to right in the images.

3.2.1   Spray Characteristics

Figure 53 shows the probability distribution of equivalent droplet diameter for the entire field of view. Unexpectedly, the lowest momentum flux case (q of 10) contained the greatest proportion of 61µm (or less) droplets at 81.5%, and a total of 92.3% of droplets less than 87µm in size. At higher momentum flux ratios (q of 60/120), the smallest droplets represented less than half of the detected droplets at ~45%, and with the 83.1% of droplets less than 121µm it is clear that there is a greater variation in droplet size for there higher flow cases. Overall, it appears as though increasing momentum flux ratio for jet-in-counterflow reduces the number of small droplets and favours larger droplets. This suggests that maybe the lower turbulence seen at q of 60 and 120 is indeed affecting droplet breakup.
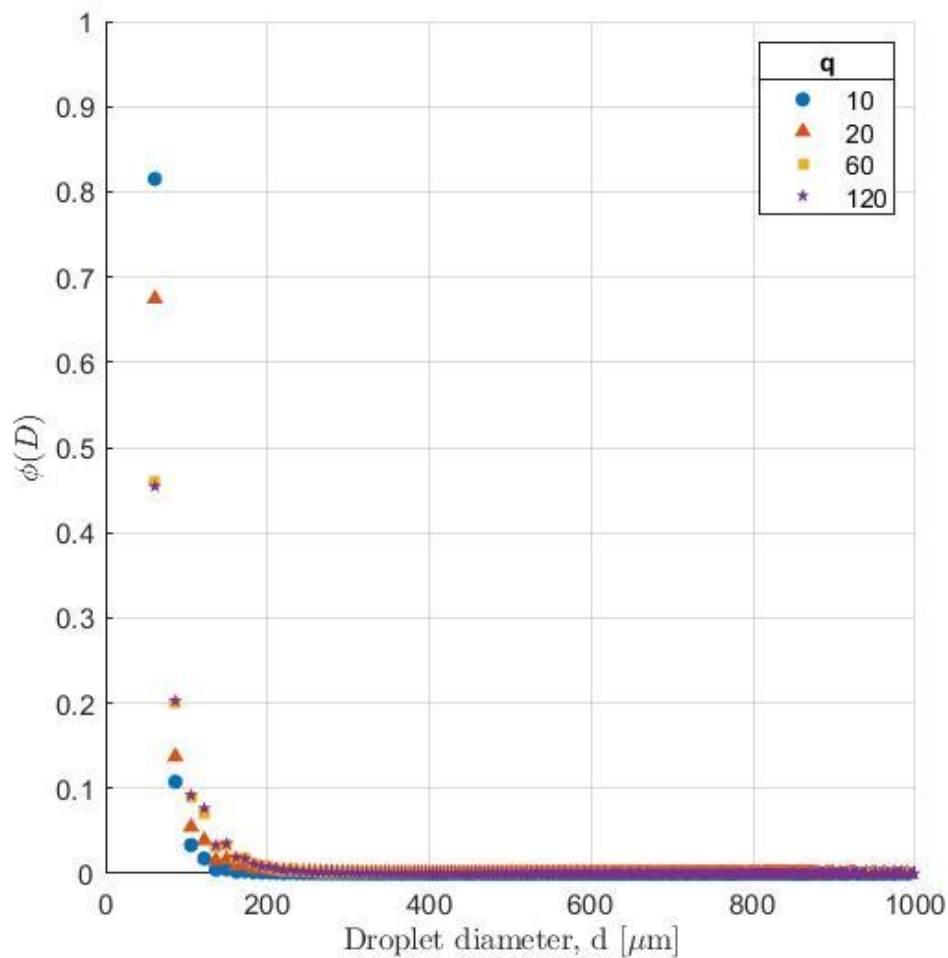
Figure 53: Probability distribution Φ(d) of droplet diameter for jet-in-counterflow at different momentum flux ratio cases (q=10/20/60/120).

The spatial size distribution of droplets is illustrated in Figure 54 as colormaps over the measurement field of view for the four momentum flux ratio cases. The results show that increasing momentum flux ratio greatly increases the spanwise coverage of the spray droplet plume, and for lower momentum flux ratios, the spray plume expands noticeably within a distance of $150d_o$ downstream of the spray bar. Interestingly, the largest droplets for q of 60 and 120 flows appear to be in the wake of the spray bar rather than at the periphery of the spray plume. This observation may be evidence of the accumulation of liquid on the surface of the spray bar, simply due to the large liquid flow rates being used, and thus droplets are remaining attached to the spray bar and do not detach until they are

within the wake. These larger droplets then seem to quickly reduce in size once released from the spray bar. Also, the spray bar wake region appears to contain relatively small droplets. The SMD size distribution appears quite uniform within the spray plume other than the axis of symmetry which contains the spray bar wake. As before, note that the white regions are areas where no droplets were detected by the algorithm.
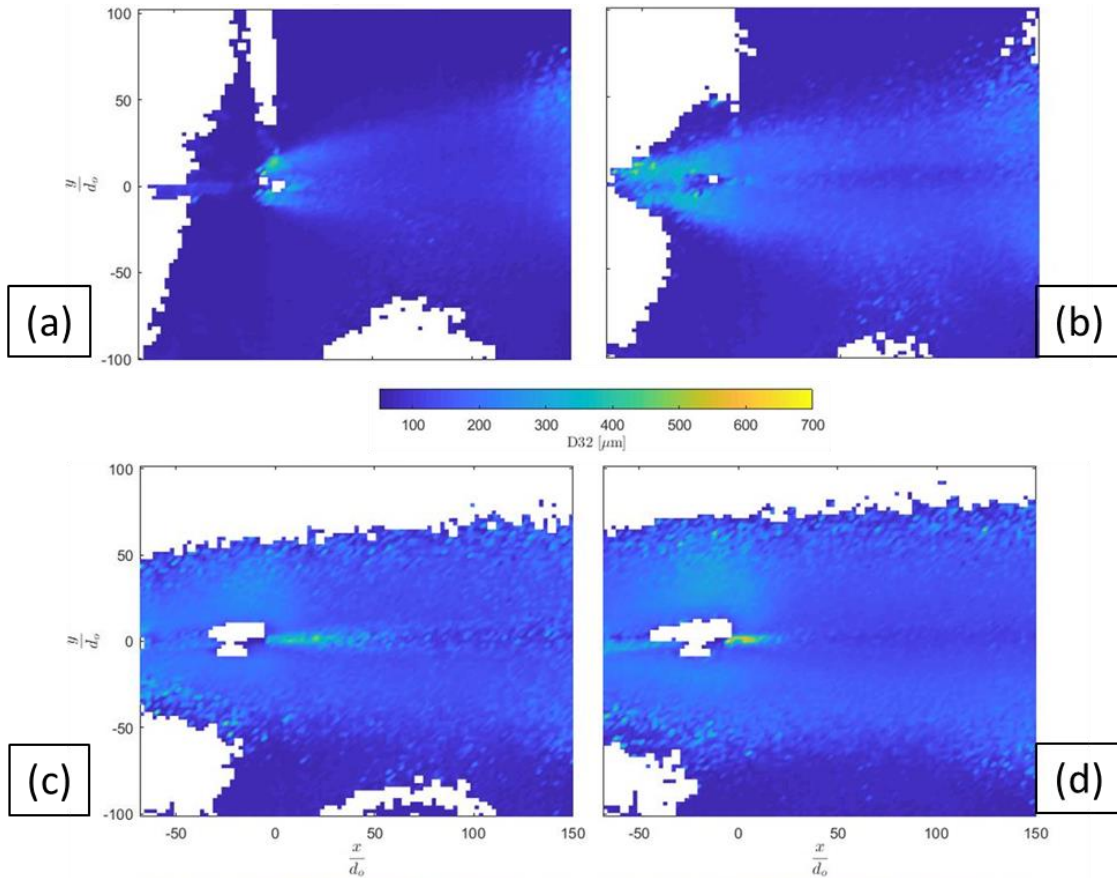
Figure 54: Color maps of the spatial distribution of the droplet SMD for (a) q=10, (b) q=20, (c) q=60, (d) q=120.

Figure 55 shows the spanwise SMD profile of droplets at different downstream locations for q of 120. The spanwise profiles of the droplet size distribution are very consistent at these downstream locations, with the exception of a few large SMD spikes. The SMD is largest at the spray boundaries, which appears to be at approximately $y/d_o = \pm 50$, and SMD gradually decreases towards the spray bar wake. Figure 56 shows the spanwise SMD profile of droplets for all momentum flux ratios, at $50d_o$ downstream from the spray bar.

Cases at q of 20, 60 and 120 demonstrate very similar behaviour as well as similar SMD magnitudes. The exception is for q of 10 which does not seem to have a symmetric profile and in fact seems to have its largest SMD near the spray bar wake.
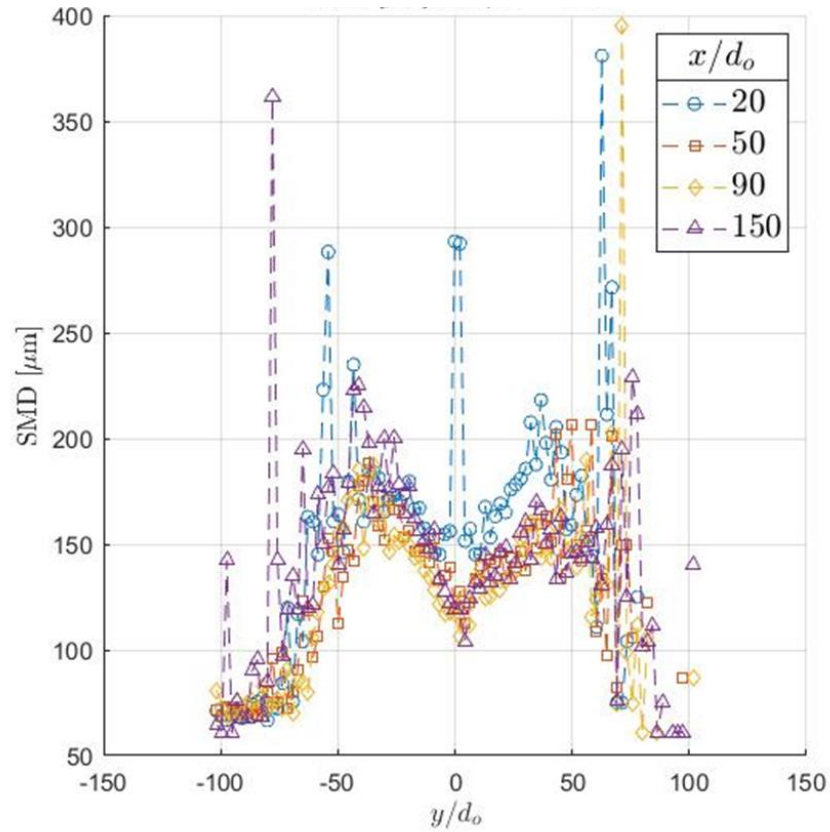
Figure 55: Spanwise profile of droplet SMD at various downstream locations for q of 120.
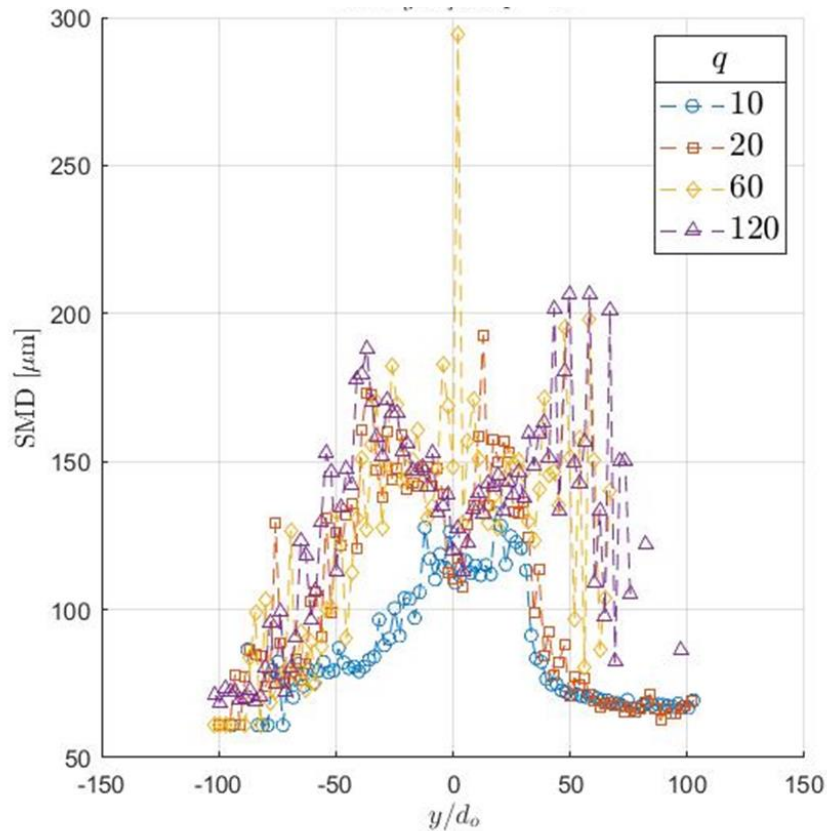
Figure 56: Spanwise profile of droplet SMD at 50d$_o$ downstream of the spray bar for different momentum flux ratios (q=10/20/60/120)

Overall, the droplet size for droplets resulting from JIC spray were larger than those found for JIX. This was most evident at higher momentum flux ratios (*q* of 60 and 120), where more than 85% of droplets produced by JIX were less than 100μm, whereas less than 70% of droplets produced by JIC were less than 100μm in diameter. The distributions were similar, only in that the larger droplets relative to both sprays were found at the spray periphery (the shear layer between the spray and the freestream flow).

3.2.2   Mean Flow

The mean flow for the jet-in-crossflow spray is quite congruent with the freestream velocity when compared to the jet-in-crossflow. Figure 57 illustrates the contour maps of the mean streamwise velocity at different momentum flux rations. These plots show that, as the momentum flux increases, the increased volume of liquid phase present in the flow,

decelerates a progressively larger region of the gas flow. Unlike the jet-in-crossflow spray, there was no significant amount of flow acceleration around the spray plume. Figure 58 shows the contour map of mean spanwise velocity field at q of 120, which indicates minor spanwise movement of the flow.
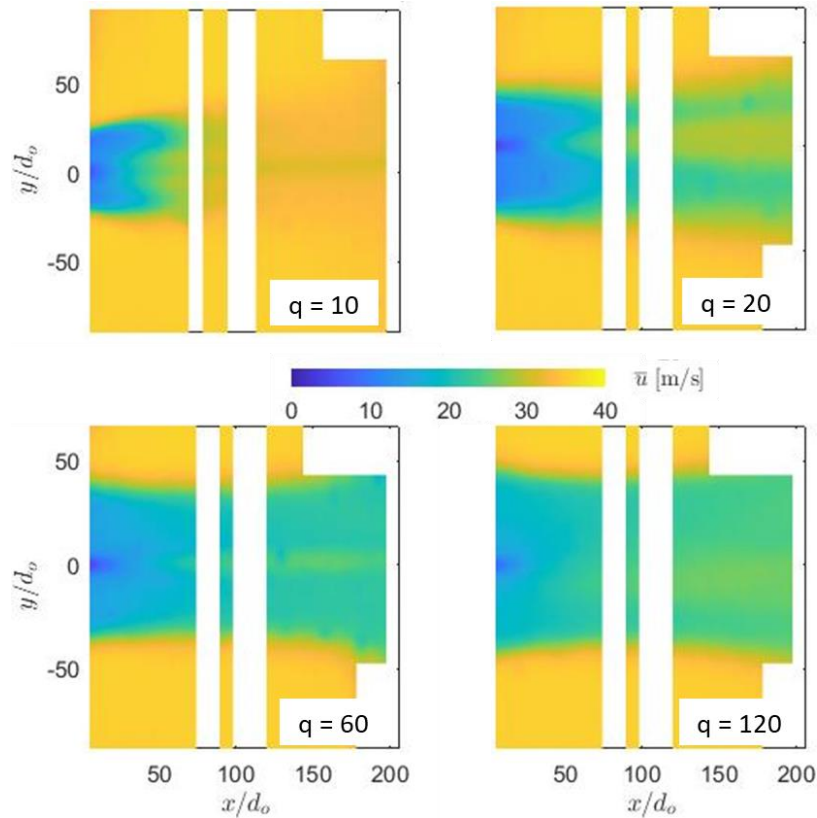
Figure 57: Color plot of the mean streamwise velocity [m/s] for q of 10 (upper left), 20 (upper right), 60 (bottom left), and 120 (bottom right)
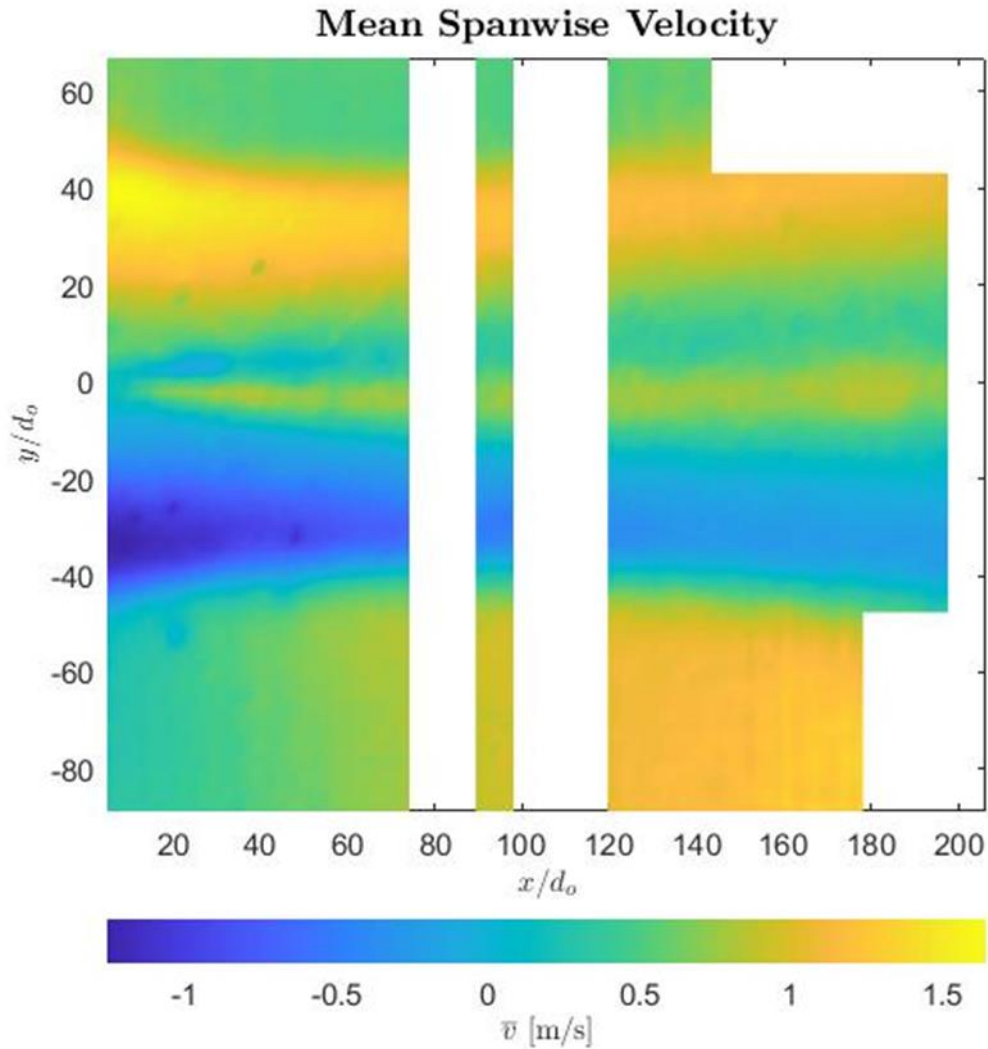
Figure 58: Color plot of the mean spanwise velocity [m/s] for *q* of 120

3.2.3   Turbulence

Figure 59 shows the contour maps of turbulent kinetic energy (TKE) at different momentum flux ratios. The results show that the turbulence is strongest in the shear layer at the interface of the spray boundary and the gas flow. Relatively higher turbulence magnitudes are also observed in the middle region, which is likely associated with the wake formed by the spray bar. The results also show an increase in the spanwise extent of the turbulence zone with the momentum flux, which is expected to the increase in the extent of the spray zone.   The turbulent velocity fluctuations are primarily dominated by the

streamwise velocity fluctuations, particularly at the spray boundaries. Figure 59 shows the TKE distribution for all momentum flux ratios, and Figure 60 shows the spanwise RMS velocity fluctuations. As shown, the magnitude of v'_{RMS} contributes marginally to the magnitude of TKE and is primarily dominant along the axis of symmetry of this flow $(y/d_o = 0)$ which is an indication that the spray bar wake remains present in this counterflow configuration.
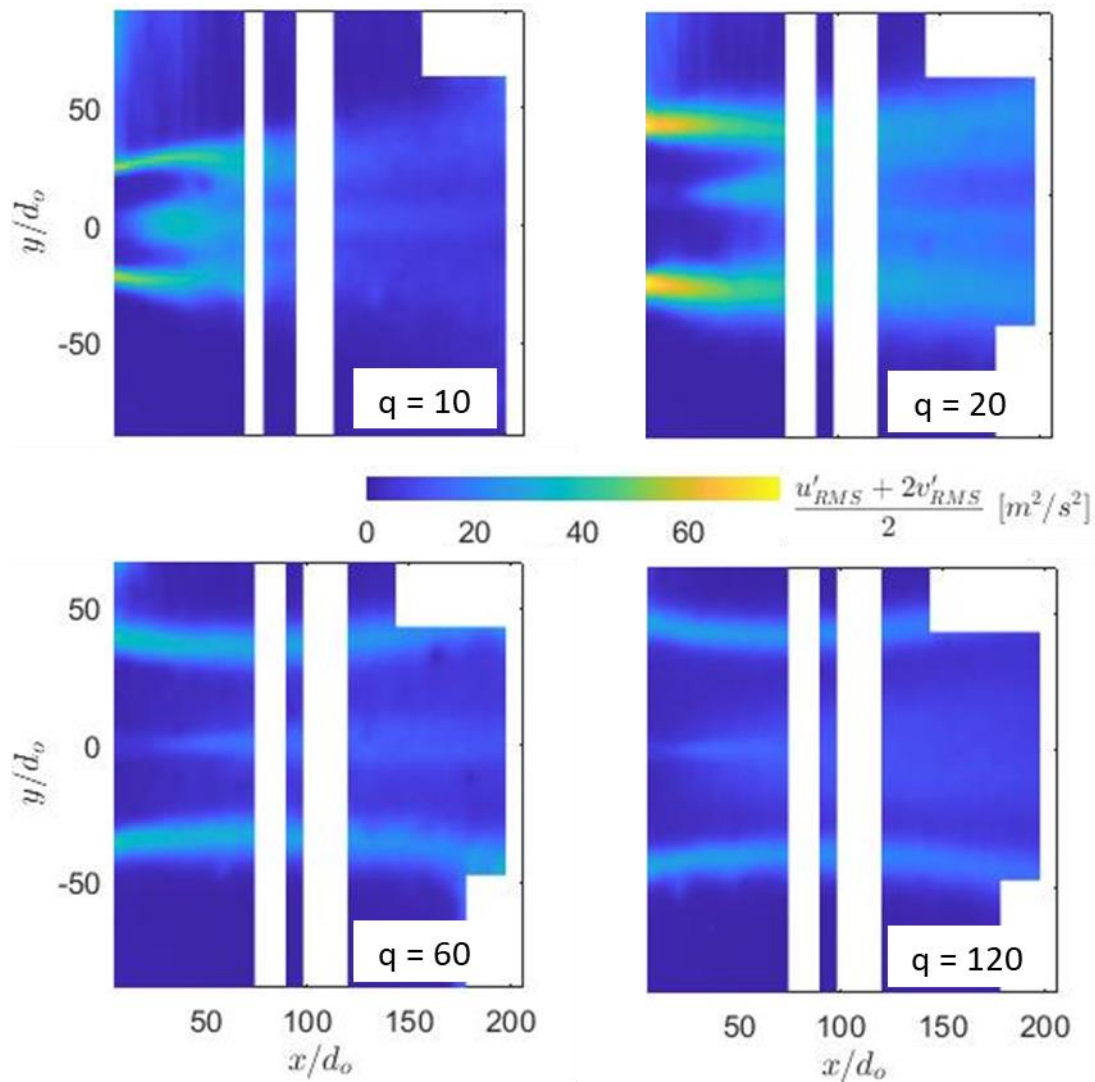
Figure 59: TKE signatures in the spray plume boundary as well as down the plume centerline

Spanwise RMS Velocity Fluctuations
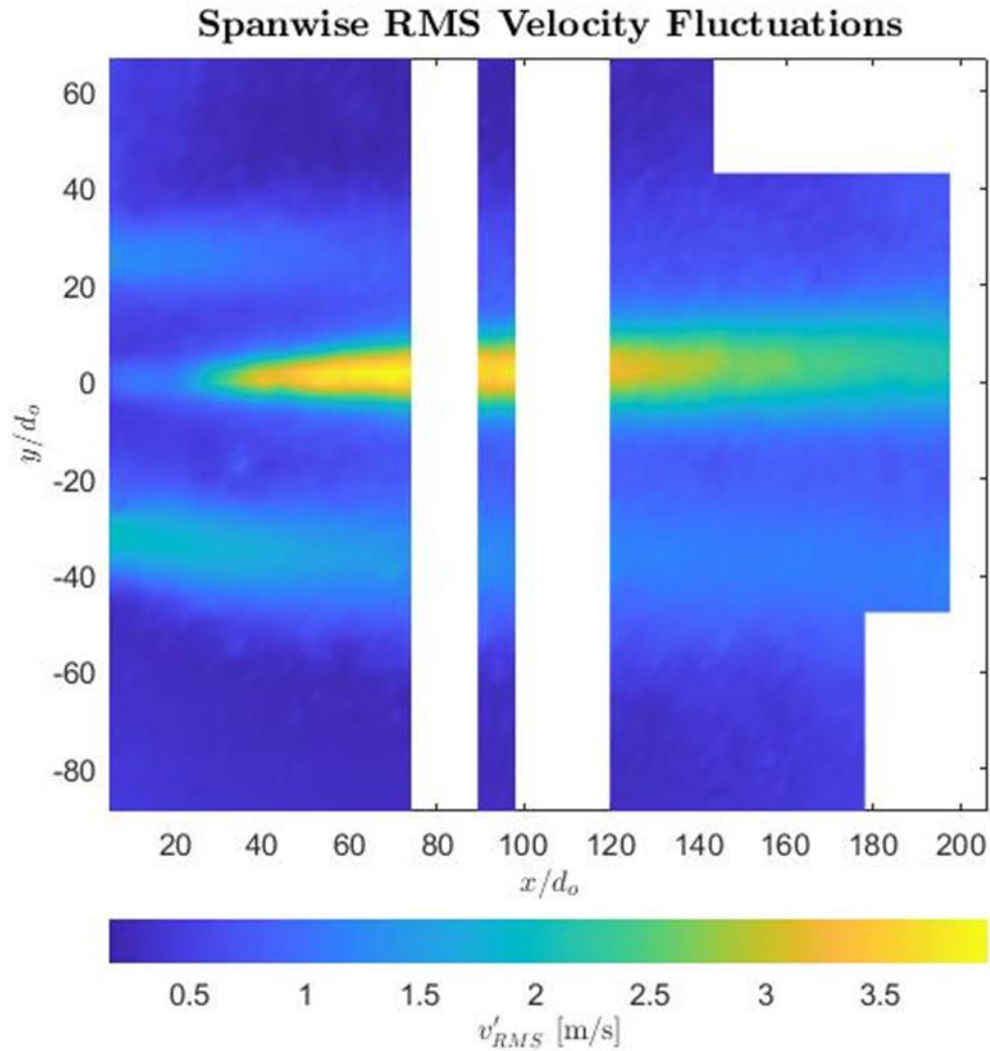
Figure 60: Color plot of the spanwise velocity fluctuations for q of 20.

As shown in Figure 59, the TKE magnitudes were largest at q of 20, which at its peak, is nearly double the TKE for momentum flux of 60 and 120. It should be noted that the most turbulent regions at the two higher momentum flux ratios are much farther upstream of the spray bar than for the q of 20 case due to the increased upstream penetration of the higher flow rate cases. For the momentum flux ratio of 10, there may not have been enough shear

due to the smaller difference between injection velocity and freestream velocity, therefore resulting in less turbulence generation.

Figure 61 illustrates the Reynolds shear stress for each momentum flux ratio. Expectedly, the shear stress appears to be strongest in the flows with the larger gradients downstream of the spray bar (q of 10/20). It is likely that shear stress for q of 60 and 120 is located further upstream as with TKE.
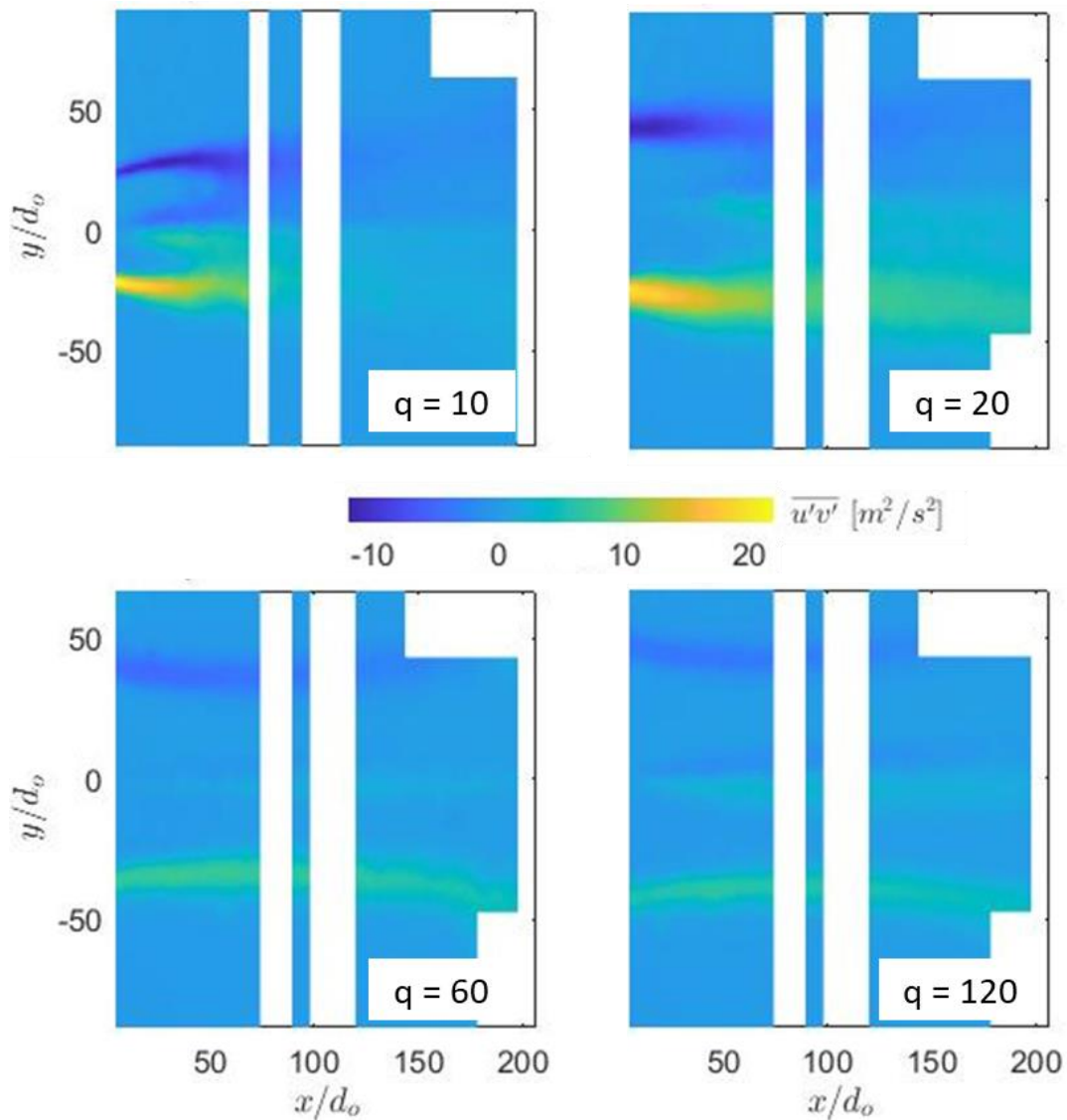
Figure 61: Reynolds shear stress for all momentum flux ratios

As with the crossflow study, examining the progression of turbulence at several downstream locations is of interest. Figure 62a and Figure 62b show the spanwise distribution of shear stress at $\frac{x}{d_o} = 20, 50, 90$, and 150. The location $100d_o$ downstream could not be examined due to the masked regions covering the scratch shadows. As seen in the color maps, the lower momentum flux ratio shows much larger shear stress magnitudes, however it is clear that the peak values are reduced between $90d_o$ and $150d_o$ downstream of the spray bar. At the highest liquid flow rate, the shear stress appears to be relatively constant in magnitude even as early as $20d_o$ from the spray bar. In Figure 63, all momentum flux cases are plotted $150d_o$ downstream of the spray bar. The magnitudes of shear stress for all cases are drastically lower than the peaks found near the spray bar at q of 10. In fact, momentum flux of 20, 60, and 120 have near identical profiles and magnitudes, whereas q of 10 has even lower overall magnitudes. So, while the lowest momentum flux created the largest localized shearing, it dissipated much more quickly.
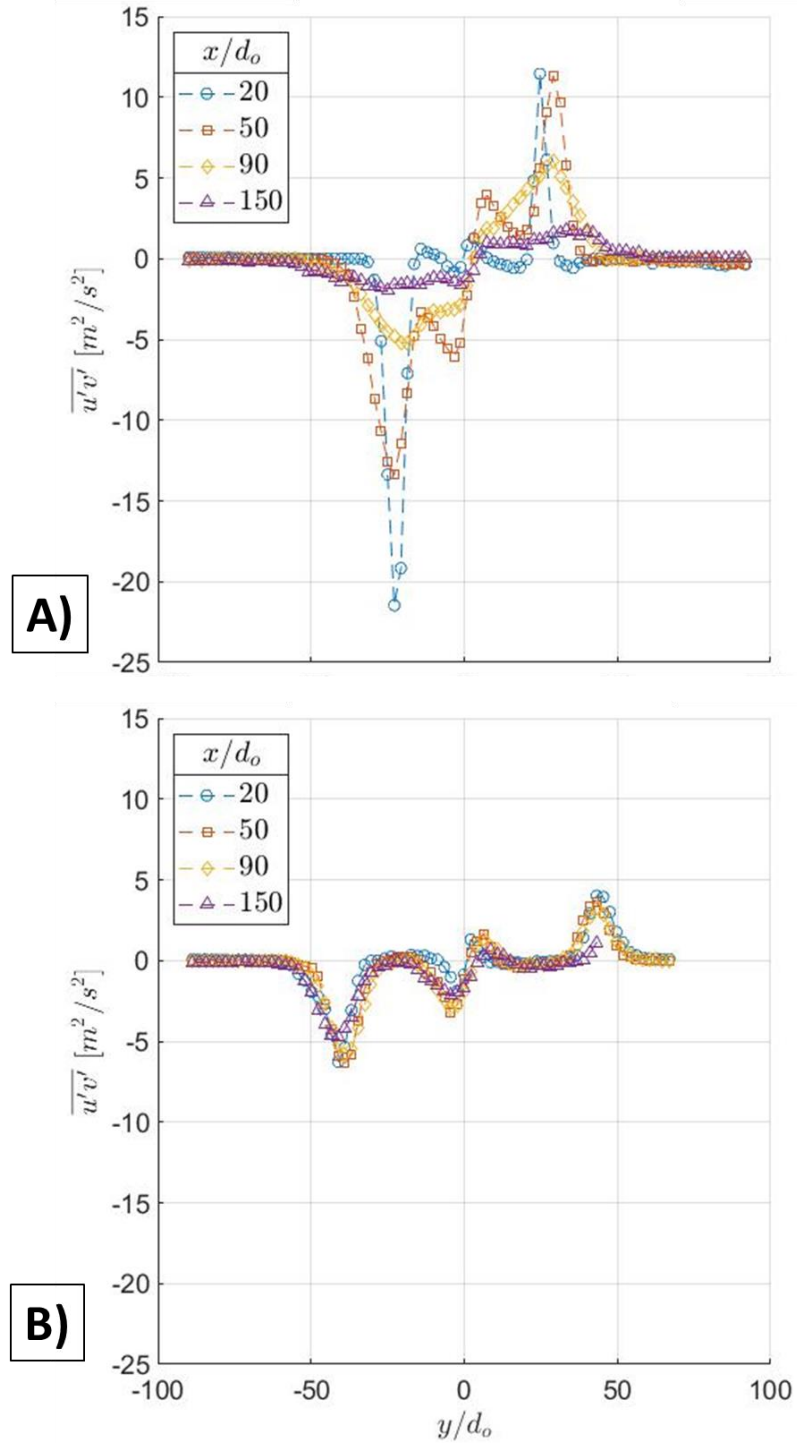
Figure 62: Spanwise distribution of Reynolds shear stress at various locations downstream from the spray bar for A) *q*= 10 **and B)** *q*= 120.
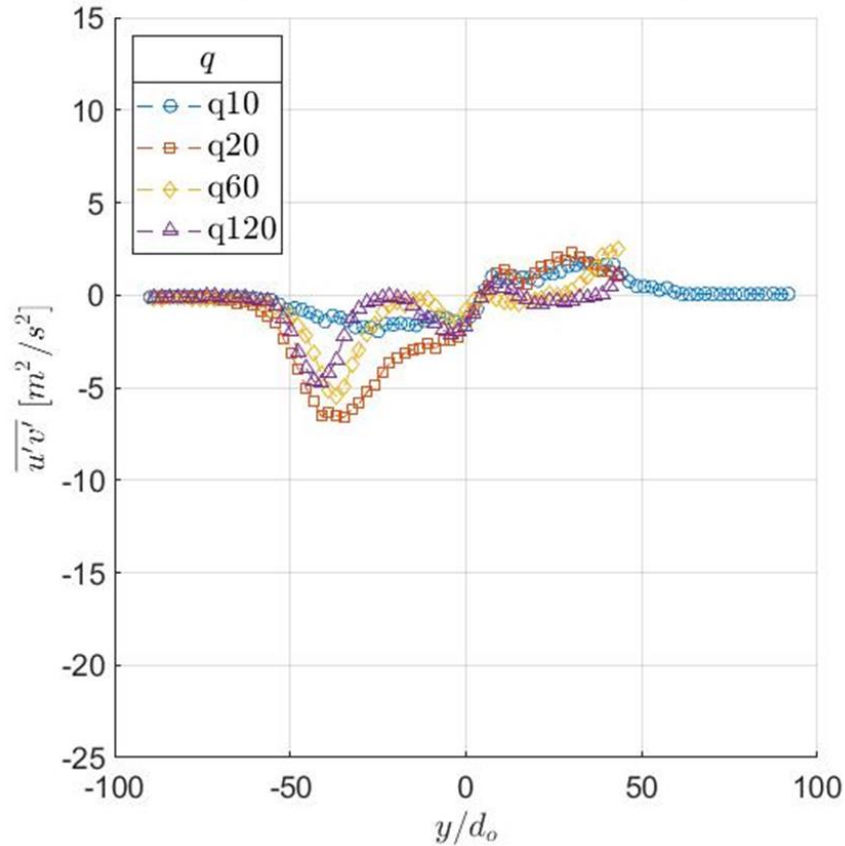
Figure 63: Spanwise distribution of Reynolds shear stress 150d_o downstream of the spray bar for all momentum flux ratios.

Due to the almost imperceivable amount of jet penetration achieved at *q* of 10, it is likely that not jet is formed on exit from the spray bar. The droplets then remain attached to the spray bar via surface tension or exit the injection orifice in a more disorganized manner. In addition, the quantity of droplets exiting would be lower due to the reduced liquid flow rate. This may allow for droplets to spread over a larger area downstream of the spray bar and for better mixing to occur with the gas flow.

The droplet distribution results presented earlier show that the measured droplet size did not vary considerably in the downstream direction. This suggests that the momentum transfer from the mean flow did not contribute to the breakup of larger droplets.

3.2.4   Liquid-Gas Interactions

Using the detailed knowledge of the turbulence characteristics of the jet-in-counterflow, as well as the spatial distribution of the droplets, the relationship between them can be investigated.

Figure 64 shows the relationship between the local mean streamwise velocity and droplet SMD. For q of 10 (Figure 64a), the figure shows two relatively strong trends in the relationship between the local mean streamwise velocity and droplet size. At high gas velocity, the droplet sizes appear to be independent of the local mean velocity. However, in mid to low range of velocities, the results show a decrease in droplet size as the local mean velocity increases. Since lower velocities were only found in a short region directly downstream of the spray bar it appears that as droplets escape this low velocity region they begin to decrease in size, possibly due to velocity gradients. Otherwise, at q of 10, all droplets essentially travel near the freestream velocity of 35m/s. At q of 20, a decreasing trend of droplet size with the mean velocity is observed only in the lower range of velocities. At further higher momentum flux ratios, the results do not show a strong relationship between the droplet size and local mean velocity.
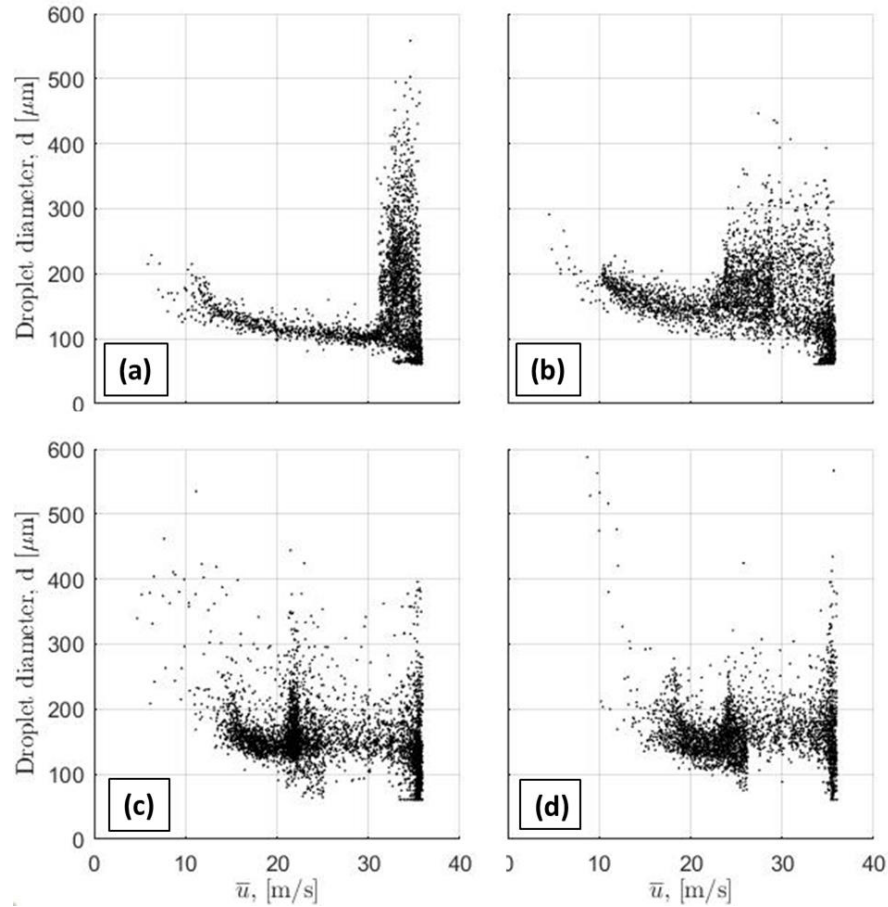
Figure 64: Streamwise local mean velocity versus droplet SMD, for (a) q=10, (b) q=20, (c) q=60, (d) q=120.

Figure 65 shows the relation between the local TKE and droplet SMD for different momentum flux ratio cases. The results overall, do not show strong relationships between the local TKE and droplet size in this spray configuration. Some weak trends are observed at q of 10 and 20, in the higher magnitude range of TKE, where a slight increase in the droplet size is observed with an increase in the TKE magnitude. As discussed, this likely indicates that turbulence is no longer participating in droplet breakup in the region studied, but rather in droplet acceleration.
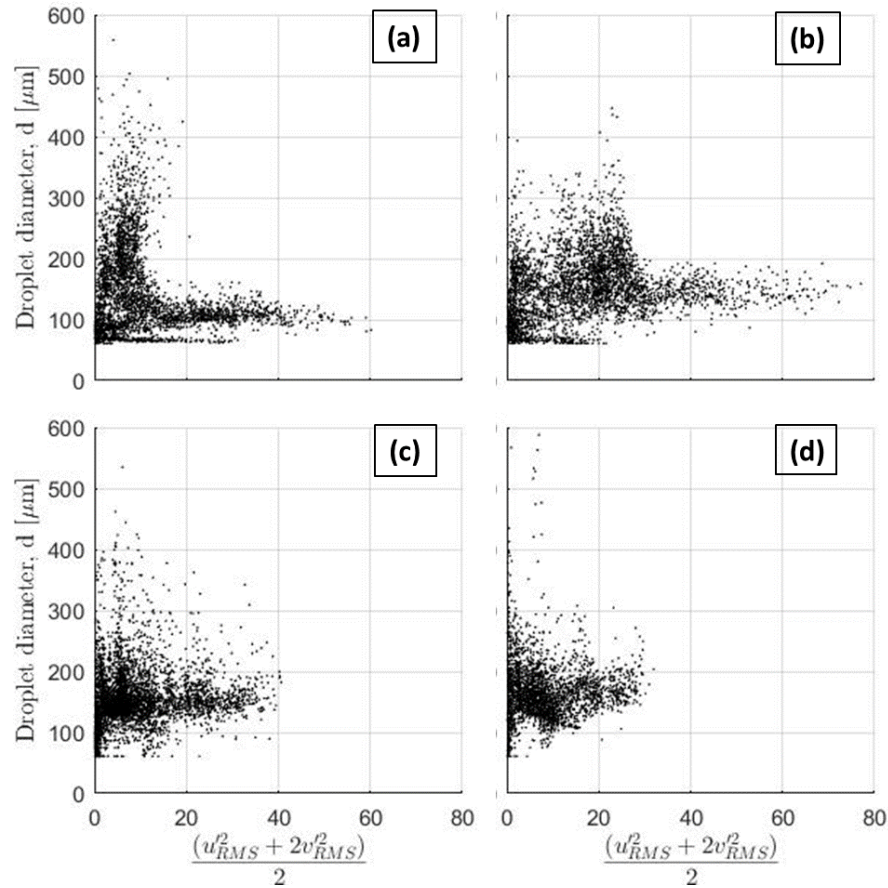
Figure 65: Local TKE versus droplet SMD, for (a) q=10, (b) q=20, (c) q=60, (d) q=120.

Figure 66 plots the turbulent vorticity versus the droplet SMD for different momentum flux ratio cases. Similar to the TKE results, the plots do not show a strong relationship between the local turbulent vorticity and the droplet size at these momentum flux ratio cases. A weak trend of an increase in the droplet size with an increase in turbulent vorticity is observed.
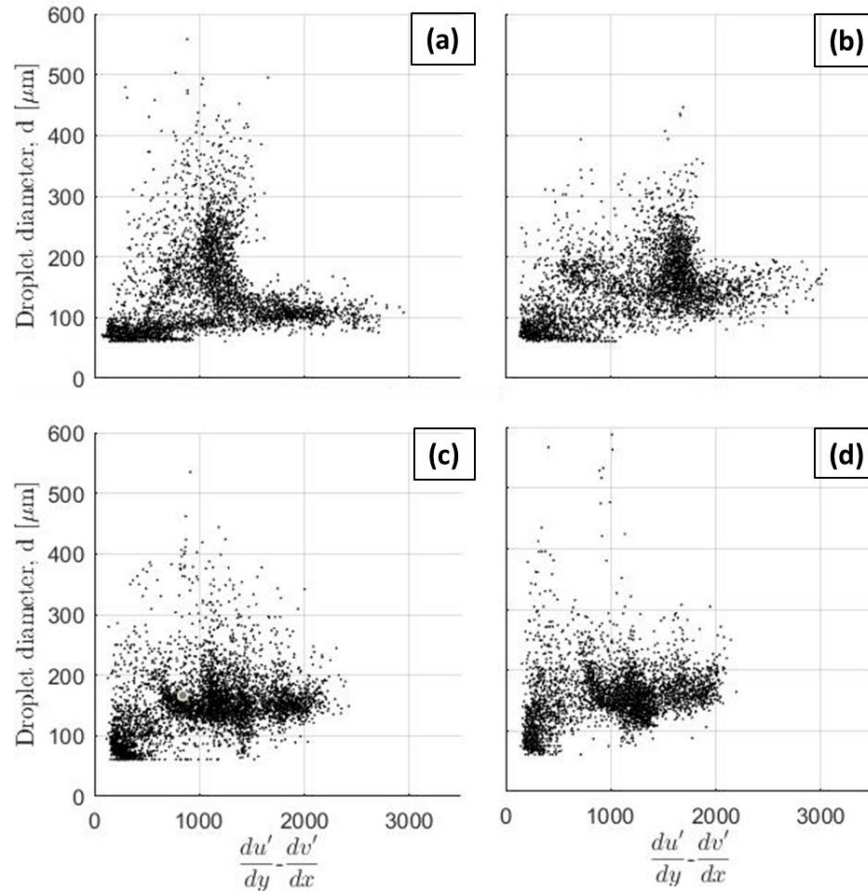
Figure 66: Local turbulent vorticity versus droplet SMD, for (a) q=10, (b) q=20, (c) q=60, (d) q=120.

3.3　Discussion

In preceding sections, results are presented that characterized the mean and turbulent flow fields, the droplet size distribution and the interaction between the local flow field and the liquid droplets. It is observed that for the jet-in-crossflow configuration, the spray plume created a region of slow moving but organized flow bounded by a highly turbulent shear layer on the windward side of the plume, and a moderately turbulent spray plume on the leeward side. This in turn also caused the freestream flow to accelerate slightly in areas where the spray was not obstructing the flow to satisfy the mass conservation. It is observed that the turbulence was strongest in the shear layer downstream of the spray bar, which gradually became weaker along the spanwise direction. The POD analysis showed that the

momentum flux ratio had an influence at lower POD modes. At high momentum flux ratios, the largest fraction of energy was contained in low POD modes.

The results also show that the liquid jet breakup was quite effective in this configuration where over 90% of detected droplets were under 100µm. This is in agreement with liquid jet-in-crossflow literature which regularly reports droplet sizes in the 30 to 60 micron range. The spatial distribution of the droplets showed that the larger droplets have increased penetration and tend to stay on the perimeter of the spray plume, which is consistent with the trend reported in the literature. Droplets were found to get progressively smaller as they advect through the spray plume. Overall, the peak SMD was found to increase with an increase in the momentum flux ratio. A novel aspect of this study was the ability to investigate the interaction between the local turbulence and the droplets. The results show a strong relation between the local flow behaviour and the droplet size at high momentum flux ratios. The droplet diameter was found to decrease with an increase in the mean freestream velocity, indicating that the mean shear plays an important role in the droplet breakup. Non-linear correlations were also found between turbulent parameters (TKE and vorticity) and SMD. There appeared to be an inflection point at a particular droplet size, ~90-100µm, around which turbulence was largest. The most turbulent region of the flow is the windward shear layer between the liquid column/spray plume and the incoming gas. The inflection point captured in the correlational data suggests that droplets which advect through, and downstream of, the shear layer are smaller in size. Given that droplets are generally less than 100µm in size, it is believed that the shear layer is the primary contributor to reduction in droplet size. It could then be supposed that the increased liquid jet penetration at higher momentum flux ratios contributes to more complete atomization due to the creation of a longer shear layer.

For the jet-in-counterflow, it was observed that lower momentum flux ratios displayed higher magnitudes of turbulence in the measured field of view. However, it is that higher momentum flux ratios produce stronger turbulence which was not captured in the measured field of view, due to increase upstream jet penetration. With increased upstream liquid penetration the stronger turbulence produced likely diffused by the time it reached the field of view and hence, in the measurement region, the turbulence was relatively uniform. The

spanwise droplet size distribution profile was well developed and remained relatively unchanged with changes in momentum flux ratio, with the exception of q of 10. The other three momentum flux ratios had largest droplet diameters at the periphery of the spray plume (i.e., at the shear layer between gas and droplet plume), which decreased towards the centre of the plume within the spray bar wake. It is also observed that the spanwise droplet size distribution did not change appreciably with the downstream distance. However, for q of 10, droplet sizes were overall smaller and were not uniformly distributed. No literature was found to be relevant to the injection configuration used in this study however, the droplet SMD found between 60 and 200µm are well within what has been seen in jet-in-crossflow research. The results also show that the correlations between the jet-in-crossflow droplet sizes and turbulent properties was generally weak. This is likely due to the reason that the strong interaction between the liquid jet and the gas flow occurred far upstream and as the gas and droplet flow reached the measurement region, the local interactions were not too strong.

Chapter 4

4 Droplet Behaviour around a Bluff Body Recirculation Zone

A preliminary investigation of the behavior of water droplets flowing around a vee-gutter bluff body was performed. The findings from this preliminary investigation will first be discussed qualitatively, then quantitatively. However, it is important to emphasize that to the best of our knowledge, such investigations are first of its kind in the scientific literature (no previously reported literature on the investigation of flow and/or droplet behavior in vee-gutter geometry), despite the usage of such geometry in the afterburner of fighter jets. Hence, despite being preliminary in nature, the result in this Chapter provides for the first time, the dynamics of droplets in such geometry and highlights some key observations, which provide a first insight into the underlying physical behavior and sets the ground for advanced level investigations.

The initial work plan was set to investigate and describe both the gas and liquid behaviours simultaneously using PIV (similar to the results presented and discussed in the previous Chapter). Although attempts were made to perform these experiments, equipment failure and ill-timed COVID-19 pandemic resulted in a time loss of approximately 3 months (as far as experiments are concerned). Therefore, the scope of this phase of study was revised to use a different measurement approach (with some measurement limitations) to meet at the very least, the primary objective of the basic characterization of droplet dynamics (for the first time) in the presence of vee-gutter geometry. Being first of its kind, these results are still very valuable to the scientific research related to afterburners. The details of the experimental setup, measurement techniques and data analysis are already described in Chapter 2.

4.1   Qualitative Analysis

The high-speed imaging served as a useful tool not only for the quantitative analysis but also for qualitative analysis to obtain a deeper insight into the dynamics of droplets in this configuration. The recorded frame rate of 8,000 frames per second was sufficient to be able to follow the motion of in-plane droplets both at fast (8.26µs) and slow (50µs) shutter speeds. These shutter speeds will be referred to by the shape of droplets in each case, namely non-streak and streak images, respectively. Figure 67 shows a streak image at q of 20. The far upstream flow was from left to right and the bluff body is also visible in the image. The region enclosed by the bluff body was hashed as this region has high level of noise.
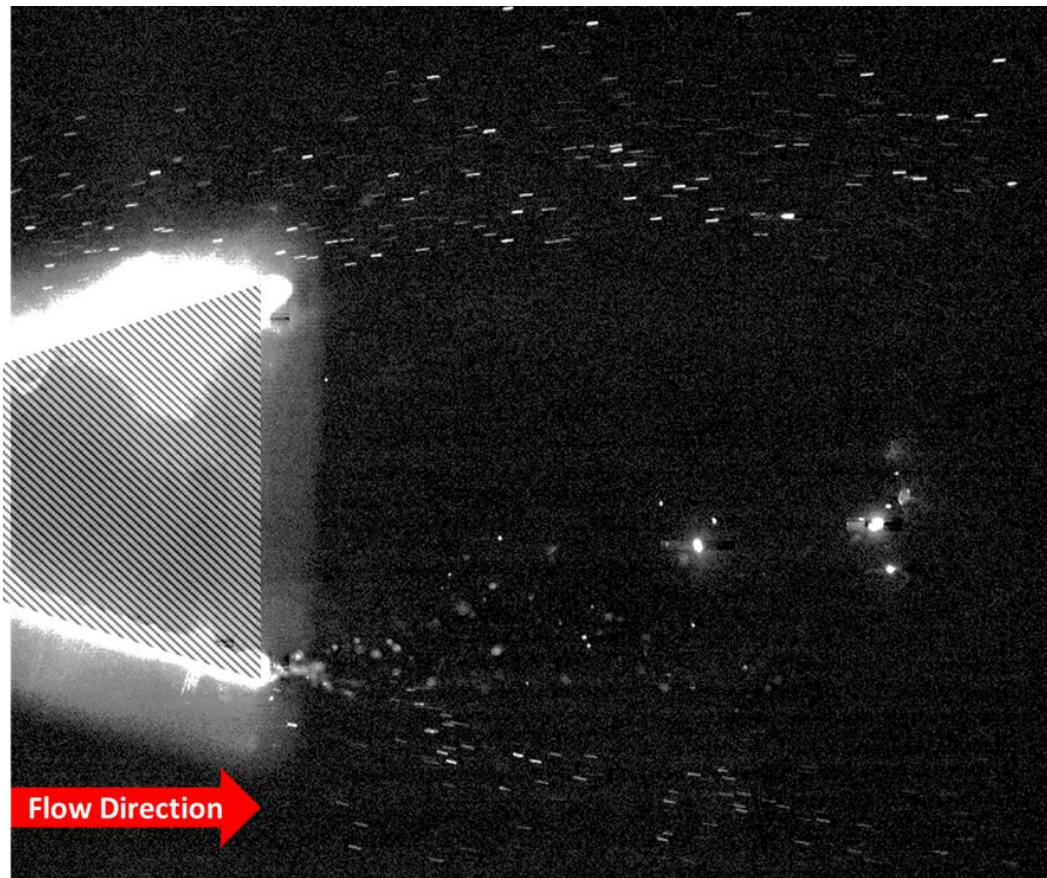
Figure 67: Contrast adjusted streak image outlining flow direction (arrow) and vee-gutter bluff body (hashed lines) (q of 20). The far upstream flow was from left to right.

A large amount of brightness saturation is also noticeable in the general area of the bluff body, primarily as a result of contrast adjustment. This corresponds to accumulation of water on the surface of the bluff body, as well as droplets within the vee-gutter "cavity" (which will be discussed in more detail later). Figures 68a and Figures 68b illustrates differences between streak and non-streak images, which primarily illustrate the appearance of droplets (as streak or particle). Note the increased brightness and reduced visible noise in the streak images. Identical contrast adjustment was performed on both images for viewing purposes. The author also had access to playback of the high-speed recordings which facilitated qualitative analysis.

Figures 68a and Figures 68b are shown the behavior at the momentum flux of 20, however, the qualitative features to be discussed showed no considerable differences at varying momentum flux ratios. That is, the features presented in the following discussion were common across all momentum flux cases with exception of behaviours occurring in the q of 50 and 60 cases related to the boundaries of the bluff body and test section. Given the fixed location of the illumination sheet, the quantity of droplets observed was dependent on the momentum flux, but this will be discussed in the quantitative analysis section.

There are two primary interests concerning the qualitative analysis: overall droplet motion/behaviour and droplet entrainment mechanisms. Droplet entrainment mechanisms were distinguished from overall droplet motion because droplet entrainment was found to occur due to unique mechanisms unrelated to bulk droplet behaviour.
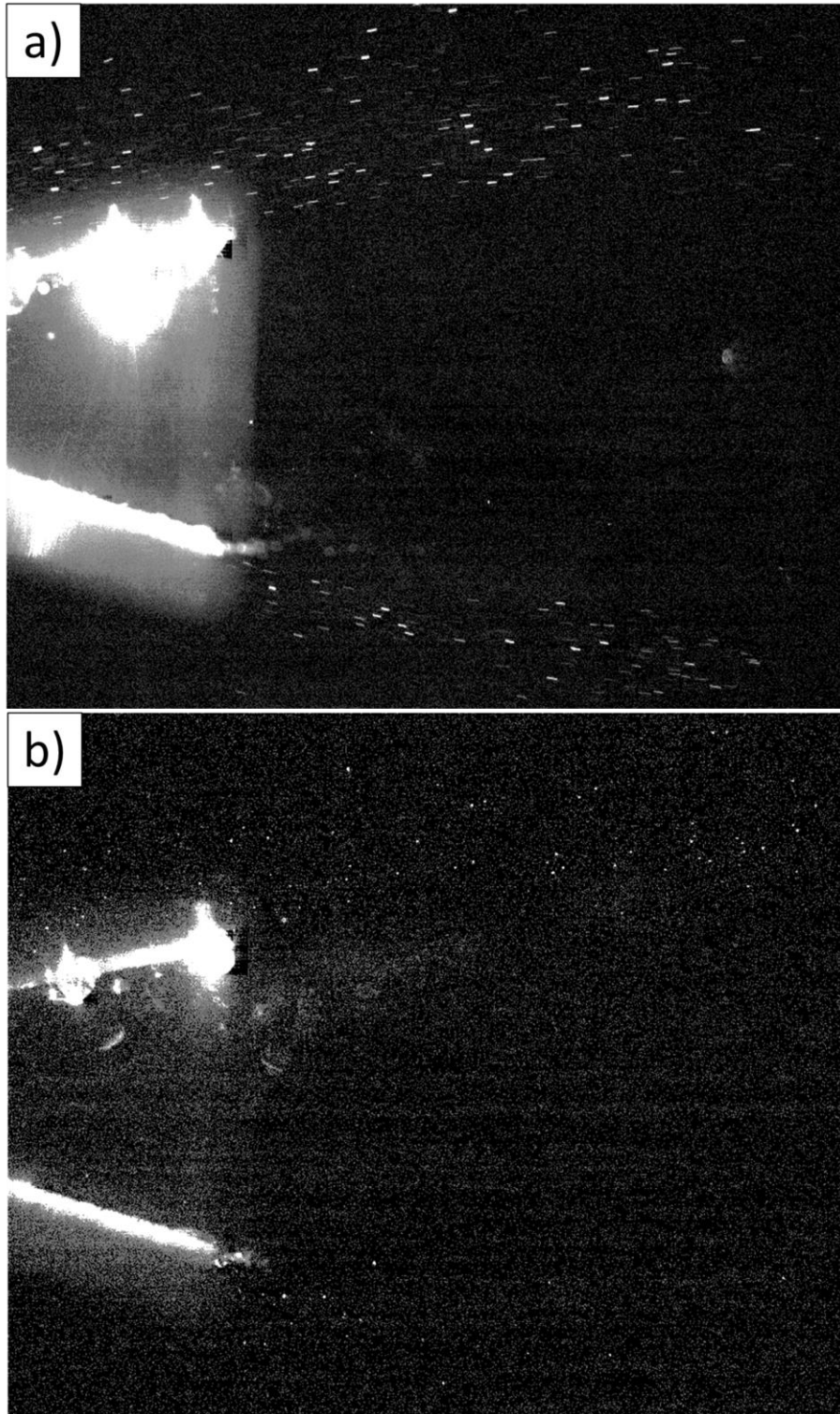
Figures 68: a) Streak (shutter speed 50μs) and b) non-streak (shutter speed 8.26μs) images illustrating appearance of droplets as well as brightness and noise differences (*q* of 20).

4.1.1   Bulk droplet behaviour

Based on the streak images, such as the one in Figure 69, it can be seen that nearly all droplets move along the expected trajectory of gas which flows around both the bluff body and the bluff body wake. The droplets "follow" the gas without deviating from their path to enter the wake region. However, evidently in Figure 69, droplets do exist within the bluff body wake.
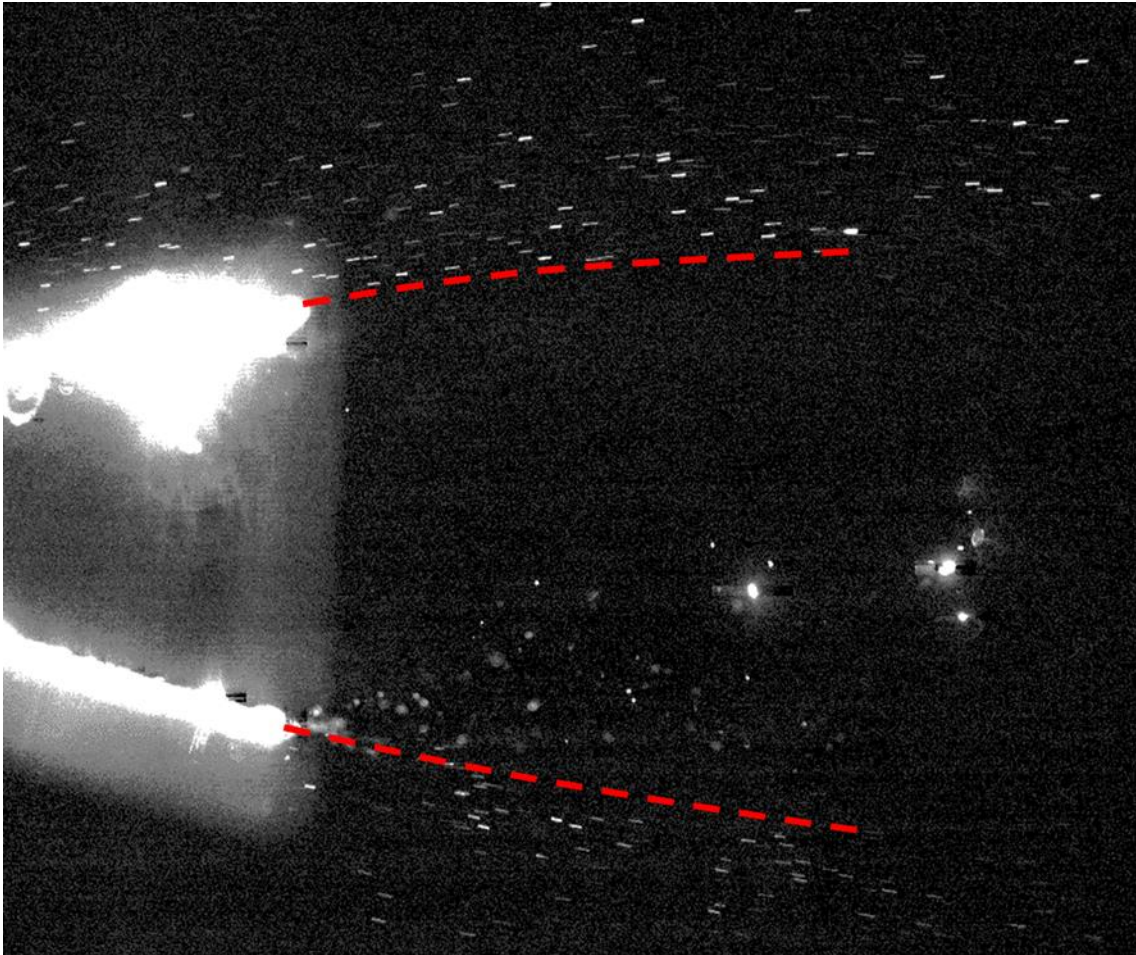
Figure 69: Bulk droplet motion remains outside of the wake region with the shear layers (approximated by the red dashed lines) acting as a barrier.

Before discussing droplet entrainment and behaviour within the wake region, it should be clarified that although the droplets identified in the region adjacent to the bluff body wake may appear organized as if they follow the flow (behave as tracers), it cannot be concluded

that droplet relaxation is occurring without first considering the quantitative data. In fact, given the size of droplets visible at the current image resolution (minimum observable droplet diameter is $\approx 161\,\mu$m), it is expected that droplets visible at this resolution will show some resistance to the inertial effects imposed by the momentum of the gas phase (and thus are not tracers). Instead, since droplet relaxation is a response measured relative to external changes in momentum/inertial forces, the appearance that these droplets follow/mimic the behaviour of the gas phase is presumably a result of low levels of turbulence in the gas phase.

4.1.2   Droplet Entrainment

Observed droplet entrainment mechanisms and behaviour in the wake region of a bluff body was unexpected. With very little exception, droplets in the bulk flow never entrained in the wake region. The primary mechanism by which liquid would find its way into the bluff body cavity and wake was through wetting of the bluff body's windward surface. Any liquid wetted to the surface of the bluff body eventually made its way to the trailing edge (TE) where it would accumulate (see Figure 70).

On the lower TE, the accumulation of liquid ends at the TE. However, on the upper TE, the liquid often continued to cling to the bluff body and creep its way into the bluff body cavity through surface tension. Given the stagnant flow in this region as well as the smooth surface of the acrylic bluff body, liquid was often content remaining in the root of the vee-gutter indefinitely (not shown here). An alternate outcome is that the liquid would instead drip from the top inner surface down to the bottom due to gravity, and eventually end up accumulating at the lower TE. The accumulation of liquid on the lower TE was the primary source of droplet entrainment for all momentum flux ratio cases examined.
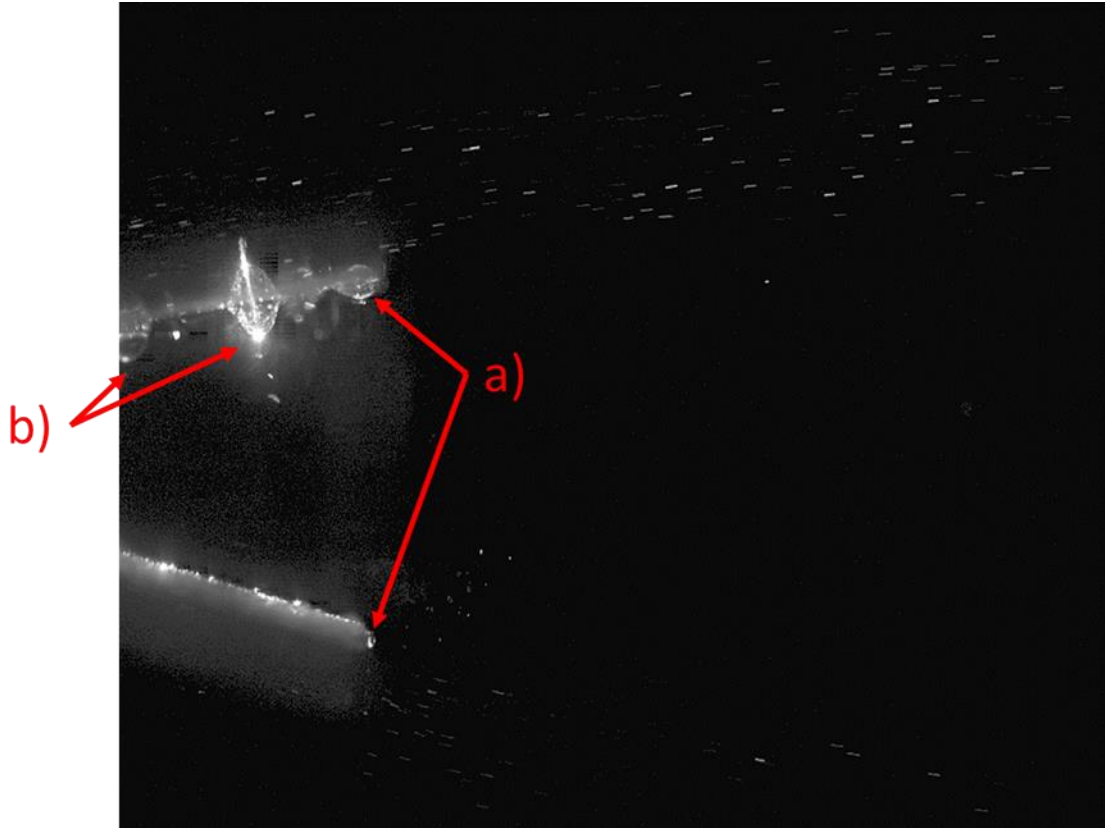
Figure 70: Wetting of the bluff body surfaces results in the accumulation of liquid at (a) the bluff body trailing edge, and (b) accumulations on the upper traling edge often enter the bluff body cavity.

Once a sufficient mass of liquid, too heavy to remain on the inner surface of the lower TE, had accumulated, the liquid would begin to extend into the bluff body's lower shear layer. At this point, the large shear force (strong velocity gradients) between the quiescent wake region and the fast-moving freestream flow would atomize the liquid blobs through familiar breakup process such as ligament and bag breakup (see Figure 71 and Figure 72). A ligament injection process would take place whereby the liquid drop would be stretched into a ligament reaching into the wake region before breaking up into droplets. The turbulent wake structures appear to always pull the ligament (and therefore the resulting droplets) into the wake as opposed to the freestream. As with droplets outside of the bluff body shear layers, these newly formed droplets seemed unable to permeate through the shear layers. These droplets either settled within the wake region or continued to interact with the shear layers leading to their further breakups.

An example of secondary interaction with bluff body wake structures is the bag breakup of droplets within the wake region is illustrated in Figure 72, which highlights the bag breakup of two droplets within the bluff body wake. Depending on the location of these droplets, the resulting droplets may be projected in any direction. It was also apparent that the breakup of these wake droplets occurred due to the shearing effects as the droplets were observed to accelerate during the breakup process. This is evidenced by droplet #2 in Figure 72, as the resulting droplets demonstrate a thin streak-like appearance, which results when a droplet travels a significant distance during the exposure time of the image.

The number of droplets entrained via this mechanism depended largely on the size of the drop accumulating at the lower trailing edge, but this was the dominant entrainment mechanism. Still, a few additional behaviours were observed and deserve mention. First, droplet breakup in upper shear layer occurred infrequently but was always a result of a droplet from the wake transiting into the shear layer from within the wake. Second, the drop accumulating on the upper trailing edge was on one occasion occurred to be broken up by an incoming droplet.
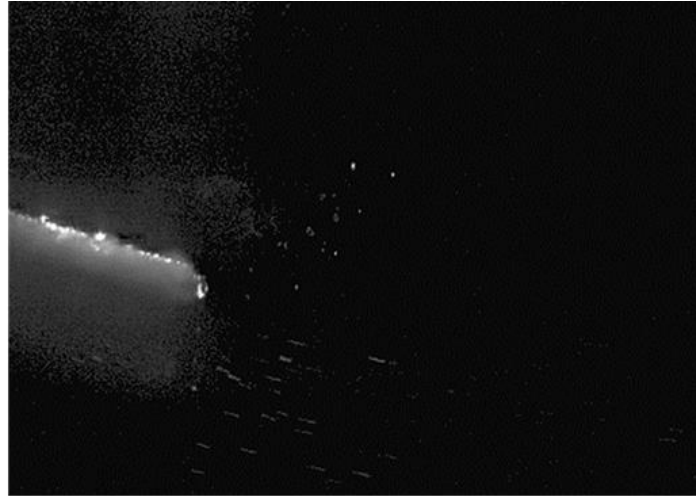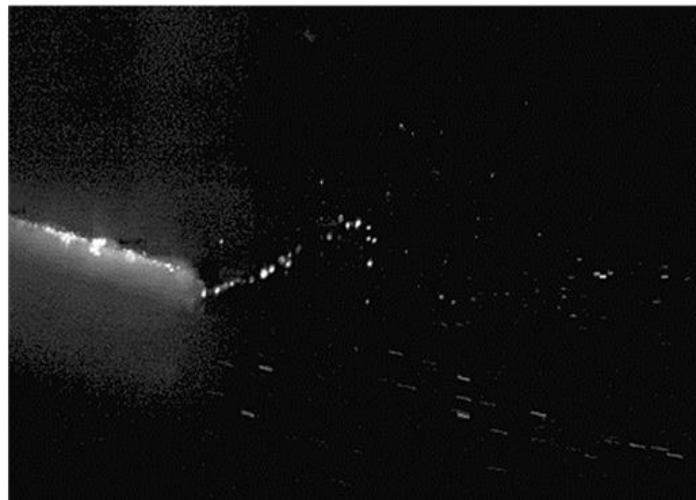
Figure 71: Ligament injection process. (Top) Accumulation of a small water drop on the lower trailing edge. (Middle) Stretching of this drop into a ligament. (Bottom) Subsequent breakup into smaller droplets.
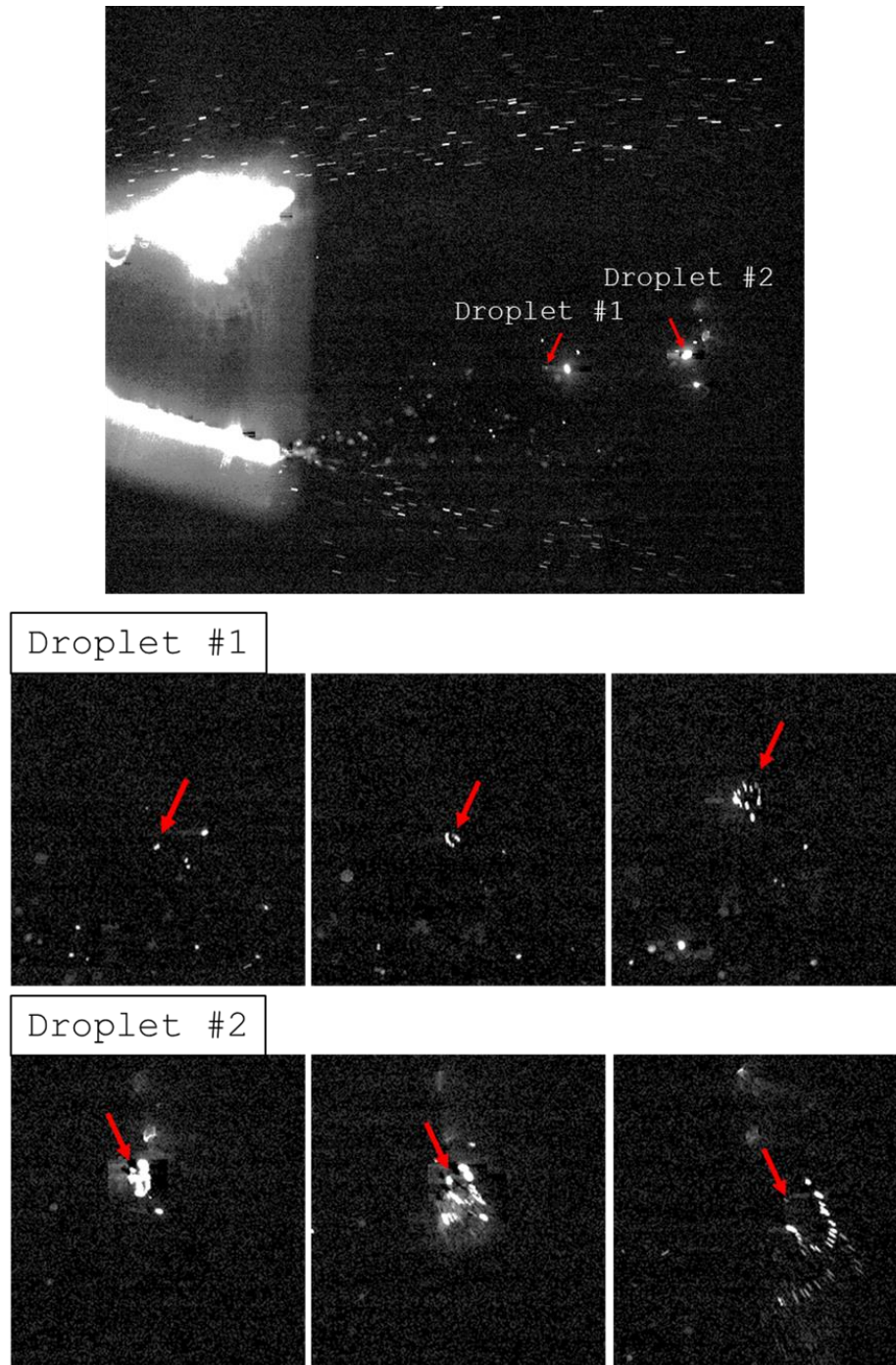
Figure 72: Bag breakup of two droplets of various sizes in the wake region. Droplet #1) Small droplet with breakup projecting droplets upwards. Note that the arrow is pointing to the correct droplet. The larger object to its right was not the object tracked. Droplet #2) Large drop with breakup projecting droplets downwards.

The above qualitative results provide a first insight into the behavior of droplets in the proximity of the bluff body. The results show that the vast majority of droplets travelled in the free-stream region and relatively few droplets entrained into the wake. The results also show that the majority of droplets observed in the wake region are supplied through the secondary process of droplets accumulation on the bluff body and eventual breakdown and entrainment in the wake region. A relatively small fraction of observed wake-region droplets are directly entrained from the free-stream flow. These results indicate a poor liquid-gas pre-mixing (relative to the bluff body), which has a direct impact on the combustion efficiency in the real afterburner as the vee-gutter is used as a flame holder in these applications. It should be noted that in the present study, the size of detected droplets was restricted to 160 μm or higher (due to image resolution). In real applications, the droplet of much smaller sizes are involved in the combustion process. Although the present study is not able to characterize the smaller droplets, considering their smaller size (smaller Stokes number), these smaller droplets are likely to follow the free-stream flow and hence, their chances of entrainment in the wake region are relatively low. Furthermore, in real afterburner applications, the gas velocities are significantly higher than that considered in this study, hence, the chances of droplets entrainment in the wake region further reduces due to the higher gas flow inertia. Thus, it can be concluded that the wake region of the vee-gutter may not provide good gas-liquid mixing, which may have an impact on the combustion efficiency. However, further investigations with higher resolution and more realistic combustion setup are crucial to confirm this conclusion.

4.2   Quantitative Analysis

The quantitative analysis described the sizes of droplets detected using the non-streak images, and the droplet velocities determined using the streak images. For both the droplet sizes and velocities, the global distribution in the freestream region is examined first, followed by the distribution of local mean values.

Droplet behaviour was examined in three regions: the upper freestream region, the lower freestream region, and the wake region (*see* Experimental Setup and Methods). The freestream region was split into upper and lower zones to examine any asymmetric

behaviour about the bluff body. It was intended to examine the wake region downstream of the bluff body's trailing edge, however a few concerns led to the omission of this data.

For the non-streak images, although droplets could be identified within the wake region, image artifacts were found in that region that indicate that the current droplet detection method may occasionally take multiple measurement of the same droplet due to the lower droplet speeds in this area. In addition, image artifacts such as flaring occasionally resulted in artificial droplets, which over time create artificial concentrations at these flare locations. Figure 73 shows some examples of these artifacts.
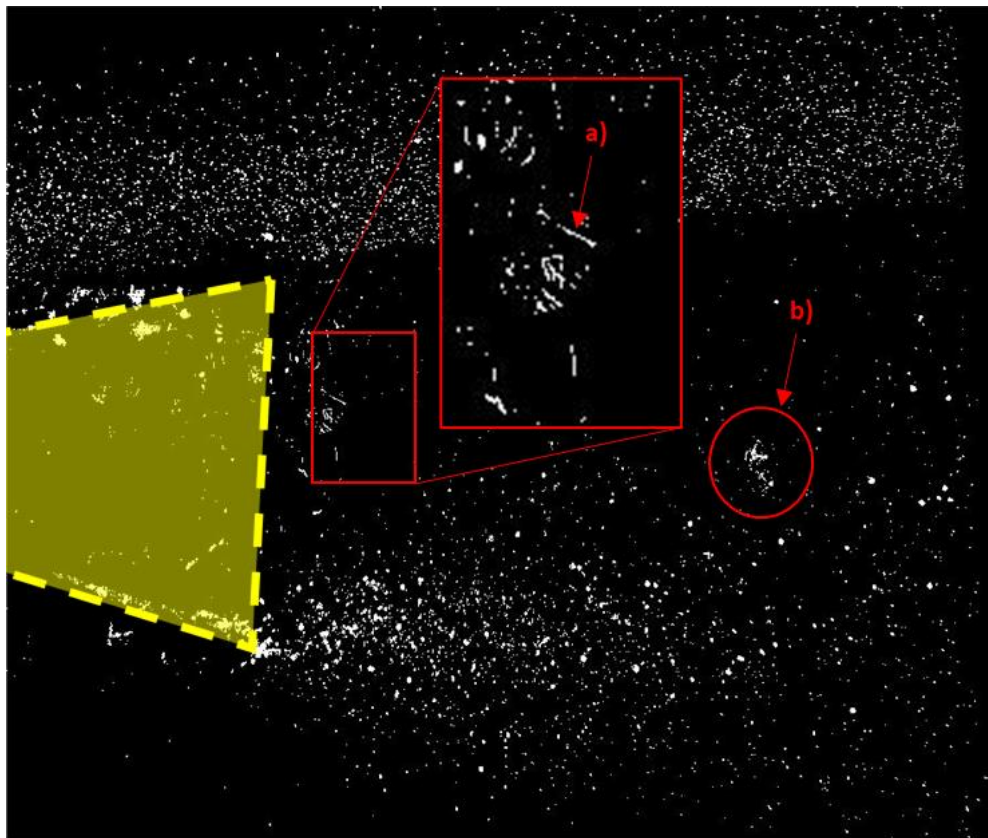
Figure 73: Short exposure image (*q* of 20) created from a logical 'or' combination of all detected binary droplets. Object (a) represents a streak created by a single droplet moving slowly, and region (b) represent flaring from droplet reflections. The bluff body is outlined on the left in yellow.

For the streak images, artifacts could more easily be removed as they would appear larger and brighter due to the longer image exposure time, however some artifacts were present in the wake region only (see Figure 74). This was not a concern as the wake region did not contain droplet streaks and thus there was no information available in the wake.
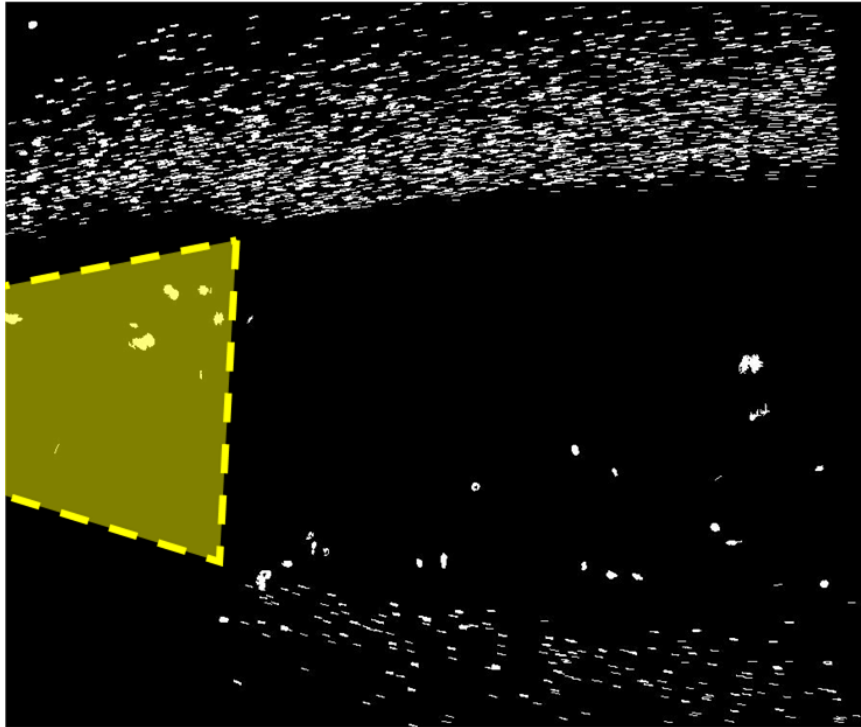
Figure 74: Long exposure image (q of 20) created from a logical 'or' combination of all detected streaks. Observe that the only artifacts (large non-streak objects) appear in the wake region. The bluff body is outlined in yellow on the left.

4.2.1   Droplet Size

The detectable droplet sizes were limited to the resolution of the image, and although they do not cover the entire desirable range, these results provide a good firsthand approximation of the overall droplet dynamics and also illustrate the capabilities of the experimental methodology. In addition to large droplet sizes, the resolution of discretization is also quite large as a result of the image resolution. The PDF in Figure 75 shows the size distribution of the droplets detected in the freestream region based on calculated equivalent diameter.
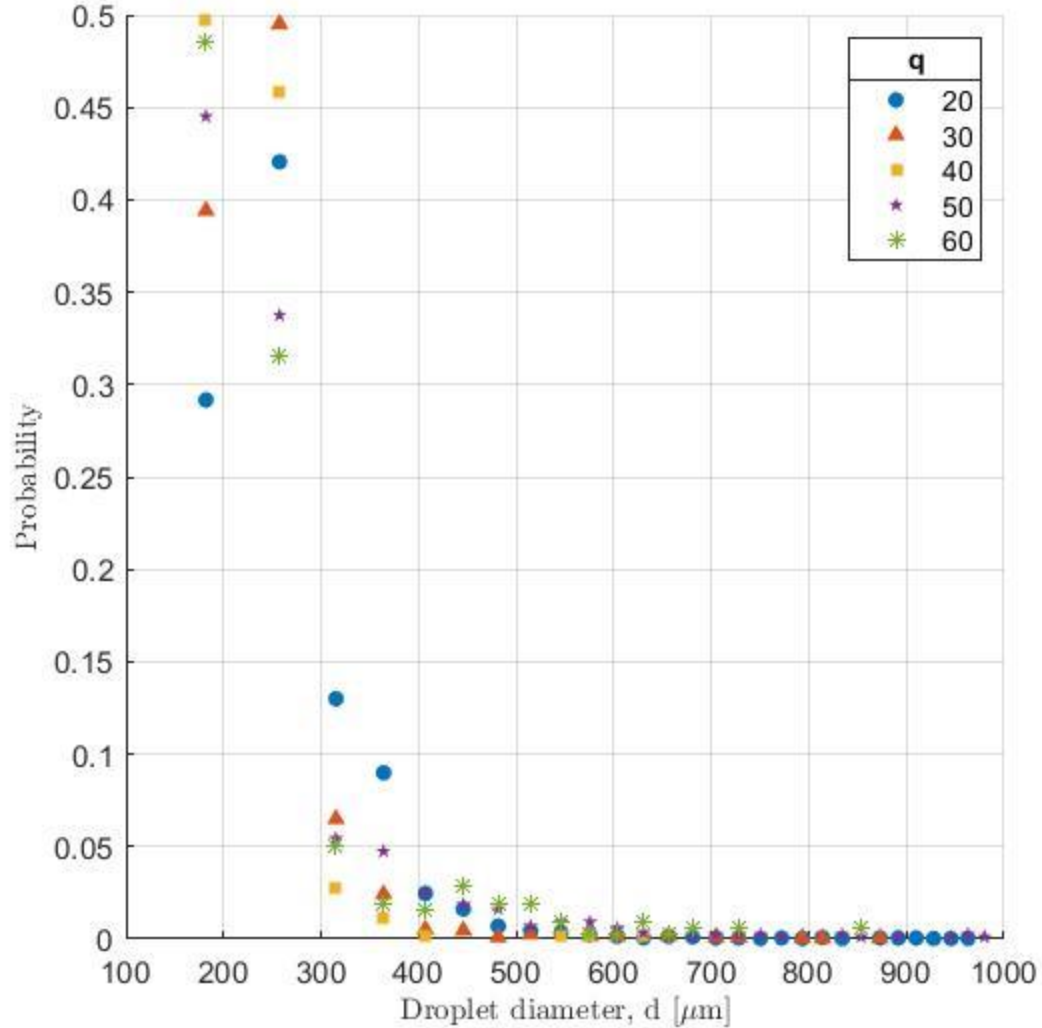
Figure 75: PDF of droplet diameter for the combined upper and lower freestream regions for q=20, 30, 40, 50, and 60.

The droplet sizes were found to be highly concentrated at the two smallest sizes, 182µm and 257µm, which comprise 71% (q of 20) to 95% (q of 40) of the total droplet count. As q increases, the concentration of 182µm droplets increases, with q of 40 having a relatively even split of 182µm and 257µm diameters. The increased percentage of smaller droplets may indicate that larger q results in smaller droplet sizes overall, and/or that shearing mechanisms from the liquid jet column produces smaller droplets than those which exist

in the droplet plume. The plume is defined as the volumetric region in which the droplets are primarily found.

The total number of detected droplets decreased with increasing momentum flux ratio, with the slight exception of q of 50, as shown in Table 2. As mentioned in the methods chapter, the placement of the laser sheet was chosen to remain in a fixed location ($\frac{y}{d} = 70$) which was optimized for viewing droplets at q of 20 as it corresponded with the region of the spray plume most congruent with the freestream flow. As a result, for higher momentum flux ratios, this location corresponds with shearing of droplets from the jet column, which would be expected to produce less droplets at the current Weber number.

Table 2: Total droplet counts in the upper and lower freestream regions

		Upper	Lower	Total
	20	2895 (81%)	674 (19%)	3569
	30	1692 (87%)	249 (13%)	1941
Momentum flux, q	40	696 (92%)	64 (8%)	760
	50	359 (42%)	506 (58%)	865
	60	167 (53%)	150 (47%)	317

Note in Table 2 that the quantity of droplets in the lower freestream region relative to the total number of detected droplets also generally increases with q. The change is quite abrupt, with the lower freestream region containing <20% of total droplets from q of 20 to 40, but 50% or more of total droplets at $q{\geq}50$. Increased mass flow of liquid leads to increased incidence of ligament injection events at the lower trailing edge, ultimately resulting in higher droplet counts after secondary atomization processes occur. This shows that the ligament injection behaviour creates a difference in liquid-gas ratios between the upper and lower trailing edges, and that this difference is dependent on the liquid flow rate.

Figure 76 illustrates the composition of droplet sizes specifically for the lower freestream region from q of 20 to 60. It is clear that droplets at 182μm and 257μm diameters comprise the majority of the droplets in this region with 40% to 47%, and 23% to 39% shares, respectively. The distribution trends for the upper freestream region were identical to that

of the combined upper and lower freestream regions. That is, the 182μm and 257μm droplets comprise 71% (*q* of 20) to 95% (*q* of 40) of the total droplets in this region.
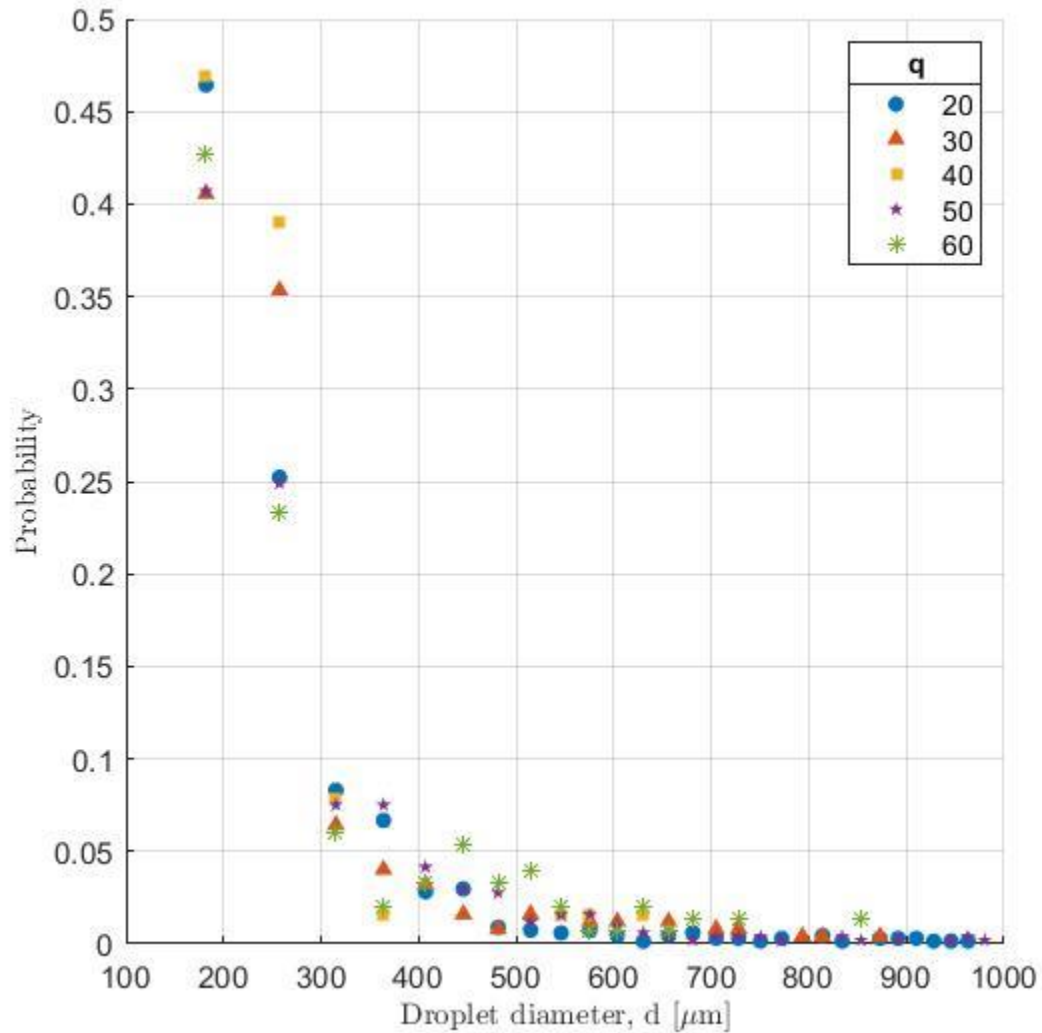
Figure 76: PDF of droplet size in the lower freestream region for q=20, 30, 40, 50, and 60.

Figure 77 provides a glance at the spatial distribution of droplet sizes for *q* of 40 and *q* of 60 cases. The data in the wake region is excluded due to the presence of image artifacts. The droplet sizes illustrated here are in reference to the Sauter mean diameter (SMD) determined for each 32×32 bin region. Note that there are many empty regions, which is

an indication that no droplets were detected in this reason and signifies the need for a larger number of samples needs to be acquired to accurately quantify droplet sizes.
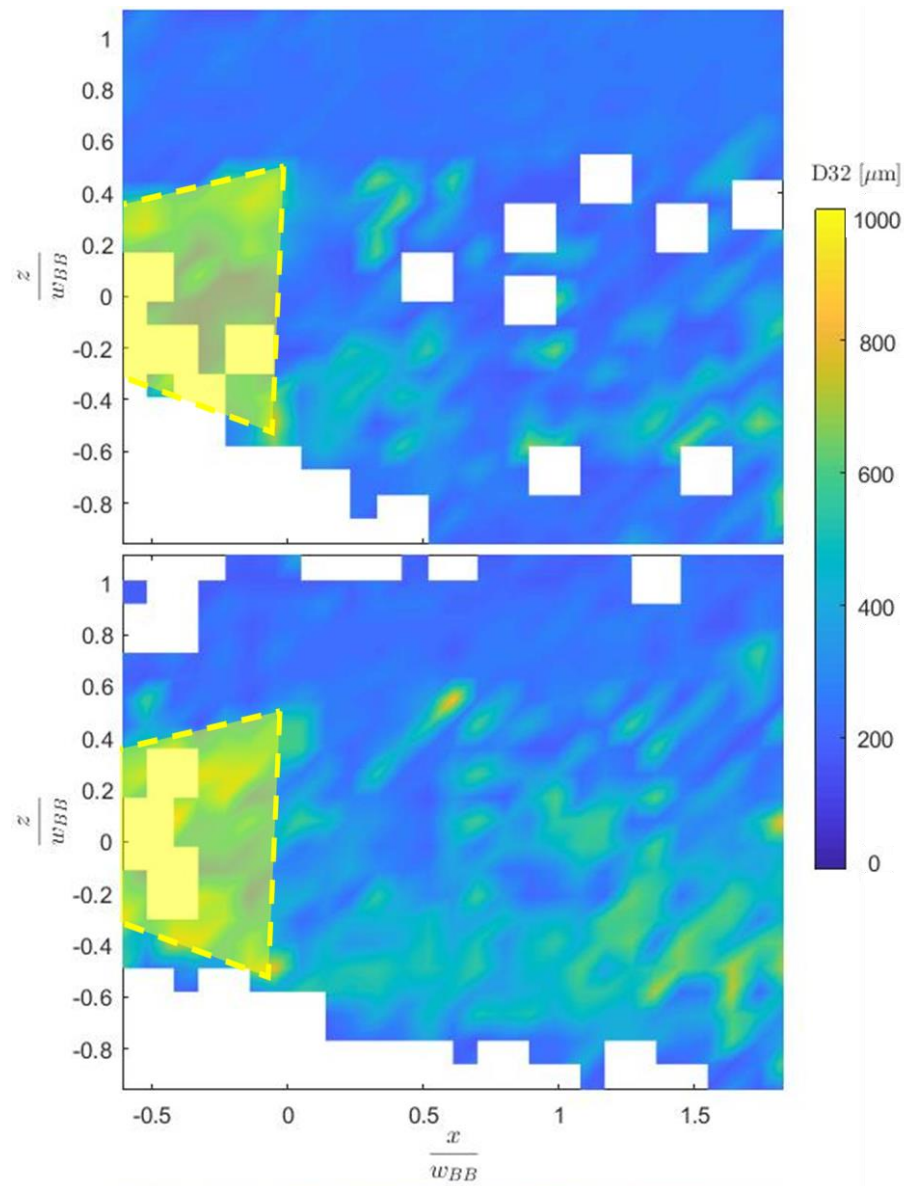
Figure 77: Spatial distribution of SMD for *q* of 40 (top) and *q* of 60 (bottom). The empty (white) regions contained no data, and the bluff body is outlined in yellow.

In Figure 77 (above), the SMD distribution is uniform in the freestream region above the bluff body and is more varied in the lower freestream region. The uniformity in SMD is also evident in Figure 78 which shows that for *q* of 50, the SMD is not a strong function of

downstream distance in the freestream region. This trend was consistent for all momentum flux ratios.
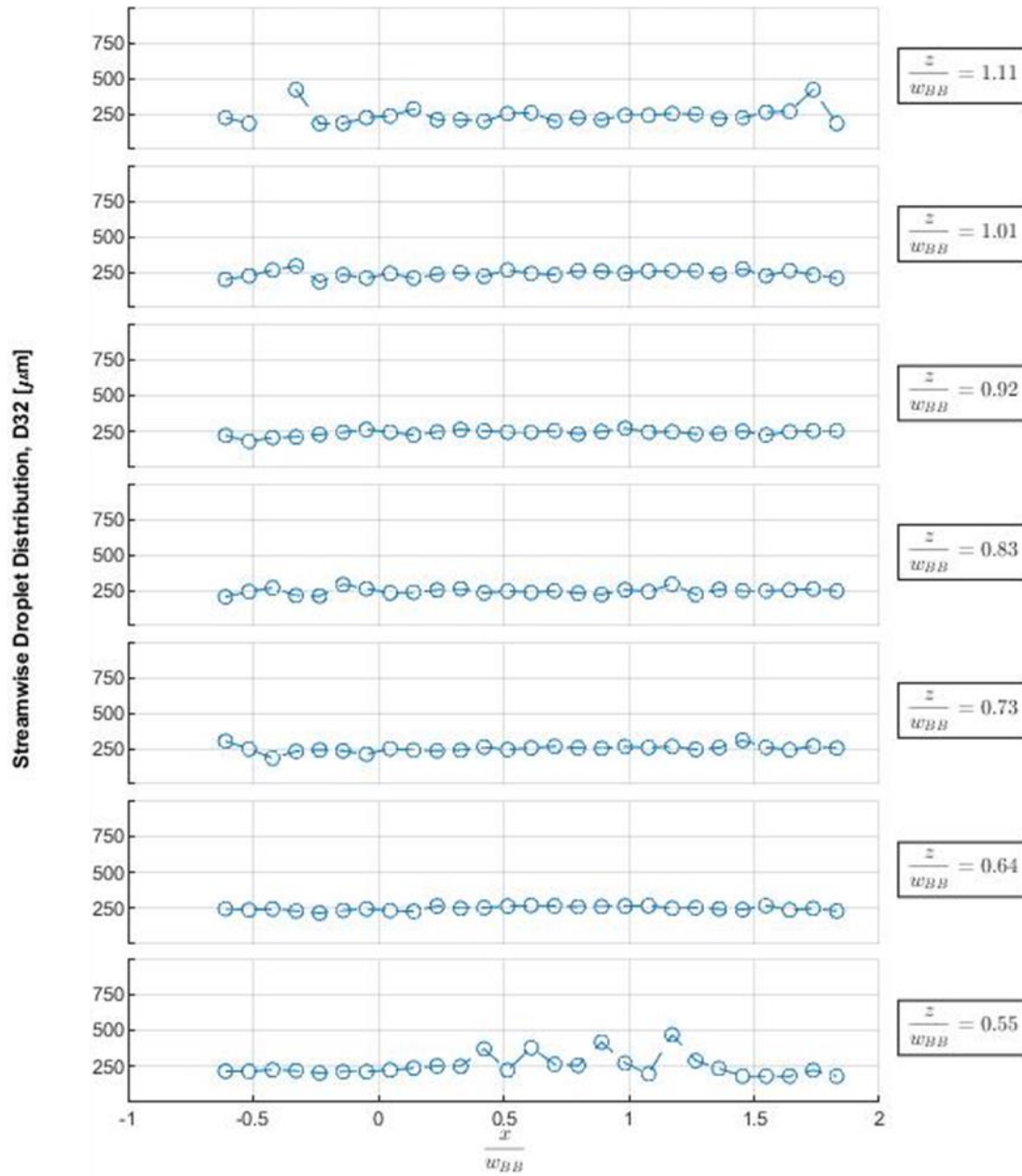
Figure 78: Streamwise SMD distribution in the upper freestream region at various spanwise locations (*q* of 50).

4.2.2   Droplet Velocity

The PDFs of velocity magnitudes for detected droplets using the streak images are shown in Figure 79 for q of 20 case. As with the non-streak images, the combined freestream regions and the upper freestream region show identical trends, which is that the calculated velocities are clustered at discrete values. The analysis of the long-exposure images (see an example in Figure 79), show that the streaks in the free-stream region of images are not affected by image artifacts, hence, the velocity results presented in the above figure are accurate. These discrete values occur within the bins: 20-21m/s, 23-24 m/s, 26-27 m/s, and 29-30 m/s, which contain nearly 2/3 of the total counts, 63.2% and 64.4% for the combined and upper freestream regions, respectively. This is different from the lower freestream region where 63.6% of velocities fell within 19 to 24 m/s. As with droplet size, the number of detected droplets decreased with momentum flux ratio (Table 3). Hence, the results in the lower free-stream region for cases q of 40 to 60 are not statistically significant.

Table 3: Total streak counts in the upper and lower freestream regions

		Upper	*Lower*	*Total*
	20	1813 (95%)	88 (5%)	1901
	30	1007 (95%)	51 (5%)	1058
Momentum flux, q	**40**	328 (96%)	15 (4%)	343
	50	101 (89%)	13 (11%)	114
	60	57 (90%)	6 (10%)	63
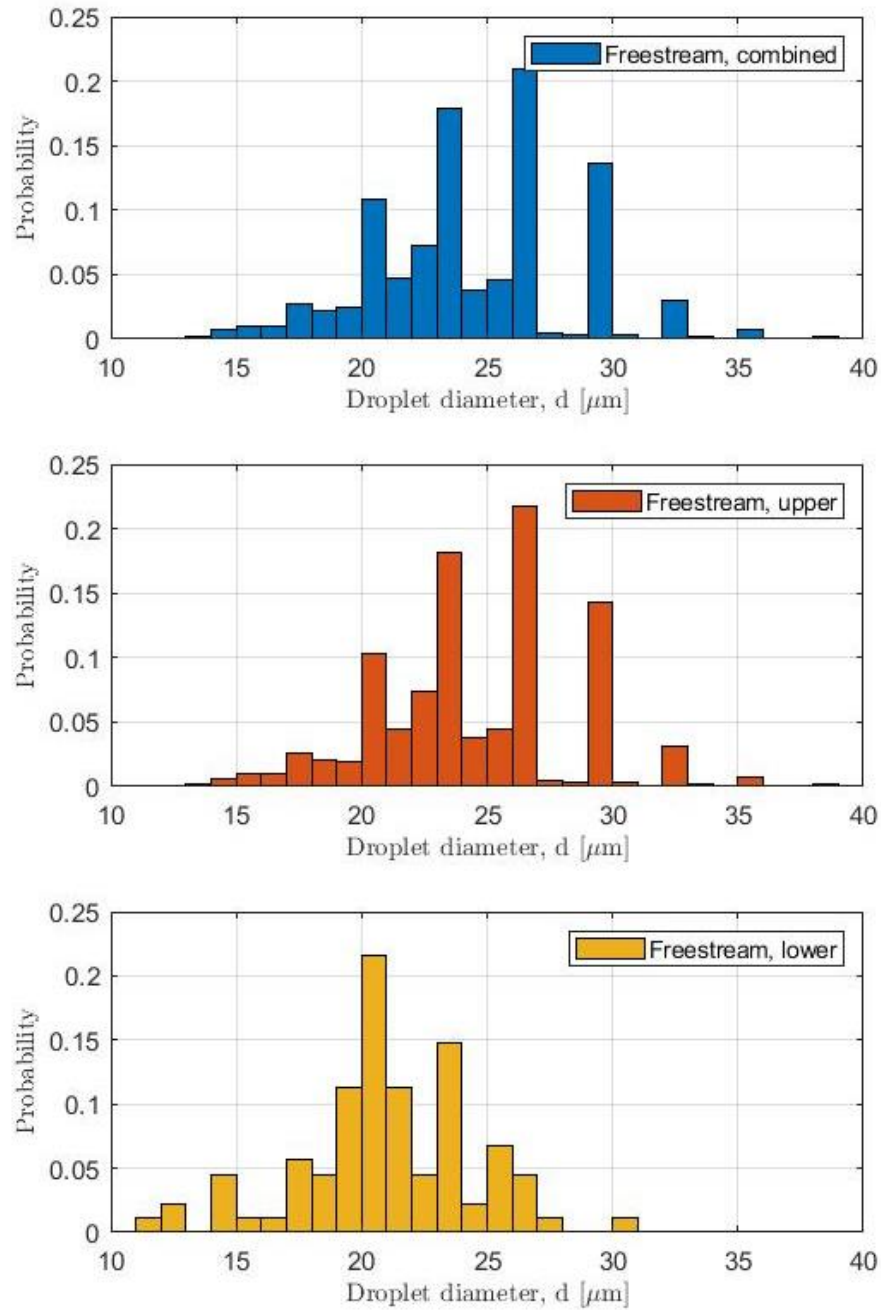
Figure 79: PDFs of the droplet velocity magnitudes for q=20 in the combined freestream regions (top), upper freestream region (middle), and lower freestream regions (bottom).

Possible reasons for drastically reduced streak/droplet count as compared to the non-streak images include the lack of wake streaks present and out of plane motion of many droplets which would not result in streak formation. In addition, due to the increased exposure and therefore brightness of the streak images, a more conservative detection method was applied to avoid detection of false objects such as flaring objects, resulting in the removal of a larger number of detected objects overall.

Figure 80 shows the color maps of the spatial distribution of droplet resultant velocity magnitudes for q of 20 and q of 50. There is an evident increase in droplet speed with downstream distance, which is expected. There is also a noticeable lack of data in the wake region, which is expected due to the lack of streak formation in that region as discussed earlier.

The increase in droplet velocity is proposed to be a result of gas acceleration around the bluff body (flow convergence). As the freestream air accelerates past the bluff body, the droplets must also accelerate, but due to their size they lag the flow. In the current field of view, it does not appear that droplets become fully relaxed (i.e., $v_{drop} \neq v_{air}$). Figure 81 illustrates that the droplet velocity increases as a function of downstream distance at various spanwise locations throughout the freestream region. This is consistent across all momentum flow ratio cases.
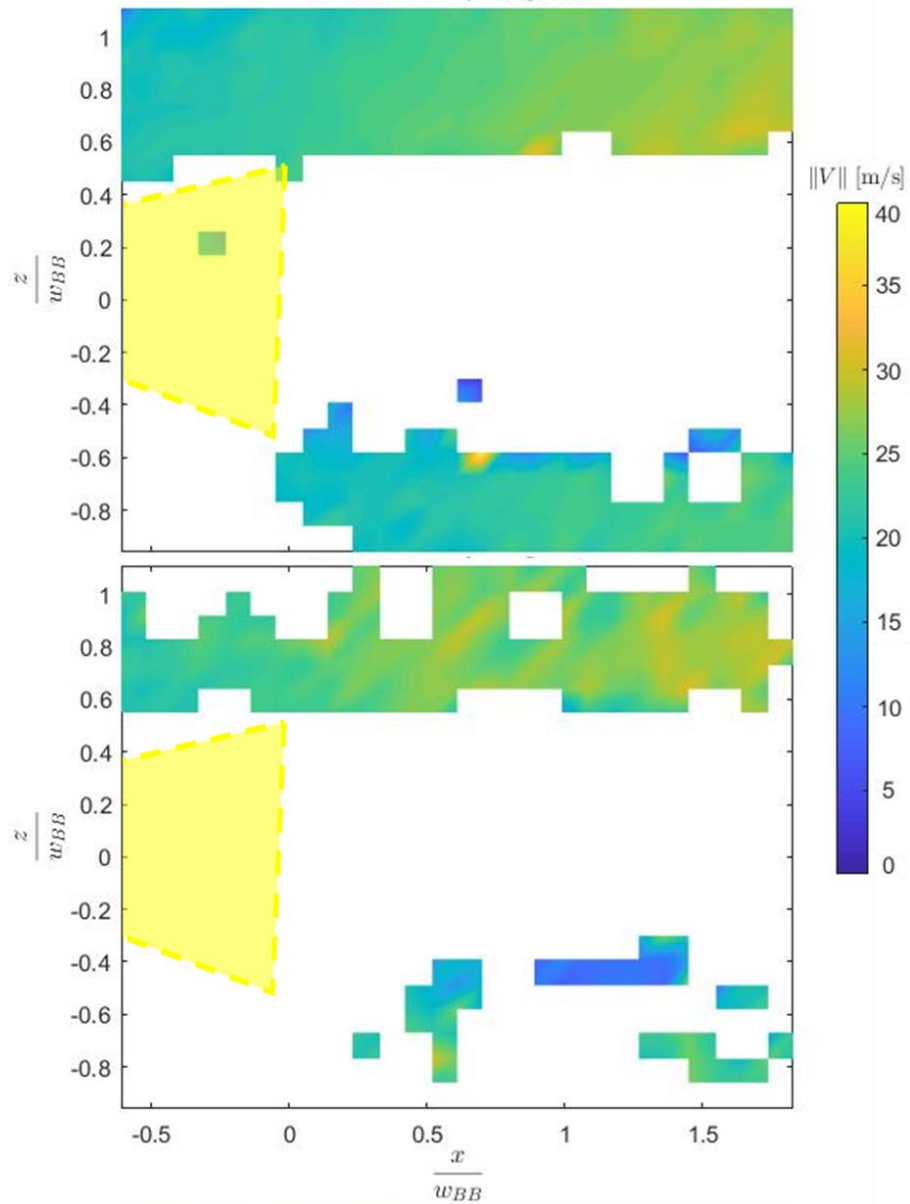
Figure 80: Spatial distribution of streak velocity magnitudes for _q_ of 20 (top) and _q_ of 50 (bottom). The empty (white) regions contained no data, and the bluff body is outlined in yellow.
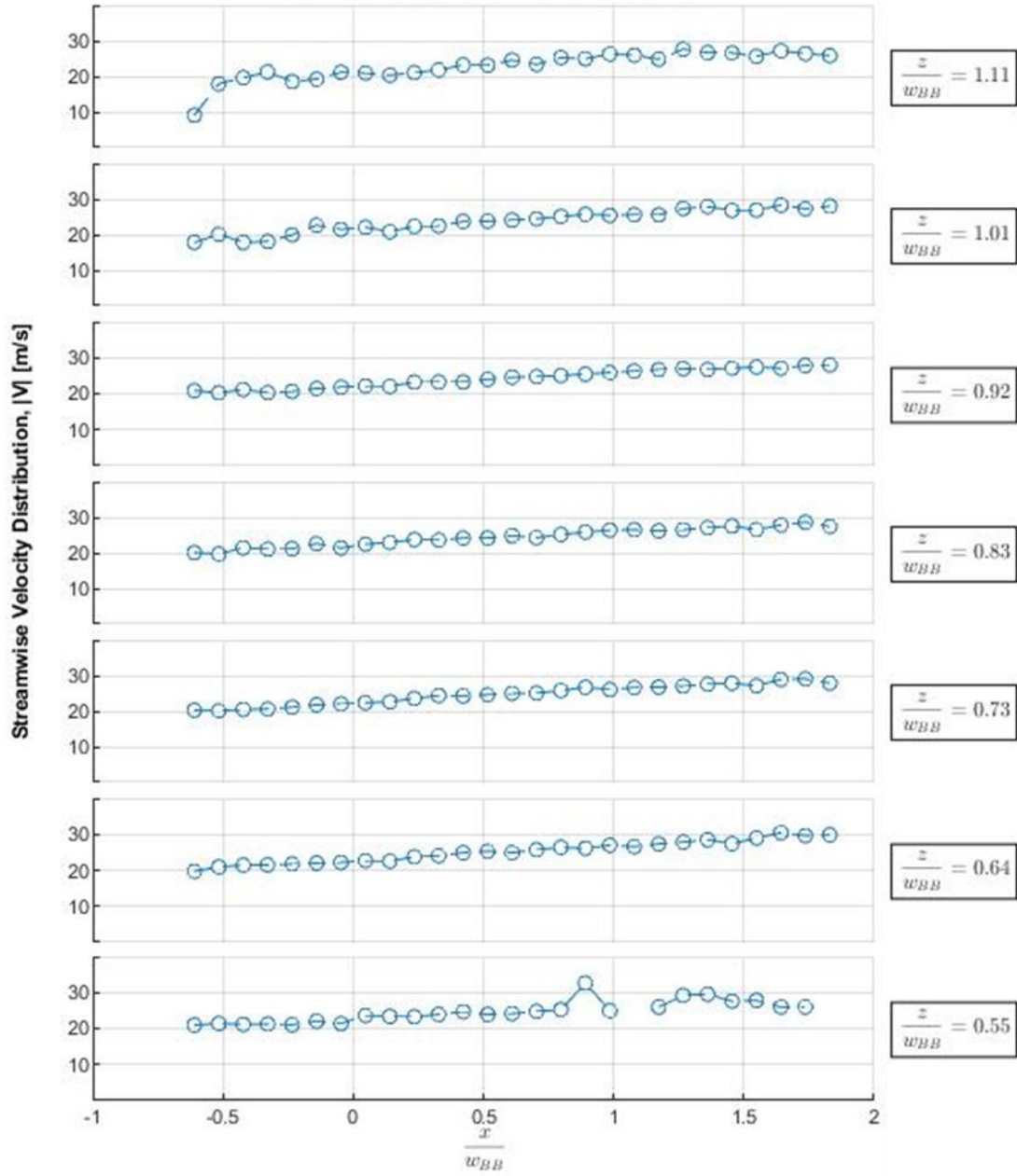
Figure 81: Streamwise streak velocity distribution in the upper freestream region at various spanwise locations (*q* of 20).

Chapter 5

5 Conclusion

In gas turbine engine afterburners jet-in-crossflow fuel injection is utilized to provide fuel for combustion. This injection system creates a spray of fuel droplets which flow through the afterburner pipe and around a bluff body flameholder where it reacts in combustion. The fuel dynamics within the afterburner are a variable which participates in combustion instability which can be harmful and dangerous to the engine. While the influence of bulk and mean gas flow on spray behaviour is known, the impact of turbulence has yet to be explored in detail. In order to better understand the jet-in-crossflow injection process, the objective of this thesis was to investigate the droplet dynamics in an afterburner-like flow configuration. Particularly this thesis looks to identify relationships between turbulent flow properties and droplet size and distribution.

The thesis research consisted of a two-part experiment aimed at elucidating spray droplet dynamics related to afterburner combustion. Modifications were made to existing wind tunnel facilities in order to simulate afterburner flow. Particle image velocimetry and high-speed imaging were used to capture the behaviour of the jet-in-crossflow dynamics and the resulting images were processed using in-house MATLAB codes. A jet-in-counterflow configuration was also investigated due to interest from the project sponsor. The PIV methodologies were only applied to the jet-in-crossflow and jet-in-counterflow spray characterization, while the investigation of droplet behaviour around a bluff body was performed with high-speed imaging techniques, due to malfunctioning PIV equipment. All studies were performed at a fixed gas crossflow velocity, but at different liquid injection flow rates.

Part one of this thesis study was conducted to simultaneously establish a baseline of droplet and gas characteristics found in jet-in-crossflow and jet-in-counterflow spray injection configurations. PIV data was processed to identify turbulent and mean flow properties of the gas around and within a plume of spray droplets. The droplets were also analysed, and size and spatial distribution of these droplets was investigated. Using both the turbulent

description of the gas flow and the spatial distribution of droplet sizes, the interaction and correlations between turbulence and droplet size was studied.

Droplet measurements for the jet-in-crossflow spray served to some degree as validation for the experimental methods, as the droplet sizes were found to be comfortably within 30μm and to 250μm range and larger droplets were found to penetrate further into the gas crossflow, as described in the literature. After investigating the gas flow, it was found that the spray plume was characterised by a region of retarded mean flow in the bulk of the spray and was bounded upstream by a strongly turbulent and localized shear layer and bounded downstream by less turbulent, more expansive region. Spatial correlation between turbulent flow properties and droplet size suggest that droplet breakup primarily occurs in the strongly turbulent shear layer. The correlations were found to be much stronger at higher momentum flux ratios (q of 60 and 120).

For the liquid jet-in-counterflow configuration, spray droplets were overall found to be larger than their jet-in-crossflow counterparts for the same momentum flux ratio. Some similarity was found in that the largest droplets were found in the spray periphery. However, due to a lack of literature specifically relating to liquid jet in gas counterflow sprays, deviations from expected droplet sizes could not be discussed. In regard to gas flow, the spray region was defined by uniform distribution of turbulence in the spanwise direction, changing very little with downstream distance, and having low levels of turbulence at the shear layer between the droplet plume and the freestream gas. Although high levels of turbulence were seen near the spray bar for low q flow (q of 10), turbulence was seen to diffuse with downstream distance, therefore it is suspected that the bulk of turbulence generated for flows with a larger q was not captured as it occurred upstream outside of the field of view. No significant spatial correlations were found between mean or turbulent gas flow and droplet size.

In the second part of this thesis study, the flow of JIX droplets around a bluff body was investigated using high-speed imaging techniques. Two different recordings, one with a short exposure time and one with a long exposure time, were taken at each momentum flux ratio investigated. The shorter exposure time allowed for the characterization of droplet

size, spatial distribution, and breakup behaviour, while the longer exposure time allowed for estimation of droplet velocity.

Qualitative examination of the high-speed images revealed that the droplets passing around the bluff body were unlikely to pass from the freestream into the bluff body wake region. The droplets passing over the bluff body are suspected to have too much momentum to be considerable influenced by the turbulent bluff body wake and therefore did not deviate from their course. However, this did not result in zero droplets in the wake region. The mechanism by which droplets were capable of entering the wake region was not related to droplet advection or turbulent mixing of the flow. Liquid accumulation on the surface of the bluff body was capable of reaching the trailing edge of the bluff body and trickling into the bluff body cavity. From here, drops would form on the trailing edge and when the drop interacted with any gas turbulence, classical liquid breakup processes were observed. These processes include ligament and bag breakup and they resulted in the injection of droplets into the wake region. Once in the wake region, turbulence and velocity gradients dictated the motion and behaviour of droplets. This behaviour was qualitatively observed to occur more often at higher liquid flow rates.

Droplet size and velocity magnitudes were evaluated qualitatively using similar image processing methods to the free spray portion of the study. Only droplets in the freestream (outside of the bluff body wake) were included in the analysis due to artifacts and low droplet counts in the wake region. Most droplets detected were found to be less than 300µm in size and the flows with a larger momentum flux ratios of q of 50 and 60 demonstrated a larger proportion of small droplets (<200µm). At the lowest flux ratio for q of 20, the droplets were overall larger compared to the other flow cases. It was also found that the number of droplets detected in the region below the bluff body increased significantly (~10% to >50%) when ligament injection processes were frequent. The size distribution of droplets specifically in the lower region showed a larger proportion of small droplets (<200µm) for all momentum flux ratios. The spatial distribution of droplet sizes was very uniform, indicating that droplet size and location were not correlated within the freestream (excluding the differences between lower and upper freestream regions due to ligament injection). While this experiment found little droplet activity in the recirculation zone

behind a vee-gutter bluff body, it is known that bluff body combustion is possible due to recirculation of fuel droplets in a bluff body wake. The current study did not examine droplet behaviour at the end of the bluff body's recirculation zone.

Finally, the velocity magnitudes overall appeared to be slower than the expected freestream velocity, although the freestream gas velocity around the bluff body was not measured due to PIV equipment malfunction.

5.1   Future Directions

The current thesis work is novel in its simultaneous investigation of turbulent flow properties and droplet distribution for jet-in-crossflow sprays. There is also novelty in the investigation of droplet distribution around a bluff body. However, the existing work can be expanded upon and greatly improved.

A large time commitment was required in order to develop the new experimental facilities required to perform this kind of spray research at high velocities in the wind tunnel Western University Faculty of Engineering's Gas Dynamics lab. A new contraction was designed which can allow the flow to be accelerated near Mach 0.5, however a new fan motor (and maybe fan) is required to accelerate the flow. In addition, the PIV investigation of the bluff body work should be performed when the equipment becomes available.

The image processing methodology for droplet detection also needs to be re-examined and refined. Currently there remains uncertainty in the quantification of droplet size as well as in the ability of any software to detect objects on the order of a few pixels. It would be possible to narrow the field of view and get a better image resolution, however this would render the PIV analysis more difficult and so other methods of identifying droplets needs to be investigated. The identification of two separate phases within a flow is not a novel premise, and research into existing methodologies may prove fruitful.

Finally, concerning the application of the results to the issue of combustion instability, more detailed analysis of the flow turbulence and the droplet motions need to be investigated. With accurate characterization of droplet motion and the interaction with

turbulence, it may become easier to predict and control the relationship between velocity fluctuations in the afterburner combustion chamber and the fluctuations in heat release caused by the periodic supply of fuel droplets.

References

[1]   C. Keller, "Forty years of experience on closed-cycle gas turbines," *Annals of Nuclear Energy*, vol. 5, no. 8–10, pp. 405–422, Jan. 1978

[2]   E. E. Zukoski, "Ch 21 - Afterburners," in *The Aerothermodynamics of Aircraft Gas Turbine Engines*, G. C. Oates, Air Force Aero Propulsion Laboratory, 1978

[3]   J. Lovett, T. Brogan, D. Philippona, B. Kiel, and T. Thompson, "Development Needs for Advanced Afterburner Designs," in *Joint Propulsion Conference and Exhibit,* AIAA 2004, Fort Lauderdale, FL, USA, July 11-14, 2004

[4]   MTU Aero Engines AG, "EJ200 turbofan engine - The innovative power.", MTU_Prod_EJ200_2018_01, March 2018

[5]   L. Rayleigh, "The Explanation of Certain Acoustical Phenomena," *Nature*, vol. 18, no. 455, pp. 319–321, Jul. 1878

[6]   J. W. Strutt, *The theory of sound vol. 2*, Cambridge: Cambridge University Press, 2011.

[7]   B. T. Chu, "On the energy transfer to small disturbances in fluid flow (Part I)," *Acta Mechanica*, vol. 1, no. 3, pp. 215–234, 1965

[8]   F. Nicoud and T. Poinsot, "Thermoacoustic instabilities: Should the Rayleigh criterion be extended to include entropy changes?," *Combustion and Flame*, vol. 142, no. 1–2, pp. 153–159, 2005,

[9]   J. O'Connor, V. Acharya, and T. Lieuwen, "Transverse combustion instabilities: Acoustic, fluid mechanic, and flame processes," *Progress in Energy and Combustion Science*, vol. 49, pp. 1-39, 2015

[10]   J. W. Useller, J. L. Harp Jr., and Z. Barson, "Altitude Performance of Annular Combustor Type Turbojet Engine with JFC-2 Fuel," Lewis Flight Propulsion Laboratory, Cleveland, Ohio, NACA RM E51J26, 1952.

[11]   S. Candel, "Combustion dynamics and control: Progress and challenges," *Proceedings of the Combustion Institute*, vol. 29, no. 1, pp. 1–28, Jan. 2002,

[12]   T. Poinsot, "Prediction and control of combustion instabilities in real engines," *Proceedings of the Combustion Institute,* vol. 36, no. 1, pp. 1–28, Jan. 2017,

[13]   J. A. Lovett et al., "On the Influence of Fuel Distribution on the Flame Structure of Bluff-Body Stabilized Flames," *Journal of Engineering for Gas Turbines and Power*, vol. 136, no. 4, April 2014,

[14]   J. A. Lovett, C. Cross, E. Lubarsky, and B. T. Zinn, *A Review of Mechanisms Controlling Bluff-Body Stabilized Flames With Closely-Coupled Fuel Injection*, GT2011-46676, Proceedings of ASME Turbo Expo, June 6-10, 2011, Vancouver, BC, Canada

[15]   S. J. Shanbhogue, S. Husain, and T. Lieuwen, "Lean blowoff of bluff body stabilized flames: Scaling and dynamics," *Progress in Energy and Combustion Science*, vol. 35, no. 1, pp. 98–120, Feb. 2009

[16]   J. P. Longwell, E. E. Frost, and M. A. Weiss, "Flame Stability in Bluff Body Recirculation Zones," *Industrial & Engineering Chemistry*, vol. 45, no. 8, pp. 1629–1633, 1953

[17]   C. Cross, A. Fricker, D. Shcherbik, E. Lubarsky, B. T. Zinn, and J. A. Lovett, *Dynamics of Non-Premixed Bluff Body-Stabilized Flames in Heated Air Flow*, GT2010-23059, Proceedings of the ASME Turbo Expo 2010: Power for Land, Sea and Air, June 14-18, 2010, Glaskgow, UK

[18]   C. Cross et al., *Determination of Equivalence Ratio and Oscillatory Heat Release Distributions in Non-Premixed Bluff Body-Stabilized Flames Using Chemiluminescence Imaging*, GT2011-45579, Proceedings of the ASME Turbo Expo, June 6-10, 2011, Vancouver, BC, Canada

[19]   B. Emerson, J. Lundrigan, J. O'Connor, D. Noble, and T. Lieuwen, *Convective and Absolute Instabilities in Reacting Bluff Body Wakes*, GT2011-45330, Proceedings of the ASME Turbo Expo, June 6-10, 2011, Vancouver, BC, Canada

[20]   R. Erickson, M. Soteriou, and P. Mehta, *The Influence of Temperature Ratio on the Dynamics of Bluff Body Stabilized Flames*, AIAA 2006-753, 44th AIAA Aerospace Sciences Meeting and Exhibit, Jan 9-12, 2006, Reno, Nevada, USA

[21]   B. Emerson, J. O'Connor, M. Juniper, and T. Lieuwen, "Density ratio effects on reacting bluff-body flow field characteristics," *Journal of Fluid Mechanics*, vol. 706, pp. 219–250, Sep. 2012,

[22]   S. G. Tuttle et al., "Lean blowoff behavior of asymmetrically-fueled bluff body-stabilized flames," Combustion and Flame, vol. 160, no. 9, pp. 1677–1692, 2013

[23]   J. S. Lewis, *The Effect of Local Fuel Concentration on Reheat Jet Pipe Vibrations*, Proceedings of an International Propulsion Symposium Held at the College of Aeronautics, Cranfield, April 1967, Cranfield, UK

[24]   P. J. Langhorne, "Reheat buzz: an acoustically coupled combustion instability. Part 1. Experiment," *Journal of Fluid Mechanics*, vol. 193, pp. 417–443, 1988,

[25]   J. F. Driscoll and C. C. Rasmussen, "Correlation and analysis of blowout limits of flames in high-speed airflows," *Journal of Propulsion and Power*, vol. 21, no. 6, pp. 1035-1044, 2005,

[26]   M. Zhu, A. P. Dowling, and K. N. C. Bray, "Forced Oscillations in Combustors With Spray Atomizers," *Journal of Engineering for Gas Turbines and Power*, vol. 124, no. 1, pp. 20-30, Jan. 2002,

[27]   M. Zhu, A. P. Dowling, and K. N. C. Bray, "Self-Excited Oscillations in Combustors With Spray Atomizers," *Journal of Engineering for Gas Turbines and Power*, vol. 123, no. 4, pp. 779-786, Oct. 2001

[28]   H. Ebrahimi, *Overview of Gas Turbine Augmentor Design, Operation, and Combustion Oscillation*, AIAA2006-4916, 42nd AIAA/ASME/SAE/ASEE Joint Propulsion Conference & Exhibit, July 9-12, 2006, Sacramento, California, USA

[29]   M. Broumand and M. Birouk, "Liquid jet in a subsonic gaseous crossflow: Recent progress and remaining challenges," *Progress in Energy and Combustion Science*, vol. 57, pp. 1–29, Nov. 2016

[30]   P.-K. Wu, K. A. Kirkendall, R. P. Fuller, and A. S. Nejad, "Breakup Processes of Liquid Jets in Subsonic Crossflows," *Journal of Propulsion and Power*, vol. 13, no. 1, pp. 64–73, Jan. 1997,

[31]   J. Mazallon, Z. Dai, and G. M. Faeth, "Primary Breakup of Nonturbulent Round Liquid Jets in Gas Crossflows," *Atomization and Sprays*, vol. 9, no. 3, pp. 291–312, 1999

[32]   S. Tambe, S.-M. Jeng, H. Mongia, and G. Hsiao, *Liquid Jets in Subsonic Crossflow*, 43rd AIAA Aerospace Sciences Meeting and Exhibit, AIAA 2005-731, Jan 10-13, 2005, Reno, Nevada, USA.

[33]   K. A. Sallam, C. Aalburg, and G. M. Faeth, "Breakup of Round Nonturbulent Liquid Jets in Gaseous Crossflow," *AIAA Journal*, vol. 42, no. 12, pp. 2529–2540, Dec. 2004,

[34]   A. A. Ranger and J. A. Nicholls, "Aerodynamics Shattering of Liquid Drops," *AIAA Journal*, vol. 7, no. 2, pp. 285–290, 1969.

[35]   M. Behzad, N. Ashgriz, and B. W. Karney, "Surface breakup of a non-turbulent liquid jet injected into a high pressure gaseous crossflow," *International Journal of Multiphase Flow,* vol. 80, pp. 100–117, 2016,

[36]   C. A. Chryssakis, D. N. Assanis, and A. Arbor, *A Secondary Atomization Model for Liquid Droplet Deformation and Breakup under High Weber Number Conditions*, ILASS Americas 18th Annual Conference on Liquid Atomization and Spray Systems, May 2005, Irvine, California, USA

[37]   P.-K. Wu, K. A. Kirkendall, R. P. Fuller, and A. S. Nejad, "Spray Structures of Liquid Jets Atomized in Subsonic Crossflows," *Journal of Propulsion and Power*, vol. 14, no. 2, pp. 173–182, Mar. 1998,

[38]   K. Sallam, C. Ng, R. Sankarakrishnan, C. Aalburg, and K. Lee, *Breakup of Turbulent and Non-Turbulent Liquid jets in Gaseous Crossflows*, 44th AIAA Aerospace Sciences Meeting and Exhibit, AIAA 2006-1517, Jan 9-12, 2006, Reno, Nevada, USA

[39]   R. K. Madabhushi, M. Y. Leong, M. Arienti, C. T. Brown, and V. G. Mcdonell, *On the breakup regime map of liquid jet in crossflow*, ILASS Americas 19th Annual Conference on Liquid Atomization and Spray Systems, May 2006, Toronto, Ontario, CA

[40]   Z. Liu and R. D. Reitz, "An analysis of the distortion and breakup mechanisms of high speed liquid drops," *International Journal of Multiphase Flow*, vol. 23, no. 4, pp. 631–650, 1997,

[41]   L. P. Hsiang and G. M. Faeth, "Near-limit drop deformation and secondary breakup," *International Journal of Multiphase Flow*, vol. 18, no. 5, pp. 635–652, 1992,

[42]   T. Inamura and N. Nagai, "Spray Characteristics of Liquid Jet Traversing Subsonic Airstreams," *Journal of Propulsion and Power*, vol. 13, no. 2, pp. 250–256, Mar. 1997

[43]   E. Lubarsky, J. R. Reichel, B. T. Zinn, and R. McAmis, "Spray in crossflow: Dependence on Weber number," *ASME Journal of Engineering for Gas Turbines and Power*, vo. 132, no. 2, Feb 2010,

[44]   E. Lubarsky, J. T. Cutright, B. T. Zinn, and R. McAmis, *Spray Characterization at Jet Engine Thrust Augmentor Flow Conditions*, 46th AIAA Aerospace Sciences Meeting and Exhibit, AIAA 2088-1041, Jan 7-10, 2008, Reno, Nevada, USA

[45]   M. Broumand, M. Birouk, and S. V. Mahmoodi, "Liquid jet primary breakup in a turbulent cross-airflow at low Weber number," *Journal of Fluid Mechanics*, vol. 879, pp. 775–792, Nov. 2019,

[46]   J. N. Johnson, E. Lubarsky, and B. T. Zinn, *Experimental Investigation of Spray Dynamics Under Jet Engine Augmentor-Like Conditions*, Proceedings of the ASME Turbo Expo 2006: Power for Land, Sea, and Air, GT2006-91112, May 8-11, 2006, Barcelona, Spain

[47]   E. Lubarsky, D. Shcherbik, O. Bibik, Y. Gopala, and B. T. Zinn, "Fuel Jet in Cross Flow - Experimental Study of Spray Characteristics," in *Advanced Fluid Dynamics*, H. W. Oh, Ed. London, UK: InTech, 2012,

[48]   J. H. Bell and R. D. Mehta, "Contraction Design for Small Low-Speed Wind Tunnels," NASA Ames Research Center, California, USA, Contractor Report NASA-CR-177488, Aug 1988

[49]   C. K. Choi and D. K. Kwon, "Wind tunnel blockage effects on aerodynamic behavior of bluff body," *Wind and Structures, An International Journal*, vol. 1, no. 4, pp. 351–364, Sept 1998,

[50]   M. A. Macquisten and A. P. Dowling, "Combustion oscillations in a twin-stream afterburner," *Journal of Sound and Vibration*, vol. 188, no. 4, pp. 545–560, Dec. 1994,

[51]   P. W. Runstadler, F. X. Dolan, and R. C. Dean, "Diffuser data book," Creare Inc., Hanover, NH, USA, Tech. Note 186, 1975.

[52]   F. M. White, *Fluid Mechanics 7th Ed*. New York: McGraw-Hill, 2011.

[53]   K. Teschke, Y. Chow, M. Brauer, C. van Netten, S. Varughese, and S. Kennedy, *Atmospheric effects in the entertainment industry: constituents, exposures and health effects*, UBC School of Occupational and Environmental Hygiene, Web Report, pp. 99 Vancouver, CA, May 2003.

[54]   J. Song and J. G. Lee, *Characterization of Spray Formed by Liquid Jet Injected Into Oscillating Air Crossflow*, Proceedings of the ASME Turbo Expo 2015: Turbine Technical Conference and Exposition Volume 4B: Combustion, Fuels, and Emissions, GT2015-43726June 15-19, 2015, Montreal, Quebec, CA

[55]   J. Song, C. Ramasubramanian, and J. G. Lee, *Response of Liquid Jet to Modulated Crossflow*, Proceedings of the ASME Turbo Expo 2013: Turbine Technical Conference and Exposition Volume 1B: Combustion, Fuels, and Emissions, GT2013-95726, June 3-7, 2013, San Antonia, Texas, USA

[56]   J. Johnson, E. Lubarsky, and B. Zinn, *Experimental Investigation of Spray Dynamics Under Jet Engine Augmentor Conditions*, 41st AIAA/ASME/SAE/ASEE Joint Propulsion Conference & Exhibit, AIAA-2005-4480, July 10-13, 2005, Tucson, Arizona, USA

[57]   C. Tropea, A. L. Yarin, and J. F. Foss, *Springer Handbook of Experimental Fluid Mechanics*. Berlin, Heidelberg: Springer Berlin Heidelberg, 2007

[58]   E. A. Cowen and S. G. Monismith, "A hybrid digital particle tracking velocimetry technique," *Experiments in Fluids*, vol. 22, no. 3, pp. 199–211, 1997

[59]   J. Song, C. Cary Cain, and J. Guen Lee, "Liquid Jets in Subsonic Air Crossflow at Elevated Pressure," *Journal of Engineering for Gas Turbines and Power*, vol. 137, no. 4, April 2015

[60]   A. Sharma, "Liquid Jet in Oscillating Crossflow: Characterization of Near-Field and Far-Field Spray Behavior," MSc dissertation, Dept. of Aerospace Engineering, Cincinnati, Ohio, USA, 2015.

[61]   M. Behzad, A. Mashayek, and N. Ashgriz, *A KIVA-based Model for Liquid Jet in Cross Flow*, ILASS Americas 22nd Annual Conference on Liquid Atomization and Spray Systems, May 2010, Cincinnati, Ohio, USA

[62]   M. Arienti, R. K. Madabhushi, P. R. van Slooten, and M. C. Soteriou, *Aerodynamic Blockage Effect on the Spray Characteristics of a Liquid Jet Atomized by Crossflowing Air*, Proceedings of the ASME Turbo Expo 2006: Power for Land, Sea, and Ai. Volume 1: Combustion and Fuels, Education, GT2006-90536, May 8-11, 2006, Barcelona, Spain

[63]   E. Farvardin, M. Johnson, H. Alaee, A. Martinez, and A. Dolatabadi, "Comparative Study of Biodiesel and Diesel Jets in Gaseous Crossflow," *Journal of Propulsion and Power*, vol. 29, no. 6, pp. 1292–1302, Nov. 2013,

[64]   M. D. Pinchak, V. G. Shaw, and E. J. Gutmark, "The effects of cross-flow fuel injection on the reacting jet in vitiated cross-flow," *Combustion and Flame*, vol. 199, pp. 352–364, Jan. 2019

[65]   L. Doddipatla, "Wake Dynamics and Passive Flow Control of a Blunt Trailing Edge Profiled Body," PhD dissertation, Dept. of Civil and Env. Engineering, The University of Western Ontario, London, ON, CA, 2010.

6 Appendix

6.1 Appendix A: Uncertainty Analysis

The uncertainty analysis of the liquid injection flow rate Q and the freestream velocity $\bar{u}_\infty$ was performed and was used to estimate the accuracy of the momentum flux ratio q. This includes equipment uncertainty in the pressure transducer used to estimate liquid injection flow rate as well as the uncertainty associated with velocity calculations made using the PIV methodology described in Chapter 2.

6.1.1 Liquid Flow Rate Uncertainty

The accuracy of the pressure transducer used for flow rate calibration first needs to be determined. Manufacturer accuracy was stated as ±10.3kPa at 34.5kPa of system pressure and as ±6.9kPa above 34.5kPa, and this covers the linearity, hysteresis, and repeatability errors. To account for zero offset and span errors, a calibration was performed using a pressure gage which has a stated manufacturer accuracy of ±4.1kPa resolution error of ±1.7kPa. The combined contribution of these systematic errors was calculated using Equation (17), where B indicates the systematic error. The total systematic error for the pressure gage was determined as ±11.2kPa.

$$B_{gage} = \sqrt{B_{manufacturer}{}^2 + B_{resolution}{}^2} = 4.4 kPa \tag{17}$$

$$B_p = \sqrt{B_{manufacturer}{}^2 + B_{gage}{}^2} = 11.2 kPa \tag{18}$$

Throughout the experiments injection feed pressure was monitored. Multiple recordings were taken at each momentum flux rate q, and therefore at each flow rate Q. The random error P (Equation (19) associated with the sampling of pressure across multiple tests was determined using equation, where t_s is the t-statistic used in a student t-test, n is the number of samples, and S_p is the standard deviation of the sample (Equation (20).

$$P_p = t_s \frac{S_p}{n} \tag{19}$$

$$S_p = \sqrt{\frac{\sum_i^n (p_i - \bar{p})^2}{n-1}}$$

(20)

The resulting random error for each momentum flux ratio q investigated in the PIV section of this study is shown in table and are clearly of negligible value compared to the systematic uncertainty.

MOMENTUM FLUX, Q	MEAN PRESSURE, P [KPA]	RANDOM UNCERTAINTY [KPA]	PERCENTAGE OF READING [%]
10	33.4	0.0134	0.04%
20	56.6	0.0141	0.02%
60	140	0.0637	0.05%
120	256	0.0502	0.02%

The uncertainty in flow rate calculation using the stopwatch & bucket method was determined via the resolution error of the scale used to weigh the liquid and of the frame rate of the camera which were ±0.05g and $\pm\frac{1}{60}s$ respectively, while liquid density was assumed to have negligible uncertainty. Propagation of these uncertainties to the calculation of volume flow rate (equation (21) was determined using equation (22).

$$Q = \frac{m_f - m_o}{\rho t}$$

(21)

$$B_{Q,measurement} = Q * \sqrt{\left(\frac{B_m}{m}\right)^2 + \left(\frac{B_t}{t}\right)^2} < 0.1\% \ of \ Q$$

(22)

In equation (21), m_f is the final mass recorded, m_i is the initial mass recorded, ρ is the liquid density, and t is the length of the recording in seconds. In equation (22), B_m and B_t represent the uncertainty of the scale and video recording respectively. The accuracy was determined less than ±0.1% of the flow rate reading which is negligible.

Finally, the uncertainty associated with the calibration (equation (23) was performed by estimating the sensitivity of Q to p using equation calibration. The sensitivity error is given by equation (24) and was high for low flow rates at $q = 10$ and $q = 20$ (20.7% and 8.7% of Q respectively) but was 3.5% and 2% for $q = 60$ and $q = 120$.

$$Q(p) = 0.0448p^{0.6067} \tag{23}$$

$$B_{Q,sensitivity} = B_p \frac{dQ}{dp} \tag{24}$$

The total flow rate uncertainty would be estimated by determining the root of the sum of squares of all components of flow rate uncertainty (in this case the measurement uncertainty $B_{Q,measurment}$ and the sensitivity error $B_{Q,sensitivity}$). However, with such low measurement uncertainty relative to the sensitivity, it can be assumed that the total flow rate uncertainty B_Q is equal to $B_{Q,sensitivity}$.

6.1.2   Crossflow Gas and PIV Uncertainty

Factors to consider which contribute to uncertainty in PIV measurements include particle size, image dynamic range, AGW interpolation, and out-of-plane motion of particles. Uncertainty was estimated based on the work of Cowen and Monismith [58].

Given that particles were much smaller than the size of a pixel, it was assumed a diameter of 1 pixel per particle and using Figure 5a in [58] the error due to particle size is found to be 0.095 pixels. According to Figure 5b, the error for a dynamic range of 255 is 0.05 pixels with an additional error of 0.08 pixels when using AGW. To determine if out-of-plane motion was a considerable source of error, the maximum spanwise velocity of the q of 120 jet-in-counterflow test was used. This test was used as the spanwise motion was most comparable to any estimated out-of-plane motion, which is likely small. At 1.5m/s, the expected displacement is 60µm, which is negligible for a laser sheet of 1mm thickness. The error associated with seeding density, and velocity gradients was not determined but will be briefly discussed.

In the presence of velocity gradients, PIV methods are more likely to capture the slower moving particles in an interrogation window, as faster moving particles will result in larger displacements and will typically be more disperse, therefore resulting in a poorer correlation peak than say the slower particles who may remain as an ensemble. Seeding density must be of consideration as too little seeding may lead to poor displacement correlations, particularly near gradients, while dense seeding may result in high frequency noise. The total PIV error was determined as the RMS (similar to Equation (17) and was found to be 0.13 pixels which is equivalent to 0.18m/s.

There is also uncertainty associated with the calibration equation used to control the wind tunnel velocity, however since this calibration is not used to determine the freestream velocity it is simply presented here for completeness. The calibration uncertainty was determined to be less than 1% of the reading at the operating speed of the wind tunnel.

6.1.3   Momentum Flux Ratio Uncertainty

Finally, the uncertainty in determining the momentum flux ratio can be calculated based on the uncertainties in gas velocity and liquid injection velocity measurements. The density of water and air were assumed to have negligible uncertainty, so the uncertainty of the momentum flux ratio, q was determined via equation (25).

$$B_q = q * \sqrt{\left(\frac{B_{gas}}{\overline{u_\infty}}\right)^2 + \left(\frac{B_{liquid}}{v_{inf}}\right)^2} \qquad (25)$$

As might be expected, the liquid injection rate uncertainty was much larger than the PIV uncertainty. Therefore, B_q is equivalent to B_Q, and the uncertainty in the momentum flux ratio q was 20.7%, 8.7%, 3.5%, and 2% for $q = 10$, $q = 20$, $q = 60$, and $q = 120$ respectively.

Curriculum Vitae

EDUCATION

The University of Western Ontario, London/ON

MESc, Mechanical Engineering, Thermofluids   **Apr 2022**
MESc, Biomedical Engineering, Biomechanics   **Apr 2018**
BESc, Mechanical and Materials Engineering   **Apr 2015**

RESEARCH PROJECTS

Graduate Theses
Topic: *Fuel Spray Droplet Behaviour in Gas Turbine Afterburners*   **(Mechanical Engineering)**

Topic: *Shoulder Implant Fixation in Degenerative Bone*   **(Biomedical Engineering)**

WORK EXPERIENCE

Mobile Maintenance EIT   **Apr 2021**
Glencore - Kidd Operations, Timmins/ON   **Current**

Graduate Teaching Assistant   **Sept 2015**
The University of Western Ontario   **May 2020**
- Product Design
- Mechanical Component Design
- Material Selection
- Experimental Methods
- Thermodynamics I
- Fluid Mechanics II

Coop student – Maintenance Engineering   **May 2013**
Xstrata Copper- Kidd Operations, Timmins/ON   **Sept 2013**

PUBLICATIONS/CONFERENCES

Abstract #100, Co-author. "Effects of Augmented and Lateralized Glenoid Baseplate Geometry on Micromotion in the Presence of E2 Erosion", 2022 COA Annual Meeting, June 8-11, Quebec, CA

Technical Presentation, "Influence of Local Cross-Airflow Behaviour on Liquid Jet Droplet Dynamics", *FEDSM 2021* - Multiphase Flow Track, submission FEDSM2021-75774, Online

First Author, "Density distribution of the type E2 glenoid in cuff tear arthropathy", *Journal of Shoulder and Elbow Surgery,* Vol. 29, Issue 1, Jan 2020

Podium presenter, "Density Distribution Analysis of the E2-Type Glenoid", *ICORS 2019 Annual Meeting*, June 19-22, 2019, Montreal, Quebec, CA

Co-author, "Does Humeral Component Lateralization in Reverse Shoulder Arthroplasty Affect Rotator Cuff Torque? Evaluation in a Cadaver Model", *Clinical Orthopaedics and Related Research*, Vol. 475, Issue 10, Oct 2017